POLYPUBLIE

# Passage-averaged approximation of turbomachinery flows using vorticity-potential method

Xudong Zhang

Document en libre accès dans PolyPublie
Open Access document in PolyPublie

| | |
|---|---|
| **Date** | 1991 |
| **Type** | Mémoire ou thèse / Dissertation or Thesis<br>Thèse de doctorat/Ph.D. thesis |
| **URL de PolyPublie**<br>PolyPublie URL | https://publications.polymtl.ca/57968/ |
| **Conditions d'utilisation**<br>Terms of use | © Tous droits réservés / All rights reserved |
| **Référence**<br>Citation | Zhang, X. (1991). Passage-averaged approximation of turbomachinery flows using vorticity-potential method [Thèse de doctorat, Polytechnique Montréal]. PolyPublie. https://publications.polymtl.ca/57968/ |

**Détails de la thèse**
Thesis details

| | |
|---|---|
| **Directeurs de recherche**<br>Advisors | |
| **Programme**<br>Program | Non spécifié |

Ce fichier a été téléchargé à partir de PolyPublie, le dépôt institutionnel de Polytechnique Montréal
This file has been downloaded from PolyPublie, the institutional repository of Polytechnique Montréal
https://publications.polymtl.ca

UNIVERSITE DE MONTREAL

# PASSAGE-AVERAGED APPROXIMATION OF TURBOMACHINERY FLOWS USING VORTICITY-POTENTIAL METHOD

par

Xudong ZHANG

DEPARTEMENT DE MATHEMATIQUES APPLIQUEES

ECOLE POLYTECHNIQUE

THESE PRESENTEE EN VUE DE L'OBTENTION

DU GRADE DE PHILOSOPHIAE DOCTOR (Ph.D.)

JUILLET 1991

© Xudong ZHANG 1991

National Library
of Canada

Canadian Theses Service

Ottawa, Canada
K1A 0N4

Bibliothèque nationale
du Canada

Service des thèses canadiennes

The author has granted an irrevocable non-exclusive licence allowing the National Library of Canada to reproduce, loan, distribute or sell copies of his/her thesis by any means and in any form or format, making this thesis available to interested persons.

The author retains ownership of the copyright in his/her thesis. Neither the thesis nor substantial extracts from it may be printed or otherwise reproduced without his/her permission.

L'auteur a accordé une licence irrévocable et non exclusive permettant à la Bibliothèque nationale du Canada de reproduire, prêter, distribuer ou vendre des copies de sa thèse de quelque manière et sous quelque forme que ce soit pour mettre des exemplaires de cette thèse à la disposition des personnes intéressées.

L'auteur conserve la propriété du droit d'auteur qui protège sa thèse. Ni la thèse ni des extraits substantiels de celle-ci ne doivent être imprimés ou autrement reproduits sans son autorisation.

ISBN 0-315-72716-0

Canada

**UNIVERSITÉ DE MONTRÉAL**

**ÉCOLE POLYTECHNIQUE**

**Cette thèse intitulée:**

# PASSAGE-AVERAGED APPROXIMATION OF TURBOMACHINERY FLOWS USING VORTICITY-POTENTIAL METHOD

**Présentée par: Xudong ZHANG**

**en vue de l'obtention du grade de Philosophiae Doctor (Ph.D.)**

**a été dûment acceptée par le jury d'examen constitué de:**

| | |
|---|---|
| **M. René Kahawita, Ph.D.** | **Président** |
| **M. Ricardo Camarero, Ph.D.** | **Directeur** |
| **M. André Garon, Ph.D.** | **Co-directeur** |
| **M. Dominique Pelletier, Ph.D.** | |
| **M. Marcel Lacroix, Ph.D.** | |

# SOMMAIRE

La simulation numérique de l'écoulement de fluide dans une turbomachine est extrêmement difficile à cause de la complexité des phénomènes ainsi que de la géométrie. Aborder ce problème dans sa totalité, comprenant le couplage des diverses interactions, est impossible dans le contexte des outils d'analyse et de calcul dont nous disposons aujourd'hui. Ce travail concerne donc un volet de cet ensemble, soit plus spécifiquement l'interaction du rotor avec le stator. Un examen de cette configuration révèle un écoulement tridimensionnel dont la complexité de la structure découle de l'interaction entre l'écoulement à la sortie du stator et les parois en mouvement du rotor. Cette interaction est essentiellement tridimensionnelle et de nature transitoire, caractérisée par des phénomènes visqueux, turbulents, sur lesquels se superposent, à une autre échelle, des écoulements secondaires.

A ce jour, ce problème même ainsi délimité a fait l'objet de très peu d'études et généralement celles-ci sont tellement réductrices que l'on obtient peu d'informations détaillées. Il est clair qu'une approche basée sur la résolution des équations complètes est inabordable avec le niveau des moyens informatiques courants. Pour réaliser en pratique des simulations numériques avec les ressources de calcul disponibles, une stratégie utilisant un modèle simplifié

de l'interaction est nécessaire. On retrouve dans la littérature une hiérarchie de modèles classifiés en quatre familles selon la nature de l'écoulement: potentiel, rotationnel non-visqueux, visqueux et turbulent. Pour chacune de ces familles, un autre niveau de classification est possible selon la géométrie ou la dimension du problème: écoulements bidimensionnels, quasi-tridimensionnels et tridimensionnels.

Les techniques de calcul basées sur des approches utilisant diverses combinaisons de ces niveaux d'approximation ont donné lieu à des outils d'analyse et de design pour les turbomachines. Mais, jusqu'à ce jour, aucune ne prenait en compte la nature de l'interaction stator-rotor qui est essentiellement d'origine instationnaire. Cette dernière caractéristique est la cause des plus grandes difficultés. Plusieurs méthodes ont été analysées dans l'optique de pallier à ce problème, et, la méthode de la moyenne du passage s'est avérée une des plus intéressantes. Dans cette méthode, les effets produits par le mouvement des pales est pris en compte par une distribution de forces volumiques externes. L'expression pour ces forces peut être obtenue par diverses méthodes issues de considérations de la cinétique ou de la dynamique de l'écoulement. Des études antérieures ont montré que la prise en compte uniquement de la cinétique ne suffisait pas. Dans ce travail on propose une méthode, pour le calcul de ces forces, basée sur une intégration des équations du mouvement dans la di-

rection circonférentielle, et ils incorporent alors plus fidèlement la physique de ces dernières. Sur le plan du modèle ces termes se reduisent à des termes sources dans les équations du mouvement dans un plan méridional. On obtient alors deux types équations: les équations tridimensionnelles et les équations méridionales. Cette approche, pour la clôture du système d'équations, est plus rigoureuse que les autres approches utilisées jusqu'à présent.

Cette méthode a été utilisée dans plusieurs applications avec des écoulements non-visqueux. Cette étude comprend une extension de cette méthode pour les écoulements visqueux, et son intégration dans une méthodologie de calcul qui couple les solutions tridimensionelles dans le stator et dans le rotor par le biais de la solution dans le plan méridional modifiée par les termes sources.

Ces équations pour ces trois solutions ont été formulées en variables vorticité-potentiel vecteur, et vorticité-fonction de courant, respectivement. Ces formulations présentent certains avantages sur le plan calcul et mémoire, par rapport aux formulations en variables primitives.

La formulation vorticité-potentiel vecteur est l'extension en trois dimensions de la formulation vorticité-fonction de courant traditionnelle en deux dimensions. Elle suppose une décomposition en deux parties du vecteur vitesse;

une partie potentielle et une partie rotationnelle. Ensuite, la pression est éliminée du système en prenant le rotationnel du mouvement. La difficulté majeure dans cette approche réside dans le choix et l'imposition de conditions frontières du potentiel vecteur pour obtenir un problème bien posé et une solution unique. On discute dans ce travail des conditions de compatibilité de ces relations et on propose un ensemble admissible pour les équations tridimensionnelles et pour les relations méridionales.

Pour la solution de ces équations, une procédure de calcul est proposée et mise en oeuvre. Ceci comprend la résolution de deux écoulements tridimensionnels, respectivement dans les canaux inter-aube du stator et du rotor. Le domaine de calcul est borné par les pales, le moyeu, le carter et des surfaces qui définissent l'entrée et la sortie. On note qu'en posant respectivement ces dernières le long du bord d'attaque et de fuite , on contourne le problème des conditions frontières périodiques. Ces solutions sont ensuite utilisées, par une procédure d'intégration, pour évaluer les forces volumiques qui s'ajoutent aux termes des équations du mouvement du plan méridional. La solution de ces équations ainsi modifiées permet de poser les conditions de sortie et d'entrée aux écoulements dans le stator et dans le rotor respectivement, et, ainsi réaliser le couplage nécessaire au calcul de l'interaction. Afin de faciliter le transfert d'information entre les solutions tridimensionnelles et l'équation méridionale,

les maillages pour ces deux domaines coïncident.

Le processus global, consiste à calculer les solutions tridimensionnelles avec des conditions axisymétriques obtenues de la solution méridionale à ces stations. Après le calcul des termes volumiques, l'équation méridionale modifiée est calculée. Outre les composantes axiale et radiale, cette équation donne également la composante circonférentielle. Cette dernière traduit l'effet de rotation induit par les pales. Le procesus itératif est répété jusqu'à convergence, définie lorsque deux itérées successives ne changent pas.

Pour la résolutions numérique de ces équations, on a mis en oeuvre une méthode implicite pour une prise en compte des conditions frontières. Il s'agit d'une méthode directe utilisant une décomposition LU de la matrice globale. Quoique plus exigeante sur le plan mémoire, cette méthode, contrairement aux méthodes itératives de type du point fixe assure la stabilité de la solution.

Une procédure globale qui intégre les divers éléments a été developpée et validée sur quelques configurations simples. Ensuite une application pratique, la pompe du NEL a été calculée. Il s'agit du modèle expérimental le mieux adapté au dévelopement numérique proposé. Celle-ci comprend un rotor à cinq pales et un stator à neuf pales. Les mesures expérimentales utilisées pour compléter la comparaison avec les calculs numériques sont les vitesses

mesurées, à plusieurs sections du rotor en mouvement à 1200 tours par minute et pour un nombre de Reynolds de $1.5x10^6$.

Le domaine de calcul sur la plan méridional est divisé en cinq parties; la conduite en amont du rotor, le canal inter-aube du rotor, la conduite entre le rotor et le stator, le canal inter-aube du stator, et finalement la conduite d'évacuation. Le maillage est de 13x59 sur le plan méridional et de 13x15x15 et 13x13x21 pour le rotor et le stator respectivement.

Les comparaisons entre les mesures expérimentales et les résultats numériques sont faites à plusieurs sections de la machine. Pour une section donnée on a comparé, sur plusieurs coupes inter-aubes (circonférentielles), les profils de vitesse normalisé dans la direction axiale. Dans les résultats numériques on retrouve les caractéristiques générales de l'écoulement, c'est-à-dire une accélération sur l'extrados et une décélération sur l'intrados. Quantitativement les comparaisons sont bonnes dans le coeur de l'écoulement, avec des différence dans les couches limites. On donne deux raisons; d'abord la différences dans le nombre de Reynolds entre l'écoulement laminaire du calcul et l'écoulement en laboratoire qui est nécessairement turbulent. Ensuite dans le modèle numérique, on suppose aucune fuite entre les pales et le carter de la pompe. Dans la réalité, la fuite cause une modification importante de la structure de l'écoulement secondaire, ainsi que des couches limites plus importantes que celles

prédites.

Les résultats de ce travail peuvent être améliorés selon plusieurs aspects. Le premier est du point de vue de la technologie de calcul utilisé, pour résoudre les systèmes matriciels, et consiste à remplacer le stockage en ligne de ciel par un stockage compressé en rangée pour minimiser la mémoire requise. Ce changement implique l'utilisation d'une technique de calcul adapté à cette méthode de stockage. Nous proposons de tester des variantes du gradient conjugué comme CGS, CGSTAB, LSQR, et GMRES. Le second point consiste à augmenter les domaines tridimensionnels du rotor et du stator pour couvrir l'ensemble du domaine de calcul. Ceci permettra d'éliminer le calcul de la solution méridionale et ainsi améliorer le couplage entre les solutions du stator et du rotor.

# ABSTRACT

In this thesis, a physical and mathematical model based on a passage-averaged vorticity-potential formulation for the simulation of flows in a rotor-stator stage of a turbomachine is presented. The passage-averaged governing equations have been developed by taking into account the viscous effects through the three-dimensional Navier-Stokes equations applied to flows within blade rows.

An implicit three-dimensional algorithm has also been developed for solving, within the blade passages, the three-dimensional Navier-Stokes equations in terms of vorticity, scalar and vector potentials. This algorithm is coupled with the passage-averaged governing equations to form a closed set of equations describing rotor-stator flow interactions.

Validation of the numerical algorithms is primarily performed on a number of test problems, including the developing flows in a channel, rotating annulus, straight and curved ducts. A more realistic test computation for an impeller with planar blades completes the validation. The numerical results are compared with available analytical solutions and experimental data.

Finally, the model has been used to predict flow within a mixed-flow pump. The results were compared with the measurements provided by the National Engineering Laboratory.

# ACKNOWLEDGEMENT

I would like to express my great gratitude to Professor Ricardo Camarero and Dr. André Garon from the Department of Applied Mathematics, for their guidances, suggestions, encouragement, understanding and continuous support from the inception to the present form of this thesis.

I would also like to acknowledge the help I have received from my friends at École Polytechnique, especially from the members of the group MIAO of the Department of Applied Mathematics.

In addition, I acknowledge the support of the Ministère de l'Éducation du Québec for the exemption of the foreign student tuition fees and the financial support of CRIM.

Last, but not least, I wish to thank my wife Zhao Qing, for her encouragement and understanding throughout my graduate studies.

# TABLE OF CONTENTS

**Sommaire** iv

**Abstract** xi

**Acknowledgement** xiii

**List of Tables** xix

**List of Figures** xx

**Nomenclature** xxiv

**1 Introduction** 1

1.1 Problem Statement . . . . . 1

1.2 Literature Survey of Numerical methods for Turbomachinery 2

1.2.1 Levels of Approximation . . . . . 3

1.2.2 Numerical Methods . . . . . 5

1.2.3 Through-Flow Approaches . . . . . 8

1.3 Literature Survey of Solution Methods . . . . . 9

1.3.1 Primitive Variable Methods . . . . . 9

1.3.2 Non-Primitive Variable Methods . . . . . 10

1.4 Contribution of the Present Work . . . . . 12

**2 Governing Equations in Three-Dimensions** **15**

2.1 Introduction . . . . . 15

2.2 Primitive Variable Equations . . . . . 16

2.3 Vorticity-Potential Equations . . . . . 19

2.4 Curvilinear Coordinate Formulation . . . . . 24

2.5 Boundary Conditions . . . . . 27

2.5.1 Scalar Potential Boundary Conditions . . . . . 28

2.5.2 Vector Potential Boundary Conditions . . . . . 30

2.5.3 Vorticity Boundary Conditions . . . . . 34

2.5.4 Velocity Boundary Conditions . . . . . 35

2.5.5 Summary of the Boundary Conditions . . . . . 35

**3 Passage-Averaged Governing Equations(PAGE)** **38**

3.1 Introduction . . . . . 38

3.2 Passage-Averaging Operator . . . . . 38

3.3 Passage-Averaged Equations . . . . . 41

**4 Modified Passage-Averaged Governing Equations(MPAGE)** **44**

4.1 Introduction . . . . . 44

4.2 Alternative Equation System . . . . . 45

4.2.1 Swirl Equation for Axisymmetric Flow . . . . . 45

4.2.2 Modified Passage-Averaged Equations . . . . . 47

4.3 Curvilinear Coordinate Formulation . . . . . 52

4.4 Boundary Conditions . . . . . 54

**5 Coupling Between the 3DGE and the MPAGE** **57**

5.1 Introduction . . . . . 57

5.2 Data Flow from the 3DGE to the MPAGE . . . . . 58

5.3 Data Flow from the MPAGE to the 3DGE . . . . . 58

**6 Solution Procedure** **60**

6.1 Introduction . . . . . 60

6.2 Line Relaxation Method . . . . . 60

6.3 Fully Implicit Method . . . . . 61

6.4 Scalar Potential Test . . . . . 63

6.5 Global Algorithm for the 3DGE . . . . . 66

6.6 Global Algorithm for the MPAGE . . . . . 67

6.7 Global Computational Procedure . . . . . 68

**7 Validations** **70**

7.1 Introduction . . . . . 70

7.2 Validation for the 3DGE . . . . . 71

7.2.1 Developing Flow in a Straight duct . . . . . 71

7.2.2 Developing Flow in a Curved duct . . . . . 73

7.3 Validation of the MPAGE . . . . . 75

7.3.1 Developing Flow in Channels . . . . . 75

7.3.2 Flow in a Rotating Annulus . . . . . 76

7.3.3 Flow in a Rectangular Duct . . . . . 77

7.3.4 Flow in an Impeller with Planar Blades . . . . . 81

**8 Applications to a Rotor-Stator Stage** **85**

8.1 Introduction . . . . . 85

8.2 Description of the NEL Pump . . . . . 85

8.3 Numerical Predictions . . . . . 87

8.3.1 Rotor Three-Dimensional Results . . . . . 87

8.3.2 Stator Three-Dimensional Results . . . . . 92

8.3.3 Comparison between the MPAGE and 3DGE Results 94

8.3.4 MPAGE Results without Stator . . . . . 95

**9 Conclusion and Recommendations** **96**

**References** **99**

**Appendix A: Relations between rotating and stationary frame of references** **112**

**Appendix B: Local orthogonal curvilinear coordinate system** **115**

**Appendix C: Passage-averaged analytical solution for straight duct** **117**

# LIST OF TABLES

6.1 Scalar potential test using Line SOR method . . . . . 65

6.2 Scalar potential test using implicit method . . . . . 66

# LIST OF FIGURES


3.1 Configuration of a Blade Row . . . . . 119

6.1 Sectional View of Domains with Skewness, $\alpha$ . . . . . 120

6.2 History of Convergence for Scalar Potential Test . . . . . 121

7.1 Duct Configuration . . . . . 122

7.2 Velocity Development for a Straight Duct with Aspect Ratio $\gamma = 1.0$ . . . . . 123

7.3 Fully-Developed Velocity Profiles, $\gamma = 1.0$ . . . . . 124

7.4 Center-Line Velocity Development, $\gamma = 1.0$ . . . . . 124

7.5 Velocity Development for a Straight Duct with Aspect Ratio $\gamma = 0.5$ . . . . . 125

7.6 Fully Developed Velocity Profiles, $\gamma = 0.5$ . . . . . 126

7.7 Center-Line Velocity Development, $\gamma = 0.5$ . . . . . 127

7.8 Square Curved Duct . . . . . 127

7.9 Streamwise Velocity Development . . . . . 128

7.10 Fully Developed Velocity, $\vartheta = 102.4^0$ . . . . . 129

7.11 Secondary Velocity Vectors . . . . . 130

7.12 Fully Developed Flow Through a Two-Dimensional Channel 133

7.13 Fully Developed Axisymmetric Flow . . . . . 134

7.14 Flow in a Rotating Annulus . . . . . 135

7.15 Passage-Averaged Axial Velocity Profiles . . . . . 136

7.16 Passage-Averaged Shear Force Profiles . . . . . 137

7.17 Center-Line Shear Force Development with Aspect Ratio $\gamma$ = 0.25 . . . . . 138

7.18 Impeller Geometry . . . . . 138

7.19 Development of Velocity Components with and without External Forces . . . . . 139

7.20 Velocity Comparisons for Different Angular Velocities, Re = 100 . . . . . 140

7.21 Velocity Comparisons for Different Reynolds Numbers, $\omega = 0.5$ 141

7.22 Secondary Velocity Vectors, Re = 100, $\omega = 1.0$ . . . . . 142

7.23 Ribbon Patterns within the Impeller, Re = 100, $\omega = 1.0$ . . 145

8.1 Cross-Section Through the Mixed-Flow Pump (From Carey et al. 1985a) . . . . . 146

8.2 Domain for the MPAGE Computation . . . . . 147

8.3 Domains for the 3DGE Computations . . . . . 147

8.4 Grid for the MPAGE Computation . . . . . 148

8.5 Grids for the 3DGE Computations . . . . . 148

8.6 Definition of Velocity Components (From Carey et al. 1985b) 149

8.7 Station Locations . . . . . 149

8.8 Surface Plots for Components $V_p$, Rotor . . . . . 150

8.9 Surface Plots for Components $W_t$, Rotor . . . . . 151

8.10 Surface Plots for Components $V_n$, Rotor . . . . . 152

8.11 Blade-to-Blade Velocity Components $V_p$, Rotor . . . . . 153

8.12 Blade-to-Blade Velocity Components $W_t$, Rotor . . . . . 154

8.13 Blade-to-Blade Velocity Components $V_n$, Rotor . . . . . 155

8.14a Blade-to-Blade Velocity Vector at R=0.167, Rotor . . . . . 156

8.14b Blade-to-Blade Velocity Vector at R=0.333, Rotor . . . . . 157

8.14c Blade-to-Blade Velocity Vector at R=0.500, Rotor . . . . . 158

8.14d Blade-to-Blade Velocity Vector at R=0.667, Rotor . . . . . 159

8.14e Blade-to-Blade Velocity Vector at R=0.833, Rotor . . . . . 160

8.14f Blade-to-Blade Velocity Vector at R=0.917, Rotor . . . . . 161

8.15 Secondary Velocity Vectors, Rotor . . . . . 162

8.16 Flow Phenomena with Tip Leakage Flow, Rotor (From Carey et al. 1985b) . . . . . 163

8.17 Surface Plots for Component $V_p$, Stator . . . . . 164

8.18 Surface Plots for Component $V_t$, Stator . . . . . 165

8.19 Surface Plots for Component $V_n$, Stator . . . . . 166

8.20 Blade-to-Blade Velocity Component $V_p$, Stator . . . . . 167

8.21 Blade-to-Blade Velocity Component $V_t$, Stator . . . . . 168

8.22 Blade-to-Blade Velocity Component $V_n$, Stator . . . . . 169

8.23 Blade-to-Blade Velocity Vectors, Stator . . . . . 170

8.24 Secondary Velocity Vectors, Stator . . . . . 172

8.25 Passage-Averaged Hub-to-Shroud Velocity Component $\bar{V}_p$ . . 173

8.26 Passage-Averaged Hub-to-Shroud Velocity Component $\bar{V}_t$ . . 174

8.27 Passage-Averaged Hub-to-Shroud Velocities with and without the Stator . . . . . 175

B.1 Local Coordinate System on the Boundary Surface . . . . . 176

# NOMENCLATURE

| | |
|---|---|
| $\boldsymbol{A}$ | vector potential |
| $A^1, A^2, A^3$ | components of **A** in cartesian coordinate system |
| $A^r, A^\theta, A^z$ | components of **A** in cylindrical coordinate system |
| $B$ | blockage ratio ($\delta/k$) |
| $D$ | width of a channel |
| $D_h$ | hydraulic diameter (4 × area/perimeter) |
| $\boldsymbol{E}$ | vector potential of **A** |
| $\boldsymbol{F}$ | external force |
| $g^{mn}$ | metric coefficients in 3D cartesian coordinate system |
| $h_{t_1}, h_{t_2}, h_n$ | metric coefficients in a local curvature in the local orthogonal coordinate system |
| $J$ | Jacobian of the coordinate transformation |
| $k$ | angular distance between the camber surfaces of two neighbour blades ($2\pi/N$) |
| $L$ | duct length |
| $N$ | number of blades |

| | |
|---|---|
| $\vec{n}$ | outward normal vector to the boundary surface of a 3D domain |
| $\vec{n}$ | outward normal vector to the boundary of a 2D domain |
| $p$ | pressure |
| $P_0$ | pressure at stagnation point |
| $q$ | scalar function |
| $r, \theta, z$ | cylindrical coordinates, $\theta$ is the distance corresponding to the polar angle |
| $Rc$ | center-line curvature of a curved duct |
| $Re$ | Reynolds number |
| $S_1$ | blade-to-blade streamsurface |
| $S_2$ | hub-to-shroud streamsurface |
| $s$ | outward coordinate direction |
| $t$ | time |
| $\vec{t}_1, \vec{t}_2$ | tangential vectors on the boundary surface of a 3D domain |
| $\vec{t}$ | tangential vector on a boundary curve in 2D |
| $U$ | relative velocity vector |
| $u^1, u^2, u^3$ | components of $\mathbf{U}$ in cartesian coordinate system |
| $u^r, u^\theta, u^z$ | components of $\mathbf{U}$ in cylindrical coordinate system |

| | |
|---|---|
| $U_t$ | the blade velocity at the midpoint of the rotor trailing edge |
| $\boldsymbol{V}$ | absolute velocity vector |
| $v^1, v^2, v^3$ | components of V in cartesian coordinate system |
| $v^r, v^\theta, v^z$ | components of v in cylindrical coordinate system |
| $V_n$ | velocity component normal to the streamwise grid line |
| $V_p$ | velocity component parallel to the streamwise grid line |
| $V_t$ | absolute circumferential velocity component |
| $\boldsymbol{W}$ | vorticity vector |
| $w^1, w^2, w^3$ | components of W in cartesian coordinate system |
| $w^r, w^\theta, w^z$ | components of W in cylindrical coordinate system |
| $W_t$ | relative circumferential velocity component |
| $x^1, x^2, x^3$ | cartesian coordinates |
| $x, y, z$ | cartesian coordinates |
| $\alpha, \beta, \gamma$ | metric coefficients in 2D |
| $\beta$ | parameter |
| $\gamma$ | aspect ratio (b/a) |
| $\delta$ | angular distance between surfaces of neighbour blades |
| $\lambda_s, \lambda_p, \lambda_c$ | suction, pressure and camber surfaces scalar functions |

| | |
|---|---|
| $\nu$ | kinematic viscosity |
| $\xi, \eta, \varsigma$ | curvilinear coordinates |
| $\xi_{t_1}, \xi_{t_2}, \xi_n$ | local orthogonal curvilinear coordinates |
| $\rho$ | density |
| $\phi$ | scalar potential |
| $\varphi, \psi$ | scalar functions |
| $\vartheta$ | angular distance in a curved duct |
| $\Omega$ | subspace of $R^3$ |
| $\partial\Omega$ | boundary $\Omega$ |
| $\Omega$ | angular velocity vector |
| $\omega$ | magnitude of the angular velocity vector $\Omega$ |

*Superscripts*

| | |
|---|---|
| $\bar{}$ | passage-averaged quantity |
| $\sim$ | perturbation quantity |
| $*$ | dimensional variable |
| $1, 2, 3$ | components of a vector in $(x^1, x^2, x^3)$ system |
| $x, y, z$ | components of a vector in $(x, y, z)$ system |

| | |
|---|---|
| $r, \theta, z$ | components of a vector in $(r, \theta, z)$ system |

*Subscripts*

| | |
|---|---|
| $p$ | value on the pressure surface |
| $s$ | value on the suction surface |
| $c$ | value on the camber surface |
| $S$ | tangential projection of a vector on a surface $S$ |
| $R$ | relative variable |
| $\Omega$ | difference between the absolute and relative variables |
| $t_1, t_2, n$ | components of a vector in local orthogonal coordinate system |

*Abbreviations*

| | |
|---|---|
| $3DGE$ | three-dimensional governing equations |
| $MPAGE$ | modified passage-averaged governing equations |
| $PAGE$ | passage-averaged governing equations |
| $PS$ | pressure side |
| $SS$ | suction side |
| $NEL$ | National Engineering Laboratory |

# Chapter 1

# Introduction

## 1.1 Problem Statement

The numerical simulation of the fluid dynamics in turbomachines is a difficult subject due to three-dimensional viscous effects, and further complicated by the rotor-stator flow interaction.

It is observed that(Sieverding 1985), within rotor blade passage, the flow has components of vorticity along the streamwise direction resulting partly from the blade curvature and the relative movement of the blade with respect to the shroud. This generates enough distortion of the boundary layer to induce significant secondary flows.

In the region of the rotor near the shroud, tip-leakage flow and the scraping of the vortex play a major role in shaping the three-dimensional structure of the flow. Tip-leakage flow results from the pressure difference which exists between the pressure and suction sides of the blade. The scraping of the vortex is caused by the relative motion of the shroud and occurs near the shroud and the pressure side of the blade. These flow phenomena give rise

to an intense mixing region.

Within a rotor-stator configuration, the flow field is unsteady, spatially aperiodic and highly rotational. This makes the coupling between the stator and rotor flows in a multiblade row an extremely difficult problem to solve and for which there has been very little analysis.

Because of the special characters and the complexity of flow behaviour in turbomachines, appropriate models need to be implemented.

## 1.2 Literature Survey of Numerical methods for Turbomachinery

From the numerical methods and computing systems points of view, the resolution of the full equations of motion for a multistage turbomachine is a formidable if not impossible task. To achieve a numerical simulation within current computational capabilities, reduction of the complexity is required to simplify the governing set of equations by appropriate modelling and approximations. In this section we review the different levels of approximation available and their implications.

### 1.2.1 Levels of Approximation

There are, generally, two levels of approximations; one is the dynamical level and the another is the spatial level of approximation. Most of the existing flow models can be characterized by a combination from these two levels.

The dynamical level of approximation is performed with regard to the physical properties of the flow (potential, rotational, viscous, turbulent ...) by investigating the order of magnitude of certain forces or terms of the governing equations to arrive at a simplified system of equations.

For flows with a predominant direction and with no separation or with a small amount of back-flow, the viscous and turbulent forces can be simplified by neglecting diffusion in the streamwise direction. This is the Thin Shear Layer approximation. If, furthermore, only the pressure field is treated as elliptic while all other variables are considered to have parabolic behaviours, the Partially Parabolic approximation is recovered.

One other extreme case of approximation can be obtained by totally neglecting the viscosity and turbulent forces. This is the well know Inviscid approximation.

There is another approximation which has been used in multistage turbomachines to predict rotor-stator interaction based on some average of the

flow properties. In this class of approximation the blade-to-blade effects are replaced by external forces which are coupled to the through-flow governing equations. To evaluate these external forces, a closure model must be developed. This approximation was initially proposed by Bosman & Marsh (1974) for applications in through-flow calculations and subsequently used by Bosman & El-Shaarawi (1977) and Jennions & Stow (1985a,1985b). Based on the same principle, a more elaborate model has been developed by Adamczyk (1984) and applied to the full three-dimensional model. This approximation has shown its advantages and its flexibility to simulate flows through multistage machines but requires computer resources not commonly available.

The spatial level approximation is based on the spatial representation of the flow. The resulting model equation system can be characterized as full three-dimensional, quasi three-dimensional, two-dimensional or even one-dimensional.

Clearly, a higher level of approximation is always the most attractive target. But it is not always possible to provide satisfactory numerical results to the most complete set of equations since they demand large computer resources (Chapman (1979)). So, progress in this field will depend largely on innovative numerical schemes based on analysis and contributions to the lower level of approximations.

### 1.2.2 Numerical Methods

Despite the numerous efforts made towards the solution of the flow fields in turbomachines, direct simulation of viscous flow is still not routinely used. Furthermore, most of the methods which have been developed are still mostly limited to inviscid flows.

However, along with the inviscid flow approximation, there are a great number of numerical methods based on the Euler equations, the stream function equations and the potential equations. A thorough review of the inviscid approximation as well as the viscous approximation can be found in McNally & Sockol (1985) and Hirsch & Deconinck (1985).

The development of the through-flow calculations can be traced back to the work of Wu (1952), in which a steady inviscid flow solution is calculated on the hub-to-shroud $S_2$ surfaces and blade-to-blade $S_1$ surfaces. Three-dimensional calculations can be performed by iteratively computing the two families of intersecting streamsurfaces (Krimerman & Adler (1978) and Wang et al. (1985)). In the quasi-three-dimensional approximation, it is assumed that the $S_1$ surfaces are surfaces of revolution and only one $S_2$ surface is used (Wang et al. (1985) and Jennions & Stow (1985a, 1985b))

In the work of Jennions & Stow (1985a, 1985b), the effects of the shear stress have been considered using the consistent loss model. The resulting

equations are still in inviscid form, but with a dissipative force term related to the entropy, blade force and viscous effects which can be provided from a blade-to-blade calculations. However the details of the losses due to the shear stresses are not considered so that this model is not able to predict correctly the flows in the region with strong shear stress gradients in the vicinity of the blade surfaces.

It is possible to incorporate the effects of the end-wall boundary layers into the quasi-three-dimensional model system by using the viscous-inviscid interaction method. Details of these approaches are given in Stow (1985) and Hirsch & Deconinck (1985).

Most of these methods have been used effectively to deal with the inviscid flow through turbomachines and can be credited with many interesting results to both analysis and design problems. A more complete three-dimensional average-passage equation system has been developed by Adamczyk (1984), especially derived for analyzing viscous flows in multiblade row. Its applications include the calculation of the inviscid flow through a counterrotating propeller (Adamczyk et al. (1986) and Celestina et al. (1986)) and the simulation of the viscous flow in a axial flow turbine (Adamczyk et al. (1990).

Based on the viscous through-flow approximation, Garon (1987) and Garon et al. (1989) have imposed an additional constraint equation to the

Navier-Stokes equations to model the blade forces. Such blade forces account for the pressure jump between pressure side and suction side. The resulting system of equations is solved by the finite element formulation with mixed and penalty method.

In two-dimensions, many of the early works used the vorticity-stream function approach for incompressible flows. Three-dimensional situation, incompressible flows may also be formulated in terms of the vorticity and a three-dimensional analogue of the stream function, referred to as the vector-potential, which is a solenoidal vector field as indicated by Aziz & Hellums (1967). But most three-dimensional flow analysis have been limited to the primitive formulation. The vorticity-potential approach has not been successfully implemented due to difficulties in the specification of boundary conditions on the vector potential as well as the increased number of unknowns and equations. However, Hirasaki & Hellums (1968, 1970) have shown that a simple evaluation of the boundary conditions is possible if one introduces a scalar potential. Further discussions on this subject and its applications to duct flows can be found in Wong et al. (1984, 1986) and Yang & Camarero (1986, 1991). The work of Yang & Camarero shows that this approach is also accurate and efficient for analyzing internal flows in turbomachines.

### 1.2.3 Through-Flow Approaches

The through-flow approach has played an important role in simulating flows in multistage turbomachines. There are in general two types of through flow approximations. One is the streamsurface technique and another is the passage-averaged technique.

In the streamsurface technique, the conservation equations are expressed directly on the volume enclosed between two streamsurfaces with a given circumferential thickness. To do this, a streamsheet thickness must be introduced. Both the streamsurface and the thickness are flow dependent and have to be determined by blade-to-blade calculations.

The passage-averaged representation is obtained by integrating the flow properties over the circumferential direction of the blade row. This means that the passage-averaged flow properties are defined on the average meridional cross-section of the turbomachine. If the flow is assumed to be periodic from one blade passage to another, the passage-averaged flow properties can be represented by integration from the pressure side to suction side of the blade. In the derived formulations, a tangential blockage parameter, which is a geometrical factor, is introduced to replace the flow dependent streamsheet thickness in the streamsurface formulations. Details about the through flow approach is reviewed in Hirsch & Deconinck (1985).

## 1.3 Literature Survey of Solution Methods

Numerical methods for solving the Navier-Stokes equations are generally classified in two groups. The first group is the primitive variable formulation in which the primitive variables, the velocities, pressure, density and temperature(or energy) are used as unknowns. The second group is the non-primitive variable formulation in which at least one of the unknowns is derived from primitive variables. These variables include the vorticity, stream function and potentials.

### 1.3.1 Primitive Variable Methods

The primitive variable methods are widely used for both compressible and incompressible fluid flows. For the compressible Navier-Stokes equations, various numerical schemes have been developed as in Briley & McDonald (1977), Beam & Warming (1978), Shang et al. (1980), Pulliam & Steger (1980), and Obayashi & Kuwahara (1986).

For incompressible viscous flows, one of the major problems related to the primitive variables is the solution method of the pressure field which should be used to guarantee a divergence free velocity field. The use of a Poisson equation for pressure was proposed by Harlow & Welch (1965).

The widely used SIMPLE algorithm has been developed by Patankar (1980). An intensive discussion about the difficulties using this approach was given in Gresho (1987). To achieve a greater computational efficiency, a method using artificial compressibility to impose mass conservation was proposed by Chorin (1967). A similar method which is called the pseudo-compressibility method was developed by Steger & Kutler (1977). Related discussion and applications of this approach can be found in Chang & Kwak (1984) and Kwak et al. (1984).

### 1.3.2 Non-Primitive Variable Methods

The vorticity-stream function formulation is frequently used for solving two-dimensional, incompressible flows. This is a well-known non-primitive variable method and a comprehensive analysis of this formulation has been given by Roache (1982). There are some other mixed variable methods, such as the vorticity-velocity and vorticity-potential method. These methods are particularly applicable for three-dimensional problems.

Fasel (1976) appears to be among the first to use the vorticity-velocity formulations with which he investigated the stability of two-dimensional boundary layer using an iterative finite difference scheme. Dennis et al. (1979) extended this method in a similar way for a three-dimensional calculation of

steady incompressible flows. Finite elements approaches using the vorticity-velocity formulation are reported by Guevremont et al. (1988, 1990). Gatsti et al. (1982), Farouk & Fusegi (1985), Speziale (1987) and Guj & stella (1988) also worked on this formulation.

The vorticity-potential method was first employed by Aziz & Hellums (1967) to the numerical solutions of two- and three-dimensional equations of motion in transient laminar natural convection. In their studies, the velocity is formulated in terms of a vector potential. This technique has been developed by Ozoe et al. (1976, 1985) and applied to various laminar and turbulent natural convection problems.

Although the vorticity-vector potential formulation has been extensively analysed by Aziz & Hellums (1967) and Hirasaki & Hellums (1968), there have been some confusions and unnecessary complications over the boundary conditions for the vector potential. Later, Hirasaki & Hellums (1970) realized that a simplification is possible if the velocity is decomposed in its irrotational and rotational parts by introducing a scalar potential as well as a vector potential. Since there are two potentials involved in the formulation, some authors call this method a dual potential method. Further discussions and applications can be found in the work of Richardson & Cornish (1977) and Wong & Reize (1986) with extensions to multiple connected domains, Aregbesola & Berley (1977) and Wong & Reize (1984) for internal straight

duct flows, Yang & Camarero (1986, 1990) for curved duct flows, Davis et al. (1989) for external flow problems and Rao et al. (1989) for inviscid flow applications of this method.

Although most of the non-primitive variable methods are developed for incompressible fluid flows, there have been some applications to compressible flow problems. These include the work of El-Refaee et al. (1981), Morino (1985), Habashi et al. (1987), Gerard(1989) and Guevremont et al. (1990). Many of these work use vorticity-velocity method, while Gerard's work uses vorticity-potential method and shows the applicability of the vorticity-potential method to two- and three-dimensional compressible flow problems.

## 1.4 Contribution of the Present Work

The objectives of the present study are, taking advantage of the passage-averaged through-flow approximation and the vorticity-potential representation of the Navier-Stokes equations, to develop a numerical algorithm for the prediction of the flow in the configuration of a rotor-stator stage turbomachines and to provide a better understanding of the flow phenomena in turbomachinery blade passages and the rotor-stator interaction.

The vorticity-potential formulation of the Navier-Stokes equations are averaged by the passage-averaging procedure. The external forces are calculated from three-dimensional solutions within blade rows instead of approximate blade-to-blade solutions or correlations.

An algorithm has been developed to solve the passage-averaged equations. Also, an implicit three-dimensional algorithm has been developed for the three-dimensional predictions within blade rows. At present, this study is restricted to steady incompressible laminar flows.

The main body of this thesis consists of eight chapters. Following the introduction, chapter 2 states the basic three-dimensional incompressible governing equations in terms of the primitive variable, velocity and pressure, as well as in terms of vorticity, scalar and vector potentials. The curvilinear coordinate form of these equations and boundary conditions are also discussed in this chapter. In chapter 3, a passage-averaging procedure is described and the passage-averaged governing equations are derived directly from the three-dimensional equations. In chapter 4, an alternative form of the passage-averaged equations is introduced. The curvilinear coordinate formulation and related conditions are also presented. In chapter 5, the coupling between the three-dimensional algorithm and the passage-averaged algorithm is explained. The numerical methods used in the present study are outlined and the procedures for the three-dimensional and the passage-averaged through-

flow computations as well as for their coupling are described in chapter 6. In chapter 7, numerical computations for validating the developed approximations are presented and compared with the available analytical solutions and measurements. The results for the NEL pump and comparison with the experimental data are presented in the chapter 8.

# Chapter 2

# Governing Equations in Three-Dimensions

## 2.1 Introduction

In this chapter, the three-dimensional Navier-Stokes equations for steady, laminar and incompressible fluid flow are presented. Before proceeding to the description of these equations in terms of vorticity and potentials, the primitive variables expression of these equations is presented. The introduction of the vorticity and the decomposition of the velocity field into a rotational and an irrotational part yields the vorticity and scalar-vector potential formulation for these equations. These are given in the second section. Finally, since body-fitted grids are used, the curvilinear coordinates formulation of these equations is also presented and related boundary conditions are discussed.

## 2.2 Primitive Variable Equations

The governing equations for the viscous laminar incompressible flow of a Newtonian fluid are the Navier-Stokes equations which can be written in vector form as follows:

**Conservation of Mass:**

$$\nabla \cdot \boldsymbol{V}^* = 0 \tag{2.1}$$

**Conservation of Momentum:**

$$\frac{\partial \boldsymbol{V}^*}{\partial t} + (\boldsymbol{V}^* \cdot \nabla)\boldsymbol{V}^* = -\frac{1}{\rho^*}\nabla p^* + \nu^* \nabla^2 \boldsymbol{V}^* + \boldsymbol{F}^* \tag{2.2}$$

where the $\boldsymbol{V}^*(\boldsymbol{x},t)$, $p^*(\boldsymbol{x},t)$ and $\boldsymbol{F}^*(\boldsymbol{x},t)$ are the velocity vector, static pressure and body force fields respectively. $\boldsymbol{x} = (x^1, x^2, x^3)$ is a point in $R^3$, the three-dimensional Euclidean space, t is time, $\rho^*$ and $\nu^*$ are the density and kinematic viscosity respectively.

In the present study, it is assumed that the flow is steady and that the body force field is conservative (i.e. $\boldsymbol{F}^*$ can be expressed as the gradient of a scalar function). Then the continuity and momentum equations (2.1),(2.2) can be simplified as:

$$\nabla \cdot \boldsymbol{V}^* = 0 \tag{2.3}$$

$$(\boldsymbol{V}^* \cdot \nabla)\boldsymbol{V}^* = -\frac{1}{\rho^*}\nabla \overline{p}^* + \nu^* \nabla^2 \boldsymbol{V}^* \tag{2.4}$$

where $\overline{p}^*$ is the reduced pressure defined by:

$$\overline{p}^* = p^* + \rho^* q^* \tag{2.5}$$

with

$$\boldsymbol{F}^* = -\nabla q^* \tag{2.6}$$

In a non-inertial rotating coordinate system, the continuity equation keeps the same form with the absolute velocity vector replaced by a relative one. However, in the momentum equations, Coriolis and centrifugal forces are added to the left hand side of equation (2.4). These forces can be expressed as

$$2\Omega^* \times \boldsymbol{U}^* \tag{2.7}$$

and

$$-\nabla(\frac{1}{2}\omega^{*2} r^{*2}) \tag{2.8}$$

where $\boldsymbol{U}^*$ is the relative velocity vector, $\Omega^*$ is the angular velocity vector and $\omega^*$ its magnitude. The centrifugal acceleration (2.8) is conservative and can be included into the pressure term by introducing another reduced pressure $\overline{\overline{p}}^*$ as:

$$\begin{aligned} \overline{\overline{p}}^* &= \overline{p}^* - \frac{1}{2}\rho^* \omega^{*2} r^{*2} \\ &= p^* + \rho^*(q^* - \frac{1}{2}\omega^{*2} r^{*2}) \end{aligned} \tag{2.9}$$

Equations (2.3–2.4) can then be rewritten in a rotating coordinate system as follows:

$$\nabla \cdot U^* = 0 \tag{2.10}$$

$$(U^* \cdot \nabla)U^* + 2\Omega^* \times U^* = -\frac{1}{\rho}\nabla\overline{p}^* + \nu\nabla^2 U^* \tag{2.11}$$

A non-dimensional formulation of these equations is convenient. The characteristic length is chosen as the hydraulic diameter at the inlet cross section which is defined as

$$D_h^* = \frac{4 \times Area}{Perimeter} \tag{2.12}$$

and the characteristic velocity is the mean normal velocity $v_0^*$ at the inlet surface $\Gamma_{in}$

$$v_0^* = \frac{1}{Area}\int_{\Gamma_{in}} n \cdot V^* ds \tag{2.13}$$

Using these characteristic dimensions, the following dimensionless variables are introduced

$$\begin{aligned} x &= \frac{x^*}{{D_h}^*}, \\ V &= \frac{V^*}{{v_0}^*}, \\ U &= \frac{U^*}{{v_0}^*}, \\ \Omega &= \frac{\Omega^*}{v_0^*/D_h^*}, \\ \overline{p} &= \frac{\overline{p}^* - p_0^*}{\frac{1}{2}\rho^* {v_0}^{*2}} \end{aligned} \tag{2.14}$$

With these definitions, equations (2.3–2.4) can be non-dimensionalized as

$$\nabla \cdot \boldsymbol{V} = 0 \tag{2.15}$$

$$(\boldsymbol{V} \cdot \nabla)\boldsymbol{V} = -\nabla \bar{p} + \frac{1}{Re}\nabla^2 \boldsymbol{V} \tag{2.16}$$

and for a rotating coordinate system, equations (2.10–2.11) as

$$\nabla \cdot \boldsymbol{U} = 0 \tag{2.17}$$

$$(\boldsymbol{U} \cdot \nabla)\boldsymbol{U} + 2\Omega \times \boldsymbol{U} = -\nabla \bar{\bar{p}} + \frac{1}{Re}\nabla^2 \boldsymbol{U} \tag{2.18}$$

where

$$Re = \frac{v_0 D_h}{\nu} \tag{2.19}$$

is the Reynolds number.

## 2.3 Vorticity-Potential Equations

There are generally two main difficulties related to the computation of incompressible flows. First, there is no evolution equation for the pressure and, second, the momentum equations must be solved subject to the continuity constraint. In two dimensions the vorticity-stream function method (Roache (1982)) is frequently used to overcome these difficulties. In such a formulation, the pressure is eliminated by cross differentiation over the momentum equations which yields a vorticity transport equation. Expressing

the velocity in terms of a stream function $\varphi$ ensuring that it is divergence free, the continuity equation is satisfied automatically. The reduced governing equations involve only one vorticity transport equation and one poisson equation for the stream function.

In three-dimensions, the pressure is also removed by cross differentiation of the momentum equations, but the introduction of the stream function is not straightforward. One approach is to replace the velocity by the vorticity and vector potentials. The reduced equations then involve three vorticity transport equations and three equations governing the vector potential components (see Aziz & Hellums (1967))

Based on a careful study by Hirasaki & Hellums (1968, 1970) and Richardson & Cornish (1977) on the boundary conditions, Yang & Camarero (1986, 1990) have shown that the scalar-vector potential formulation is suitable to simulate internal flows. The present study will incorporate most of their results and apply them to analyze the flow of multistage turbomachines. Details about the mathematical derivations of the scalar-vector potential representation (or dual potential formulation) can be found in Hirasaki & Hellums (1970) and Yang (1988). Here, we just briefly state the basic ideas and the final complete set of equation.

The basic idea of the scalar-vector potential method is a splitting of the velocity field into its rotational and irrotational parts which is based on the

Helmholtz's decomposition theorem. This theorem originally states that an arbitrary, bounded and continuously differentiable vector field $\boldsymbol{V}$ which is defined over the whole three-dimensional Euclidean space $R^3$ and vanishes at infinity can be expressed as

$$\boldsymbol{V} = -\nabla\phi + \nabla \times \boldsymbol{A} \tag{2.20}$$

where $\phi$ is the scalar potential and $\boldsymbol{A}$ is the vector potential of $\boldsymbol{V}$. Its generalization to an arbitrary subspace $\Omega \subset R^3$ and the related boundary conditions with regard to three-dimensional solution of Navier-Stokes equations are given and discussed in Richardson & Cornish (1977) and Wong & Reize (1986). The analytical formulation for solving the three-dimensional steady incompressible Navier-Stokes equations (equations 2.14-2.15) is detailed in the following.

### The problem specification

- The governing equations in primitive variables are (2.14) and (2.15).
- The flow domain is a bounded subspace $\Omega \subset \boldsymbol{R}^3$ with boundary $\partial\Omega$.
- The boundary conditions on the velocity field is

$$\boldsymbol{V} = \boldsymbol{v} \qquad on \quad \partial\Omega. \tag{2.21}$$

where $\boldsymbol{v}$ is such that

$$\int_{\partial\Omega} n \cdot \boldsymbol{v} ds = 0 \tag{2.22}$$

**Formula Derivation**

In general the velocity field can be decomposed into two parts

$$\boldsymbol{V} = -\nabla\phi + \nabla \times \boldsymbol{A} \tag{2.23}$$

where $\phi$ is a scalar potential field satisfying the Laplace equation

$$\nabla^2\phi = 0 \qquad in \quad \Omega \tag{2.24}$$

and $\boldsymbol{A}$ is a vector potential field which is chosen to be solenoidal(or divergence free)

$$\nabla \cdot \boldsymbol{A} = 0 \qquad on \quad \overline{\Omega} \tag{2.25}$$

and determined by the Poisson equation

$$\nabla^2\boldsymbol{A} = -\boldsymbol{W} \qquad in \quad \Omega \tag{2.26}$$

where

$$\boldsymbol{W} = \nabla \times \boldsymbol{V} \tag{2.27}$$

is the vorticity field.

Clearly, equation (2.23) ensures that the continuity equation (2.14) is automatically satisfied, since the divergence of the curl of any vector field is identically zero and the Laplace operator over any scalar field is equal to the divergence of the gradient of this scalar field.

Taking the curl on both side of equation (2.15) and using the continuity constraint (2.14) gives the following vorticity transport equation

$$(\boldsymbol{V}\cdot\nabla)\boldsymbol{W}-(\boldsymbol{W}\cdot\nabla)\boldsymbol{V} \;=\; \frac{1}{Re}\nabla^2\boldsymbol{W}. \tag{2.28}$$

Now the complete equation system in terms of the vorticity, scalar potential and vector potential can be written as follows

$$(\boldsymbol{V}\cdot\nabla)\boldsymbol{W}-(\boldsymbol{W}\cdot\nabla)\boldsymbol{V} \;=\; \frac{1}{Re}\nabla^2\boldsymbol{W} \tag{2.29}$$

$$\nabla^2\phi \;=\; 0 \tag{2.30}$$

$$\nabla^2\boldsymbol{A} \;=\; -\boldsymbol{W} \tag{2.31}$$

$$\boldsymbol{V} \;=\; -\nabla\phi+\nabla\times\boldsymbol{A} \tag{2.32}$$

For the application of the above equations within the rotor blade rows, it is necessary to describe them in a rotating frame of reference. Repeating the procedure previously applied to equations (2.17–2.18) yields

$$(\boldsymbol{U}\cdot\nabla)\boldsymbol{W}_R-(\boldsymbol{W}_R\cdot\nabla)\boldsymbol{U}-2(\Omega\cdot\nabla)\boldsymbol{U} \;=\; \frac{1}{Re}\nabla^2\boldsymbol{W}_R \tag{2.33}$$

$$\nabla^2\phi_R \;=\; 0 \tag{2.34}$$

$$\nabla^2\boldsymbol{A}_R \;=\; -\boldsymbol{W}_R \tag{2.35}$$

$$\boldsymbol{U} \;=\; -\nabla\phi_R+\nabla\times\boldsymbol{A}_R \tag{2.36}$$

The relations between the variables in stationary and rotating frame of references are given in Appendix A.

## 2.4 Curvilinear Coordinate Formulation

Body-fitted grids have one of the coordinate surfaces coinciding with the boundary of the physical domain so that irregular geometries can be transformed into regular computational domains. There are, basically, three techniques with which the body-fitted grid can be generated. They are the Conformal Mapping Technique, the Elliptic Differential Equation Technique and the Algebraic Technique. The last two are the most widely used techniques to generate body-fitted grid systems for the flow calculations in turbomachines.

The Elliptic Equation Method requires the solution of coupled Poisson equations in the computational domain and generally produces a smooth curvilinear coordinate system. But it is the most expensive method for generating body-fitted grids, especially for three-dimensional grids in the configuration of turbomachines.

The Algebraic Technique generates body-fitted grids by using algebraic functions instead of differential equations and is much more economical.

With a curvilinear coordinate system, the discretization of the governing equations and the programming of the code is an intricate task. To simplify such a problem both logically and mathematically, it is convenient to introduce a transformation with which the body-fitted grid in the physical domain is mapped into square grid in the computational domain.

The three-dimensional governing equations to be solved numerically total seven equations for seven unknowns. These equations include three vorticity transport equations, three poisson equations for the vector potential components and one Laplace equation for the scalar potential. Since they are second order elliptic partial differential equations, it is convenient to write them in one compact form as follows

$$\sum_{i=1}^{3} \frac{\partial^2 \varphi_j}{\partial x^i \partial x^i} + \sum_{i=1}^{3} c_j^i \frac{\partial \varphi_j}{\partial x^i} + c_j^0 \varphi_j = e_j \qquad j = 1,2,...,7 \tag{2.37}$$

where

$$\begin{aligned}
(\varphi_1, \varphi_2, \varphi_3, \varphi_4, \varphi_5, \varphi_6, \varphi_7) &= (w^1, w^2, w^3, A^1, A^2, A^3, \phi) \\
(c_1^0, c_2^0, c_3^0, c_4^0, c_5^0, c_6^0, c_7^0) &= (Re \frac{\partial u^1}{\partial x^1}, Re \frac{\partial u^2}{\partial x^2}, Re \frac{\partial u^3}{\partial x^3}, 0, 0, 0, 0) \\
(c_1^i, c_2^i, c_3^i, c_4^i, c_5^i, c_6^i, c_7^i) &= -(Re\, u^i, Re\, u^i, Re\, u^i, 0, 0, 0, 0) \\
(e_1, e_2, e_3, e_4, e_5, e_6, e_7) &= -(Re\, \sigma^1, Re\, \sigma^2, Re\, \sigma^3, w^1, w^2, w^3, 0)
\end{aligned} \tag{2.38}$$

with

$$\begin{aligned}
\mathbf{V} &= (u^1, u^2, u^3) \\
\mathbf{W} &= (w^1, w^2, w^3) \\
\mathbf{A} &= (A^1, A^2, A^3) \\
\mathbf{\Omega} &= (\Omega^1, \Omega^2, \Omega^3) \\
\sigma^k &= \sum_{i=1, i\neq k}^{3} w^i \frac{\partial u^k}{\partial x^i} + 2 \sum_{i=1}^{3} \Omega^i \frac{\partial u^k}{\partial x^i} \qquad k = 1,2,3
\end{aligned} \tag{2.39}$$

The velocity expression (2.32) can be rewritten as

$$\begin{aligned} u^1 &= -\frac{\partial \phi}{\partial x^1} + \frac{\partial A^3}{\partial x^2} - \frac{\partial A^2}{\partial x^3} \\ u^2 &= -\frac{\partial \phi}{\partial x^2} + \frac{\partial A^1}{\partial x^3} - \frac{\partial A^3}{\partial x^1} \\ u^3 &= -\frac{\partial \phi}{\partial x^3} + \frac{\partial A^2}{\partial x^1} - \frac{\partial A^1}{\partial x^2} \end{aligned} \tag{2.40}$$

As stated before, equations (2.37) must be transformed to the computational domain. The transformation that maps the physical domain onto the computational domain can be expressed as

$$\xi^i = \xi^i(x^1, x^2, x^3) \qquad i = 1,2,3 \tag{2.41}$$

By using the chain rule, for any scalar function $\varphi$, the following relations are deduced

$$\frac{\partial \varphi}{\partial x^i} = \beta_i^n \frac{\partial \varphi}{\partial \xi^n} \qquad i = 1,2,3 \tag{2.42}$$

$$\sum_{i=1}^{3} \frac{\partial^2 \varphi}{\partial x^i \partial x^i} = g^{mn} \frac{\partial^2 \varphi}{\partial \xi^m \partial \xi^n} + h^n \frac{\partial \varphi}{\partial \xi^n} \tag{2.43}$$

where

$$\beta_i^n = \frac{\partial \xi^n}{\partial x^i} \tag{2.44}$$

$$g^{mn} = \sum_{i=1}^{3} \frac{\partial \xi^m}{\partial x^i} \frac{\partial \xi^n}{\partial x^i} \tag{2.45}$$

$$h^n = \sum_{i=1}^{3} \frac{\partial^2 \xi^n}{\partial x^i \partial x^i} \tag{2.46}$$

Substituting (2.42–2.43) into equations (2.37) and (2.40) yields

$$g^{mn} \frac{\partial^2 \varphi_j}{\partial \xi^m \partial \xi^n} + (h^n + c_j^i \beta_i^n) \frac{\partial \varphi_j}{\partial \xi^n} + c_j^0 \varphi_j = e_j, \qquad j = 1,2,...,7 \tag{2.47}$$

and

$$
\begin{aligned}
u^1 &= -\beta_1^n \frac{\partial \phi}{\partial \xi^n} + \beta_2^n \frac{\partial A^3}{\partial \xi^n} - \beta_3^n \frac{\partial A^2}{\partial \xi^n} \\
u^2 &= -\beta_2^n \frac{\partial \phi}{\partial \xi^n} + \beta_3^n \frac{\partial A^1}{\partial \xi^n} - \beta_1^n \frac{\partial A^3}{\partial \xi^n} \\
u^3 &= -\beta_3^n \frac{\partial \phi}{\partial \xi^n} + \beta_1^n \frac{\partial A^2}{\partial \xi^n} - \beta_2^n \frac{\partial A^1}{\partial \xi^n}
\end{aligned}
\tag{2.48}
$$

These are the curvilinear form of equations (2.29–2.32).

## 2.5 Boundary Conditions

The vorticity-potential formulation of the Navier-Stokes equations leads to a difficulty in determining boundary conditions for the potentials. Any specified velocity on the boundaries does not imply a unique scalar and vector potentials. A set of compatible restrictions on the potentials must be imposed. Discussions about the admissible boundary conditions for the potentials can be found in the work of Hirasaki & Hellums (1968, 1970), Richardson & Cornish (1977), Wong & Reize (1984) and Yang & Camarero (1986)

It is convenient to use a local orthogonal curvilinear coordinate system $(\xi_{t_1}, \xi_{t_2}, \xi_n)$ on the boundaries instead of the cartesian coordinate (x,y,z), where $t_1, t_2$ denote the two tangential directions and $n$ the outward normal

direction. The expressions for gradient, divergence and cross product under this local system are given in Appendix $B$.

### 2.5.1 Scalar Potential Boundary Conditions

If the velocity is given on the boundaries, Hirasaki & Hellums (1970) proposed the following boundary condition for the scalar potential

$$\vec{\mathbf{n}} \cdot \nabla\phi = \frac{\partial\phi}{\partial n} = -\vec{\mathbf{n}} \cdot \boldsymbol{V} \tag{2.49}$$

The expression of the velocity (2.32) and equation (2.49) yield the following compatible condition for the vector potential

$$\vec{\mathbf{n}} \cdot (\nabla \times \boldsymbol{A}) = 0 \tag{2.50}$$

However such a condition is not sufficient to yield a unique vector potential. Additional conditions must be supplied. Hirasaki & Hellums (1970) have shown that the vector potential is unique if the following conditions

$$\vec{t}_1 \cdot \boldsymbol{A} = \vec{t}_2 \cdot \boldsymbol{A} = 0 \tag{2.51}$$

and

$$\nabla \cdot \boldsymbol{A} = 0 \tag{2.52}$$

are satisfied on the boundary surface. Richardson & Cornish (1977) have discussed its implementation to a multiple connected domain.

However, the vorticity-potential formulation with these conditions applies only to those problems with a known boundary velocity distribution. In such a case, the scalar potential equation

$$\begin{aligned} \nabla^2\phi &= 0 \\ \frac{\partial\phi}{\partial n} &= -\vec{n}\cdot\boldsymbol{V} \end{aligned} \tag{2.53}$$

can be solved independently. Otherwise, as mentioned by Wong & Reize (1984) and Aregbesola & Burley (1977), the scalar potential equation must be coupled with the vector potential and vorticity transport equations resulting in an increase of the computational time. For general flow problems, the velocity on all the boundaries cannot be always assumed to be known. An example is the three-dimensional duct flow with an arbitrary cross section where the exit velocity profile is not known a priori.

Another problem associated with these boundary conditions, as indicated by Wong & Reize (1984) and Yang & Camarero (1986), is that an inaccurate or even inconsistent scalar potential solutions will be encountered if $\phi$ exhibits high rate of local variations on the inlet or outlet planes. Indeed, such local variations exist when one imposes a parabolic velocity profile at the inlet or outlet of a rectangular duct.

In view of these difficulties, Yang & Camarero (1986) proposed an alternative way to impose the inlet and outlet conditions on the scalar potential. The right hand side of the Eq.(2.49) is replaced by the mean normal velocity

$$\frac{\partial \phi}{\partial n} = v_n \tag{2.54}$$

with

$$v_n = \frac{1}{Area(S)} \int_S \vec{\mathbf{n}} \cdot V \, ds \tag{2.55}$$

where $S$ is the inlet or outlet boundary surfaces.

If there is no flow across the boundary, for instance a solid wall, equation (2.54) becomes

$$\frac{\partial \phi}{\partial n} = 0 \tag{2.56}$$

Obviously, this condition requires that $\phi$ be solved only once and also highly decreases the local variation of $\phi$ on the boundaries.

### 2.5.2 Vector Potential Boundary Conditions

Since a Neumann boundary condition is used on the scalar potential at the inlet surface S equation (2.50) becomes

$$\vec{\mathbf{n}} \cdot (\nabla \times \boldsymbol{A}) = \vec{\mathbf{n}} \cdot \boldsymbol{V} - v_n = u_n \tag{2.57}$$

This condition, as mentioned before, is not sufficient to yield a unique solution. However, it is shown below that if there is a vector $\mathbf{E}$ normal to S that satisfies the differential equation

$$\vec{n} \cdot [(\nabla_s \times (\nabla_s \times \mathbf{E})] = u_n \tag{2.58}$$

then the vector defined by

$$\mathbf{A}_s = \nabla_s \times \mathbf{E} \tag{2.59}$$

satisfies equation (2.57) and is tangential to S. $\nabla_s$ is the surface gradient operator. Its expression in the local orthogonal coordinate system is given in Appendix *B*.

Indeed, if $\mathbf{E}$ is a solution to equation (2.58), since $\mathbf{E} = E_n\vec{n}$, then

$$\vec{n} \cdot \mathbf{A}_s = \vec{n} \cdot (\nabla_s \times \mathbf{E}) = 0 \tag{2.60}$$

This means $\mathbf{A}_s$ is tangential to S. From equation (2.60) and the expression of $\nabla_s$,

$$\begin{aligned} \vec{n} \cdot (\nabla \times \mathbf{A}_s) &= \vec{n} \cdot (\nabla_s \times \mathbf{A}_s) \\ &= \vec{n} \cdot [\nabla_s \times (\nabla_s \times \mathbf{E})] \\ &= u_n \end{aligned} \tag{2.61}$$

holds.

Now let $\mathbf{A}_s$ the tangential projection of $\mathbf{A}$ on the surface S, then

$$\vec{n} \cdot (\nabla \times \mathbf{A}) = \vec{n} \cdot (\nabla \times \mathbf{A}_s) = 0 \tag{2.62}$$

This shows that if one can solve equation (2.58), then one can get a solution to equation (2.57).

Equation (2.58) can be written in a direct form

$$\frac{\partial}{\partial \xi_{t_1}}[\frac{1}{h_{t_1}h_n}\frac{\partial}{\partial \xi_{t_1}}(h_nE_n)] + \frac{\partial}{\partial \xi_{t_2}}[\frac{1}{h_{t_2}h_n}\frac{\partial}{\partial \xi_{t_2}}(h_nE_n)] = -h_{t_1}h_nu_n \qquad (2.63)$$

This is a second order elliptic partial differential equation. To solve this equation, the necessary compatibility condition is

$$\begin{aligned}\int_S \vec{\mathbf{n}} \cdot [\nabla_s \times (\nabla_s \times \mathbf{E})]ds &= \int_S u_n ds \\ &= \int_S \vec{\mathbf{n}} \cdot \mathbf{V} ds - \int_S v_n ds \\ &= 0 \end{aligned} \qquad (2.64)$$

or

$$\oint_C (\nabla_s \times \mathbf{E}) \cdot d\vec{\mathbf{l}} = 0 \qquad (2.65)$$

must be satisfied, where $C$ is the contour of the surface $S$.

Expressed in the local coordinate system $(\eta_l, \eta_{n_c})$ on the surface $S$, where $\eta_l$ is the direction tangential to $C$ and $\eta_{n_c}$ is the outward normal direction to $C$, then we have

$$\begin{aligned}\nabla_s \times \mathbf{E} &= [\frac{1}{h_{t_2}}\frac{\partial}{\partial \xi_{t_2}}(h_nE_n)\vec{\mathbf{t}}_1 - [\frac{1}{h_{t_1}}\frac{\partial}{\partial \xi_{t_1}}(h_nE_n)\vec{\mathbf{t}}_2]/h_n \\ &= [\frac{1}{h_{n_l}}\frac{\partial}{\partial \eta_{n_l}}(h_nE_n)\vec{\mathbf{l}} - [\frac{1}{h_l}\frac{\partial}{\partial \eta_l}(h_nE_n)\vec{\mathbf{n}}_l]/h_n \end{aligned} \qquad (2.66)$$

A natural and simple specification for the boundary condition on $B =$

$h_n E_n$ to equation (2.63) requires that

$$\frac{\partial B}{\partial n_l} = 0 \tag{2.67}$$

so that the compatibility condition Eq.(2.65) is satisfied. Then the second order elliptic partial differential equation (2.63) with the Neumann boundary condition (2.67) permits a unique solution if one imposes a Dirichlet condition on $B$ at one point on the contour C.

With a solution $E_n$ to equation (2.63), the boundary condition on the vector potential $\mathbf{A}$ is easy to implement. Its tangential projection can be chosen as

$$\mathbf{A}_s = \nabla_s \times \mathbf{E} \tag{2.68}$$

or more specifically

$$\begin{aligned} A_{t_1} &= \frac{1}{h_{t_2} h_n} \frac{\partial}{\partial \xi_{t_2}} (h_n E_n) \\ A_{t_2} &= -\frac{1}{h_{t_1} h_n} \frac{\partial}{\partial \xi_{t_1}} (h_n E_n) \end{aligned} \tag{2.69}$$

The condition for the normal component of $\mathbf{A}$ can be deduced from

$$\nabla \cdot \mathbf{A} = 0 \tag{2.70}$$

or

$$\frac{\partial}{\partial \xi_{t_1}} (h_{t_2} h_n A_{t_1}) + \frac{\partial}{\partial \xi_{t_2}} (h_{t_1} h_n A_{t_2}) + \frac{\partial}{\partial \xi_n} (h_{t_1} h_{t_2} A_n) = 0 \tag{2.71}$$

Substituting (2.69) into Eq.(2.71), we have

$$\frac{\partial}{\partial \xi_n} (h_{t_1} h_{t_2} A_n) = 0 \tag{2.72}$$

If the boundary is a solid wall, the right hand side of equation (2.63) is zero, $E_n = 0$ is a solution to equation (2.63) and then (2.69) becomes

$$A_{t_1} = A_{t_2} = 0 \tag{2.73}$$

These coincides with (2.51), as given by Hirasaki & Hellums (1970). Again, the normal component has the same condition as (2.72).

Like the velocity, the vector potential cannot be assumed known a priori at the outlet. The following condition is used in the present study

$$\frac{\partial^2 \mathbf{A}}{\partial s^2} = 0 \tag{2.74}$$

where $s$ is the outward coordinate direction.

### 2.5.3 Vorticity Boundary Conditions

Values of vorticity at the wall are needed for the computation of the rotational flow. The wall vorticity generally can be computed from its definition or from a Taylor series expression of the vector potential (Roache 1982).

The Taylor series expression is used mostly for cartesian rectangular grid computation (see, for example, Wong & Reize 1984, Gerard 1989). In a curvilinear coordinate system, this approach leads to a very complicated

formulations of the wall vorticity expression in terms of the vector potential. So the definition

$$\mathbf{W} = \nabla \times \mathbf{V} \tag{2.75}$$

is used at the inlet and on solid walls. At the outlet, the first order derivative in the outward coordinate direction is set to

$$\frac{\partial \mathbf{W}}{\partial s} = 0 \tag{2.76}$$

### 2.5.4 Velocity Boundary Conditions

In the vorticity-potential method, velocity is not a primary variable, so it is used only to compute boundary conditions on derived variables, like the vorticity. In the present applications, the incoming velocity is given or updated from the passage-averaged velocity field. On the solid wall boundaries, the no-slip condition is used.

### 2.5.5 Summary of the Boundary Conditions

To summarize, the boundary conditions used for equations (2.29–2.32) are divided into three groups.

**Solid Wall Conditions:**

$$\frac{\partial \phi}{\partial n} = 0 \tag{2.77}$$

$$\mathbf{A}_s = 0, \quad \nabla \cdot \mathbf{A} = 0 \tag{2.78}$$

$$\boldsymbol{W} = \nabla \times \boldsymbol{V} \tag{2.79}$$

$$\boldsymbol{V} = 0 \tag{2.80}$$

**Inflow Conditions:**

$$\frac{\partial \phi}{\partial n} = v_n^i \tag{2.81}$$

$$\boldsymbol{A}_s = \nabla_s \times \boldsymbol{E}, \quad \nabla \cdot \mathbf{A} = 0 \tag{2.82}$$

$$\boldsymbol{W} = \nabla \times \boldsymbol{V} \tag{2.83}$$

$$\boldsymbol{V} \quad \text{extracted from the passage-averaged solution} \tag{2.84}$$

**Outflow Conditions:**

$$\frac{\partial \phi}{\partial n} = v_n^o \tag{2.85}$$

$$\frac{\partial^2 \boldsymbol{A}}{\partial s^2} = 0 \tag{2.86}$$

$$\frac{\partial \boldsymbol{W}}{\partial s} = 0 \tag{2.87}$$

where $v_n^i$, $v_n^o$ are the mean normal inlet and outlet velocities, $\boldsymbol{E}$ is a vector introduced in the previous sections and can be computed from Eq.(2.63). As indicated by Eq.(2.72), the conditions in (2.78) and (2.82), in the local orthogonal curvilinear coordinate system, become

$$A_{t_1} = A_{t_2} = 0, \tag{2.88}$$

$$\nabla \cdot \mathbf{A} = \frac{\partial(h_{t_1} h_{t_2} A_n)}{\partial \xi_n} = 0 \tag{2.89}$$

and

$$A_{t_1} = \frac{1}{h_{t_2} h_n} \frac{\partial}{\partial \xi_{t_2}} (h_n E_n), \tag{2.90}$$

$$A_{t_2} = -\frac{1}{h_{t_1} h_n} \frac{\partial}{\partial \xi_{t_1}} (h_n E_n), \tag{2.91}$$

$$\nabla \cdot \mathbf{A} = \frac{\partial(h_{t_1} h_{t_2} A_n)}{\partial \xi_n} = 0 \tag{2.92}$$

respectively.

# Chapter 3

# Passage-Averaged Governing Equations(PAGE)

## 3.1 Introduction

In the first section of this chapter, the passage-averaging operator and its properties are discussed. The passage-averaged formulation of equations (2.29–2.32) is presented in the second section.

## 3.2 Passage-Averaging Operator

This operator is an averaging procedure along the circumferential direction. It is applied throughout the flow domain, including the regions within both rotating and stationary blade rows. The general form of the averaging operator is

$$\bar{q} = \frac{1}{2\pi}\int_0^{2\pi} q d\theta \tag{3.1}$$

where $q$ can be a scalar or a vector. In the latter case, the integration is performed on each component of the vector.

The ratio of the angular distance of the region occupied by the fluid to the angular distance around the machine (i.e. $2\pi$ ) is a measure of the blockage attributed to the blade row. It will be used as a weighting function for the passage-averaging operator. Define the following functions

$$\theta_p = \theta_2 \tag{3.2}$$

$$\theta_s = \theta_1 + \frac{2\pi}{N} \tag{3.3}$$

as the angular position of the pressure surface ($\varphi_p^j$) and suction surfaces ($\varphi_s^j$) within the $j_{th}$ blade row, (see Figure 3.1), where $N$ is the number of blades in the jth blade row. Then, the blockage ratio is equal to

$$B = \frac{(\theta_s - \theta_p)N}{2\pi} \tag{3.4}$$

and the passage-averaging operator is defined as

$$\bar{q} = \frac{1}{2\pi B}\int_0^{2\pi} q(r,\theta,z)d\theta \tag{3.5}$$

It is noted that outside blade rows, (3.5) reduces to (3.1), since the blockage ratio is equal to 1.

Assuming a periodic flow field, the definition of the passage-average operator (3.5) can be simplified to

$$\bar{q} = \frac{1}{\theta_s - \theta_p}\int_{\theta_p}^{\theta_s} q d\theta \tag{3.6}$$

By introducing the following functions in a blade row

$$\lambda_s(r,\theta,z) = \theta - \theta_s(r,z) \tag{3.7}$$

$$\lambda_p(r,\theta,z) = \theta - \theta_p(r,z) \tag{3.8}$$

$$\lambda_c(r,\theta,z) = \theta - \theta_c(r,z) \tag{3.9}$$

the implicit equations defined by

$$\lambda_s(r,\theta,z) = 0 \tag{3.10}$$

$$\lambda_p(r,\theta,z) = 0 \tag{3.11}$$

$$\lambda_c(r,\theta,z) = 0 \tag{3.12}$$

represent the suction surface, pressure surface and camber surface respectively. From the definition of the blockage parameter $B$, we can get the following relationships

$$\theta_s = \theta_c + k(1+B)/2 \tag{3.13}$$

$$\theta_p = \theta_c + k(1-B)/2 \tag{3.14}$$

$$\delta = \theta_s(r,z) - \theta_p(r,z) \tag{3.15}$$

together with

$$\nabla\lambda_s = \nabla\lambda_c - \frac{k}{2}\nabla B \tag{3.16}$$

$$\nabla\lambda_p = \nabla\lambda_c + \frac{k}{2}\nabla B \tag{3.17}$$

where

$$k = \frac{2\pi}{N} \tag{3.18}$$

One can show that the passage-averaged form of the derivative of a function $q$ is given by

$$\overline{\frac{\partial q}{\partial x^i}} = \frac{1}{B}\frac{\partial (B\overline{q})}{\partial x^i} + \frac{1}{\delta}[q_s \frac{\partial \lambda_s}{\partial x^i} - q_p \frac{\partial \lambda_p}{\partial x^i}] \tag{3.19}$$

where $x^i$, (i = 1,2,3) represents any of the radial, circumferential or axial coordinate. From equation (3.19), it is possible to derive the following useful results

$$\overline{\nabla q} = \frac{1}{B}\nabla(B\overline{q}) + \frac{1}{\delta}[q_s \nabla\lambda_s - q_p \nabla\lambda_p] \tag{3.20}$$

$$\overline{\nabla \cdot \boldsymbol{V}} = \frac{1}{B}\nabla \cdot (B\overline{\boldsymbol{V}}) + \frac{1}{\delta}[\boldsymbol{V}_s \cdot \nabla\lambda_s - \boldsymbol{V}_p \cdot \nabla\lambda_p] \tag{3.21}$$

$$\overline{\nabla \times \boldsymbol{V}} = \frac{1}{B}\nabla \times (B\overline{\boldsymbol{V}}) + \frac{1}{\delta}[\nabla\lambda_s \times \boldsymbol{V}_s - \nabla\lambda_p \times \boldsymbol{V}_p] \tag{3.22}$$

## 3.3 Passage-Averaged Equations

To express the passage-averaged through-flow equations, equations (2.29–2.32) are averaged across the blade passage using the passage-averaging operator defined in (3.6) and the results of (3.20–3.22), leading to the following set of equations

$$(\overline{\boldsymbol{V}} \cdot \nabla)(B\overline{\boldsymbol{W}}) - (B\overline{\boldsymbol{W}} \cdot \nabla)\overline{\boldsymbol{V}} = \frac{1}{Re}\nabla^2(B\overline{\boldsymbol{W}}) + \boldsymbol{F}_W \tag{3.23}$$

$$\nabla^2(B\overline{\phi}) = F_\phi \tag{3.24}$$

$$\nabla^2(B\overline{\boldsymbol{A}}) = -B\overline{\boldsymbol{W}} + \boldsymbol{F}_A \tag{3.25}$$

$$B\overline{\boldsymbol{V}} = -\nabla(B\overline{\phi}) + \nabla \times (B\overline{\boldsymbol{A}}) + \boldsymbol{F}_V \tag{3.26}$$

where the over bar $(\bar{\cdot})$ represents averaged variables and the $F's$ are the external force terms whose expressions are given by

$$\begin{aligned}
\boldsymbol{F}_W = \frac{1}{Re\ k}\{ & \quad [\nabla(\boldsymbol{W}_s \cdot \nabla\lambda_s) - \nabla(\boldsymbol{W}_p \cdot \nabla\lambda_p)] \\
& - [\nabla \times (\nabla\lambda_s \times \boldsymbol{W}_s) - \nabla \times (\nabla\lambda_p \times \boldsymbol{W}_p)] \\
& - [\nabla\lambda_s \times (\nabla \times \boldsymbol{W})_s - \nabla\lambda_p \times (\nabla \times \boldsymbol{W})_p]\} \\
- \frac{1}{k}\{ & \quad \bar{\boldsymbol{V}}[\boldsymbol{W}_s \cdot \nabla\lambda_s - \boldsymbol{W}_p \cdot \nabla\lambda_p] \\
& + [\nabla\lambda_s \times (\boldsymbol{W} \times \boldsymbol{\Omega})_s - \nabla\lambda_p \times (\boldsymbol{W} \times \boldsymbol{\Omega})_p]\} \\
& - [\nabla \times (B\overline{\tilde{\boldsymbol{W}} \times \tilde{\boldsymbol{V}}}) + \bar{\boldsymbol{W}}(\nabla B \cdot \bar{\boldsymbol{V}})]
\end{aligned} \tag{3.27}$$

$$\boldsymbol{F}_V = -\frac{1}{k}[\phi_s \nabla\lambda_s - \phi_p \nabla\lambda_p] \tag{3.28}$$

$$F_\phi = \nabla \cdot \boldsymbol{F}_V \tag{3.29}$$

$$\begin{aligned}
\boldsymbol{F}_A = & -\nabla(\boldsymbol{A}_s \cdot \nabla\lambda_s - \boldsymbol{A}_p \cdot \nabla\lambda_p) \\
& -\frac{1}{k}[\nabla\lambda_s \times (\nabla \times \mathbf{A})_s - \nabla\lambda_p \times (\nabla \times \mathbf{A})_p]
\end{aligned} \tag{3.30}$$

where subscripts $(\cdot)_s$ and $(\cdot)_p$ represent the values of the variables on the suction surface and pressure surface respectively, and $(\tilde{\cdot})$ represents their perturbation component, for example, the velocity is written as

$$\boldsymbol{V} = \bar{\boldsymbol{V}} + \tilde{\boldsymbol{V}} \tag{3.31}$$

These perturbation terms are not necessarily small, and indeed they are not assumed to be small in this development.

# Chapter 4

# Modified Passage-Averaged Governing Equations(MPAGE)

## 4.1 Introduction

In the following section, an alternative system of equation for axisymmetric flows will be derived from the passage-averaged governing equations (3.23–3.26). These equations still have the passage-averaged form, but have only four equations for four unknowns, while in equations (3.23–3.26), there a total of seven equations and seven unknowns. The transformed equations in curvilinear coordinate system of these equations are given in the third section. Finally, boundary conditions are discussed in the last section of this chapter.

## 4.2 Alternative Equation System

### 4.2.1 Swirl Equation for Axisymmetric Flow

Many methods can be used for two-dimensional incompressible flow computations. The primitive variables method involves three equations for three unknowns, i.e. the continuity and two momentum equations for velocities u, v and pressure p. The dual potential method involves three equations for three unknowns. These equations and unknowns are the transport equation for vorticity $\varsigma$ and two Poisson equations for potentials $\phi$ and $A$. The velocity field is computed from the two potentials, while the vorticity-stream function method involves two equations for two unknowns.

In axisymmetric flow problem, the circumferential velocity $v^\theta$ in general is not zero, and the $\theta$-momentum equation is used to resolve this velocity component and completes the equation system. This equation is usually called the swirl equation and can be easily incorporated with the dual potential equations for axisymmetric flows. Simplifying the three-dimensional equations (2.29–2.32) to an axisymmetric configuration by setting $\frac{\partial}{\partial\theta} = 0$ yields

**Vorticity transport equation**

$$v^r\frac{\partial\varsigma}{\partial r} + v^z\frac{\partial\varsigma}{\partial z} - \frac{v^r}{r}\varsigma - \frac{1}{r}\frac{\partial}{\partial z}(v^\theta v^\theta) = \frac{1}{Re}\{\frac{\partial}{\partial r}[\frac{1}{r}\frac{\partial}{\partial r}(r\varsigma)] + \frac{\partial^2\varsigma}{\partial z^2}\} \qquad (4.1)$$

**$\phi$-Potential equation**

$$\frac{1}{r}\frac{\partial}{\partial r}(r\frac{\partial \phi}{\partial r}) + \frac{\partial^2 \phi}{\partial z^2} = 0 \tag{4.2}$$

**A-Potential equation**

$$\frac{\partial}{\partial r}[\frac{1}{r}\frac{\partial}{\partial r}(rA)] + \frac{\partial^2 A}{\partial z^2} = -\varsigma \tag{4.3}$$

**Swirl equation**

$$v^r\frac{\partial v^\theta}{\partial r} + v^z\frac{\partial v^\theta}{\partial z} + \frac{v^r v^\theta}{r} = \frac{1}{Re}\{\frac{\partial}{\partial r}[\frac{1}{r}\frac{\partial}{\partial r}(rv^\theta)] + \frac{\partial^2 v^\theta}{\partial z^2}\} \tag{4.4}$$

with

$$\begin{aligned} v^r &= -\frac{\partial \phi}{\partial r} - \frac{\partial A}{\partial z} \\ v^z &= -\frac{\partial \phi}{\partial z} + \frac{1}{r}\frac{\partial}{\partial r}(rA). \end{aligned} \tag{4.5}$$

The variables in the passage-averaged equations (3.23–3.26) are axisymmetric, i.e. depend on $r$ and $z$ only, and form a system of 7 equations in 7 unknowns. However, the system (4.1) to (4.5) involves only 4 equations and then is more economical. The next section shows how the passage-averaged form of (3.23–3.26) can be cast in a form similar to that of equations (4.1–4.5).

### 4.2.2 Modified Passage-Averaged Equations

To cast the passage-averaged equations (3.23–3.26) in the form of (4.1–4.4), the radial and axial velocities are written in terms of the scalar and vector potentials. This requires only the scalar potential $\bar{\phi}$ and the circumferential component of the vector potential $\bar{A}^\theta$ from the equation (3.26)

$$\begin{aligned} B\bar{v}^r &= -\frac{\partial(B\bar{\phi})}{\partial r} - \frac{\partial(B\bar{A}^\theta)}{\partial z} + F_v^r \\ B\bar{v}^z &= -\frac{\partial(B\bar{\phi})}{\partial z} + \frac{\partial(B\bar{A}^\theta)}{\partial r} + \frac{1}{r}(B\bar{A}^\theta) + F_v^z \end{aligned} \tag{4.6}$$

The scalar potential $\bar{\phi}$ can be solved independently by equation (3.24)

$$\frac{1}{r}\frac{\partial}{\partial r}[r\frac{\partial}{\partial r}(B\bar{\phi})] + \frac{\partial^2}{\partial z^2}(B\bar{\phi}) = F_\phi \tag{4.7}$$

To solve equation (3.25) for $\bar{A}^\theta$, only the circumferential vorticity $\bar{w}^\theta$ is required

$$\frac{\partial}{\partial r}[\frac{1}{r}\frac{\partial}{\partial r}(rB\bar{A}^\theta)] + \frac{\partial^2}{\partial z^2}(B\bar{A}^\theta) = -B\bar{w}^\theta + F_A^\theta \tag{4.8}$$

To solve the vorticity transport equation (3.23) for circumferential component $\bar{w}^\theta$,

$$\begin{aligned} \bar{v}^r\frac{\partial}{\partial r}(B\bar{w}^\theta) &+ \bar{v}^z\frac{\partial}{\partial z}(B\bar{w}^\theta) - \frac{\bar{v}^r}{r}(B\bar{w}^\theta) - \frac{1}{r}\frac{\partial}{\partial z}(B\bar{v}^\theta\bar{v}^\theta) \\ &= \frac{1}{Re}\{\frac{\partial}{\partial r}[\frac{1}{r}\frac{\partial}{\partial r}(rB\bar{w}^\theta)] + \frac{\partial^2}{\partial z^2}(B\bar{w}^\theta)\} \\ &+ F_w^\theta + S_w^\theta \end{aligned} \tag{4.9}$$

where

$$
\begin{aligned}
S_w^\theta \;=\; & [\frac{\partial(B\bar{v}^\theta)}{\partial r} + \frac{1}{r}B\bar{v}^\theta - \frac{r\omega}{k}(\frac{\partial\lambda_s}{\partial z} - \partial\lambda_p\partial z)]\frac{\partial\bar{v}^\theta}{\partial z} \\
& -[\frac{\partial(B\bar{v}^\theta)}{\partial z} + \frac{r\omega}{k}(\frac{\partial\lambda_s}{\partial z} - \frac{\partial\lambda_p}{\partial z})]\frac{\partial\bar{v}^\theta}{\partial r} \\
& +\frac{r\omega}{k}(\frac{\partial\lambda_s}{\partial z} - \frac{\partial\lambda_p}{\partial z})(\frac{1}{r}\bar{v}^\theta)
\end{aligned}
\tag{4.10}
$$

all three velocity components are required. For completeness, the circumferential velocity $\bar{v}^\theta$ needs to be resolved from additional relations.

In the previous chapter, four more unknowns, two vector potential components $\bar{A}^r$, $\bar{A}^z$ and two vorticity components $\bar{w}^r$, $\bar{w}^z$, were involved. However, to compute $\bar{v}^\theta$, these four unknowns are unnecessary. An alternative way to compute $\bar{v}^\theta$ is to use the swirl equation which can be derived from the three-dimensional $\theta$-momentum equation

$$
\begin{aligned}
\frac{1}{r}\frac{\partial}{\partial r}(rv^rv^\theta) \;+\; & \frac{1}{r}\frac{\partial}{\partial\theta}(v^\theta)^2 + \frac{\partial}{\partial z}(v^zv^\theta) + \frac{v^rv^\theta}{r} \\
= \; & -\frac{1}{r}\frac{\partial p}{\partial\theta} + \frac{1}{Re}\{\frac{\partial}{\partial r}[\frac{1}{r}\frac{\partial}{\partial r}(rv^\theta)] \\
+ \; & \frac{1}{r^2}\frac{\partial^2v^\theta}{\partial\theta^2} + \frac{2}{r^2}\frac{\partial v^r}{\partial\theta} + \frac{\partial^2v^\theta}{\partial z^2}\}
\end{aligned}
\tag{4.11}
$$

Applying the passage-averaging operator defined in chapter 2 to both sides of this equation yields the following

$$
\begin{aligned}
\bar{v}^r\frac{\partial}{\partial r}(B\bar{v}^\theta) \;+\; & \bar{v}^z\frac{\partial}{\partial z}(B\bar{v}^\theta) + \frac{\bar{v}^r}{r}(B\bar{v}^\theta) \\
= \; & \frac{1}{Re}\{\frac{\partial}{\partial r}[\frac{1}{r}\frac{\partial}{\partial r}(rB\bar{v}^\theta)] + \frac{\partial^2}{\partial z^2}(B\bar{v}^\theta)\} + F_v^\theta + S_v^\theta
\end{aligned}
\tag{4.12}
$$

where $F_v^\theta$ includes the viscous, geometrical effects of the blade surfaces and the perturbation term, $S_v^\theta$ represents the effects of the pressure jump between the pressure and suction surfaces within blade rows. These terms can be evaluated or integrated from the three-dimensional velocity field. Their expressions will be given later.

Now, the two potential equations (4.7, 4.8), the vorticity transport equation (4.9) and the swirl equation (4.12) together with the velocity expressions (4.6) form a complete set of equations. These equations are the passage-averaged equations equivalent to (4.1–4.4). To distinguish them from the previously developed equations (3.23–3.26), they will be called the Modified Passage-Averaged Equations.

The modified passage-averaged equations are summarized as follows

$$\begin{aligned} \bar{v}^r\frac{\partial}{\partial r}(B\bar{w}^\theta) &+ \bar{v}^z\frac{\partial}{\partial z}(B\bar{w}^\theta) - \frac{\bar{v}^r}{r}(B\bar{w}^\theta) - \frac{1}{r}\frac{\partial}{\partial z}(B\bar{v}^\theta\bar{v}^\theta) \\ &= \frac{1}{Re}\{\frac{\partial}{\partial r}[\frac{1}{r}\frac{\partial}{\partial r}(rB\bar{w}^\theta)] + \frac{\partial^2}{\partial z^2}(B\bar{w}^\theta)\} \\ &+ F_w^\theta + S_w^\theta \end{aligned} \tag{4.13}$$

$$\frac{1}{r}\frac{\partial}{\partial r}[r\frac{\partial}{\partial r}(B\bar{\phi})] + \frac{\partial^2}{\partial z^2}(B\bar{\phi}) = F_\phi \tag{4.14}$$

$$\frac{\partial}{\partial r}[\frac{1}{r}\frac{\partial}{\partial r}(B\bar{A}^\theta)] + \frac{\partial^2}{\partial z^2}(B\bar{A}^\theta) = -B\bar{W}^\theta + F_A^\theta \tag{4.15}$$

$$\begin{aligned} \bar{v}^r\frac{\partial}{\partial r}(B\bar{v}^\theta) &+ \bar{v}^z\frac{\partial}{\partial z}(B\bar{v}^\theta) + \frac{\bar{v}^r}{r}(B\bar{v}^\theta) \\ &= \frac{1}{Re}\{\frac{\partial}{\partial r}[\frac{1}{r}\frac{\partial}{\partial r}(rB\bar{v}^\theta)] + \frac{\partial^2}{\partial z^2}(B\bar{v}^\theta)\} \\ &+ F_v^\theta + S_v^\theta \end{aligned} \tag{4.16}$$

$$B\bar{v}^r = -\frac{\partial B\bar{\phi}}{\partial r} - \frac{\partial (B\bar{A}^\theta)}{\partial z} + F_v^r \tag{4.17}$$

$$B\bar{v}^z = -\frac{\partial B\bar{\phi}}{\partial z} + \frac{\partial (B\bar{A}^\theta)}{\partial r} + \frac{1}{r}(B\bar{A}^\theta) + F_v^z \tag{4.18}$$

where

$$\begin{aligned} F_w^\theta = \frac{1}{Re\ k} & \left\{ [\frac{1}{r}\frac{\partial}{\partial \theta}(\nabla\lambda_s \cdot \boldsymbol{W}_s - \nabla\lambda_p \cdot \boldsymbol{W}_p)] \right. \\ & - [\frac{\partial}{\partial z}(\frac{1}{r}(\frac{\partial \lambda_s}{\partial \theta} w_s^z - \frac{\partial \lambda_p}{\partial \theta} w_p^z) - (\frac{\partial \lambda_s}{\partial \theta} w_s^\theta - \frac{\partial \lambda_p}{\partial \theta} w_p^\theta)) \\ & - \frac{\partial}{\partial r}((\frac{\partial \lambda_s}{\partial r} w_s^\theta - \frac{\partial \lambda_p}{\partial r} w_p^\theta) - \frac{1}{r}(\frac{\partial \lambda_s}{\partial \theta} w_s^r - \frac{\partial \lambda_p}{\partial \theta} w_p^r))] \\ & - [(\frac{\partial \lambda_s}{\partial z}(\frac{1}{r}\frac{\partial w^z}{\partial \theta} - \frac{\partial w^\theta}{\partial z})_s - \frac{\partial \lambda_p}{\partial z}(\frac{1}{r}\frac{\partial w^z}{\partial \theta} - \frac{\partial w^\theta}{\partial z})_p) \\ & - (\frac{\partial \lambda_s}{\partial r}(\frac{1}{r} w^\theta - \frac{\partial w^\theta}{\partial r} - \frac{1}{r}\frac{\partial w^r}{\partial \theta})_s \\ & \left. - \frac{\partial \lambda_p}{\partial r}(\frac{1}{r} w^\theta - \frac{\partial w^\theta}{\partial r} - \frac{1}{r}\frac{\partial w^r}{\partial \theta})_p)] \right\} \\ -\frac{1}{k} & \left\{ \bar{v}^\theta [\nabla\lambda_s \cdot \boldsymbol{W}_s - \nabla\lambda_p \cdot \boldsymbol{W}_p] \right. \\ & \left. - r\omega[(\frac{\partial \lambda_s}{\partial z} w_s^z - \frac{\partial \lambda_p}{\partial z} w_p^z) + (\frac{\partial \lambda_s}{\partial r} w_s^r - \frac{\partial \lambda_p}{\partial r} w_p^r)] \right\} \\ - & \left\{ \frac{\partial}{\partial z}(B\overline{\tilde{w}^\theta \tilde{v}^z} - B\overline{\tilde{w}^z \tilde{v}^\theta}) - \frac{\partial}{\partial r}(B\overline{\tilde{w}^r \tilde{v}^\theta} - B\overline{\tilde{w}^\theta \tilde{v}^r}) \right. \\ & \left. - \bar{w}^\theta [\frac{\partial B}{\partial r}\bar{v}^r + \frac{\partial B}{\partial z}\bar{v}^z] \right\} \end{aligned} \tag{4.19}$$

$$\begin{aligned} F_A^\theta = -\frac{1}{k} & \left\{ [\frac{1}{r}\frac{\partial}{\partial \theta}(\nabla\lambda_s \cdot \boldsymbol{A}_s - \nabla\lambda_p \cdot \boldsymbol{A}_p)] \right. \\ & + [(\frac{\partial \lambda_s}{\partial z}(\frac{1}{r}\frac{\partial A^z}{\partial \theta} - \frac{\partial A^\theta}{\partial z})_s - \frac{\partial \lambda_p}{\partial z}(\frac{1}{r}\frac{\partial A^z}{\partial \theta} - \frac{\partial A^\theta}{\partial z})_p] \\ & - [\frac{\partial \lambda_s}{\partial r}(\frac{1}{r} A^\theta - \frac{\partial A^\theta}{\partial r} - \frac{1}{r}\frac{\partial A^r}{\partial \theta})_s \\ & \left. - \frac{\partial \lambda_p}{\partial r}(\frac{1}{r} A^\theta - \frac{\partial A^\theta}{\partial r} - \frac{1}{r}\frac{\partial A^r}{\partial \theta})_p] \right\} \end{aligned} \tag{4.20}$$

$$
\begin{aligned}
F_v^\theta \;=\; & \frac{1}{Re\ k}\ \Big\{\Big[\frac{\partial\lambda_s}{\partial r}\Big(\Big(\frac{\partial v^\theta}{\partial r}\Big)_s - \frac{1}{r}v_s^\theta\Big) - \frac{\partial\lambda_s}{\partial r}\Big(\Big(\frac{\partial v^\theta}{\partial r}\Big)_s - \frac{1}{r}v_s^\theta\Big)\Big] \\
& + \frac{1}{r}\Big[\frac{\partial\lambda_s}{\partial\theta}\Big(\frac{\partial v^\theta}{\partial\theta}\Big)_s - \frac{\partial\lambda_p}{\partial\theta}\Big(\frac{\partial v^\theta}{\partial\theta}\Big)_p\Big] \\
& + \Big[\frac{\partial\lambda_s}{\partial z}\Big(\frac{\partial v^\theta}{\partial z}\Big)_s - \frac{\partial\lambda_p}{\partial z}\Big(\frac{\partial v^\theta}{\partial z}\Big)_p\Big] \\
& + r\omega\Big[\frac{\partial}{\partial r}\Big(\frac{\partial\lambda_s}{\partial r} - \frac{\partial\lambda_p}{\partial r}\Big) - \frac{\partial}{\partial z}\Big(\frac{\partial\lambda_s}{\partial z} - \frac{\partial\lambda_p}{\partial z}\Big)\Big]\Big\} \\
- \quad & \Big\{\frac{2}{r}B\overline{\tilde{v}^r\tilde{v}^\theta} + \frac{\partial}{\partial r}\big(B\overline{\tilde{v}^r\tilde{v}^\theta}\big) + \frac{\partial}{\partial z}\big(B\overline{\tilde{v}^z\tilde{v}^\theta}\big) \\
& - \bar{v}^\theta\Big[\frac{\partial B}{\partial r}\bar{v}^r + \frac{\partial B}{\partial z}\bar{v}^z\Big]\Big\}
\end{aligned}
\tag{4.21}
$$

$$
F_\phi \;=\; -\frac{1}{k}\nabla\cdot(\phi_s\nabla\lambda_s - \phi_p\nabla\lambda_p) \tag{4.22}
$$

$$
F_v^r \;=\; -\frac{1}{k}\Big(\frac{\partial\lambda_s}{\partial r}\phi_s - \frac{\partial\lambda_p}{\partial r}\phi_p\Big) \tag{4.23}
$$

$$
F_v^z \;=\; -\frac{1}{k}\Big(\frac{\partial\lambda_s}{\partial z}\phi_s - \frac{\partial\lambda_p}{\partial z}\phi_p\Big) \tag{4.24}
$$

$$
\begin{aligned}
S_w^\theta \;=\; & \Big[\frac{\partial(B\bar{v}^\theta)}{\partial r} + \frac{1}{r}B\bar{v}^\theta - \frac{r\omega}{k}\Big(\frac{\partial\lambda_s}{\partial z} - \frac{\partial\lambda_p}{\partial z}\Big)\Big]\frac{\partial\bar{v}^\theta}{\partial z} \\
& - \Big[\frac{\partial(B\bar{v}^\theta)}{\partial z} + \frac{r\omega}{k}\Big(\frac{\partial\lambda_s}{\partial z} - \frac{\partial\lambda_p}{\partial z}\Big)\Big]\frac{\partial\bar{v}^\theta}{\partial r} \\
& + \frac{r\omega}{k}\Big(\frac{\partial\lambda_s}{\partial z} - \frac{\partial\lambda_p}{\partial z}\Big)\Big(\frac{1}{r}\bar{v}^\theta\Big)
\end{aligned}
\tag{4.25}
$$

$$
S_v^\theta \;=\; B\overline{D_p} \tag{4.26}
$$

with

$$
\begin{aligned}
D_p \;=\; & \frac{1}{Re}\Big[\frac{\partial}{\partial r}\Big(\frac{1}{r}\frac{\partial v^\theta}{\partial r}\Big) + \frac{\partial^2 v^\theta}{\partial z^2}\Big] \\
& - \Big[\frac{1}{r}\frac{\partial}{\partial r}(rv^rv^\theta) + \frac{\partial}{\partial z}(v^zv^\theta) + \frac{1}{r}v^rv^\theta\Big]
\end{aligned}
\tag{4.27}
$$

## 4.3 Curvilinear Coordinate Formulation

In the modified passage-averaged equations, (4.13–4.18), all derivatives with respect to the circumferential direction are zero. The (r,z) coordinate system is chosen in which r represents the radial direction and $z$ represents the axial direction. In this coordinate system, the governing equations (4.13–4.16) for the vorticity, circumferential velocity and two potentials can be rewritten in the following compact form

$$\frac{\partial^2\psi_j}{\partial r^2} + \frac{\partial^2\psi_j}{\partial z^2} + d_j^r\frac{\partial\psi_j}{\partial r} + d_j^z\frac{\partial\psi_j}{\partial z} + d_j^0\psi_j = g_j \qquad j = 1,2,3,4 \quad (4.28)$$

where

$$\begin{aligned}
(\psi_1,\ \psi_2,\ \psi_3,\ \psi_4) &= (B\bar{w}^\theta,\ B\bar{v}^\theta,\ B\bar{\phi},\ B\bar{A}^\theta) \\
(d_1^0,\ d_2^0,\ d_3^0,\ d_4^0,) &= (Re\,\frac{\partial\bar{v}^r}{\partial r} - \frac{1}{r^2},\ Re\,\frac{\bar{v}^r}{r} - \frac{1}{r^2},\ 0,\ -\frac{1}{r^2}) \\
(d_1^r,\ d_2^r,\ d_3^r,\ d_4^r) &= (\frac{1}{r} - Re\,\bar{v}^r,\ \frac{1}{r} - Re\,\bar{v}^r,\ \frac{1}{r},\ \frac{1}{r}) \\
(d_1^z,\ d_2^z,\ d_3^z,\ d_4^z) &= (-Re\,\bar{v}^z,\ -Re\,\bar{v}^z,\ 0,\ 0) \qquad (4.29) \\
(g_1,\ g_2,\ g_3,\ g_4) &= (-Re(F_W^\theta + S_W^\theta),\ -Re(F_V^\theta + S_V^\theta),\ F_\phi,\ F_A^\theta - B\bar{w}^\theta)
\end{aligned}$$

The transformation to the computational domain can be represented as

$$\begin{aligned}
\xi &= \xi(r,z) \\
\eta &= \eta(r,z) \qquad (4.30)
\end{aligned}$$

then the curvilinear form of equations (4.28) is

$$\alpha\frac{\partial^2\psi_j}{\partial\xi^2}-2\beta\frac{\partial^2\psi_j}{\partial\xi\partial\eta}+\gamma\frac{\partial^2\psi_j}{\partial\eta^2}+\lambda_j^{\xi}\frac{\partial\psi_j}{\partial\xi}+\lambda_j^{\eta}\frac{\partial\psi_j}{\partial\eta}+\lambda_j^{0}\psi_j = J^2 g_j \qquad j = 1,2,3,4 \tag{4.31}$$

where

$$\alpha = \left(\frac{\partial z}{\partial\eta}\right)^2+\left(\frac{\partial r}{\partial\eta}\right)^2, \tag{4.32}$$

$$\beta = \frac{\partial z}{\partial\xi}\frac{\partial z}{\partial\eta}+\frac{\partial r}{\partial\xi}\frac{\partial r}{\partial\eta}, \tag{4.33}$$

$$\gamma = \left(\frac{\partial z}{\partial\xi}\right)^2+\left(\frac{\partial r}{\partial\xi}\right)^2, \tag{4.34}$$

$$J = \frac{\partial z}{\partial\xi}\frac{\partial r}{\partial\eta}-\frac{\partial z}{\partial\eta}\frac{\partial r}{\partial\xi}, \tag{4.35}$$

$$\begin{aligned}\Lambda^{\xi} &= (\lambda_1^{\xi},\ \lambda_2^{\xi},\ \lambda_3^{\xi},\ \lambda_4^{\xi})\\ \Lambda^{\eta} &= (\lambda_1^{\eta},\ \lambda_2^{\eta},\ \lambda_3^{\eta},\ \lambda_4^{\eta})\\ \Lambda^{0} &= (\lambda_1^{0},\ \lambda_2^{0},\ \lambda_3^{0},\ \lambda_4^{0})\end{aligned} \tag{4.36}$$

with

$$\begin{aligned}\lambda_j^{\xi} &= J^2\tau + J\left(\ d_j^z\frac{\partial r}{\partial\eta}-d_j^r\frac{\partial z}{\partial\eta}\right),\\ \lambda_j^{\eta} &= J^2\sigma + J\left(-d_j^z\frac{\partial r}{\partial\xi}-d_j^r\frac{\partial z}{\partial\xi}\right),\\ \lambda_j^{0} &= J^2 d_j^0 \qquad\qquad j = 1,2,3,4\end{aligned} \tag{4.37}$$

and

$$\begin{aligned}\tau &= \frac{\partial^2\xi}{\partial r^2}+\frac{\partial^2\xi}{\partial z^2}\\ \sigma &= \frac{\partial^2\eta}{\partial r^2}+\frac{\partial^2\eta}{\partial z^2}\end{aligned} \tag{4.38}$$

For equations (4.17–4.18), one have

$$
\begin{aligned}
B\bar{v}^r &= \frac{1}{J}\left[\frac{\partial z}{\partial \eta}\frac{\partial (B\bar{\phi})}{\partial \xi} - \frac{\partial z}{\partial \xi}\frac{\partial (B\bar{\phi})}{\partial \eta}\right] \\
&\quad -\frac{1}{J}\left[\frac{\partial r}{\partial \eta}\frac{\partial (B\bar{A}^\theta)}{\partial \xi}\right] - \frac{\partial r}{\partial \xi}\frac{\partial (B\bar{A}^\theta)}{\partial \eta}\Big] + F_v^r \\
B\bar{v}^z &= \frac{1}{J}\left[\frac{\partial r}{\partial \eta}\frac{\partial (B\bar{\phi})}{\partial \xi} - \frac{\partial r}{\partial \xi}\frac{\partial (B\bar{\phi})}{\partial \eta}\right] \\
&\quad \frac{1}{J}\left[\frac{\partial z}{\partial \eta}\frac{\partial (B\bar{A}^\theta)}{\partial \xi}\right] - \frac{\partial z}{\partial \xi}\frac{\partial (B\bar{A}^\theta)}{\partial \eta}\Big] + \frac{1}{r}(B\bar{A}^\theta) + F_v^z \qquad (4.39)
\end{aligned}
$$

## 4.4 Boundary Conditions

The domain of the passage-averaged flow in a multistage turbomachinery configuration is the meridional plane. The inlet is located somewhere upstream of the first blade row, and the exit is located downstream of the last blade row. In the present applications for the incoming flow velocity field, a uniform profile is used. To make it compatible with the no-slip wall conditions, the value at the wall is set to zero. The velocity condition on solid boundaries is the no-slip condition and the vorticity is computed from the velocity.

Noting that there is no flow across the hub and shroud, the boundary condition on the scalar potential is

$$\frac{\partial \phi}{\partial n} = 0 \qquad (4.40)$$

The passage-averaging integration over the scalar potential across the pitch leads to the same condition on the averaged scalar potential

$$\frac{\partial \bar{\phi}}{\partial \bar{n}} = 0 \tag{4.41}$$

where $\bar{n}$ is the outward normal vector for passage-averaged flow domain. The inlet and outlet conditions for scalar potential are specified by the corresponding mean normal velocities.

As discussed in the previous chapter, the vector potential **A** has zero tangential projections on the hub and shroud. Since the circumferential component of vector potential $A^\theta$ is tangential to the hub and shroud, it is always zero on these end-walls. This implies that the passage-averaged variable $\bar{A}^\theta$ is zero on these wall boundaries. At the inlet, the component $A^\theta$ is chosen to be zero also since a uniform velocity profile is assumed, then $\bar{A}^\theta$ remains zero at the inlet.

To summarize, boundary conditions for the modified passage-averaged governing equations (4.13–4.16) belong to the following groups.

**Solid Wall Conditions:**

$$\frac{\partial \bar{\phi}}{\partial \bar{n}} = 0 \tag{4.42}$$

$$\bar{A}^\theta = 0 \tag{4.43}$$

$$B\bar{w}^\theta = \frac{\partial (B\bar{v}^r)}{\partial z} - \frac{\partial (B\bar{v}^z)}{\partial r} \tag{4.44}$$

$$\bar{v}^\theta \qquad \text{no-slip condition} \tag{4.45}$$

**Inflow Conditions:**

$$\frac{\partial \bar{\phi}}{\partial \bar{n}} = \bar{v}_n^i \tag{4.46}$$

$$\bar{A}^\theta = 0 \tag{4.47}$$

$$B\bar{w}^\theta = \frac{\partial (B\bar{v}^r)}{\partial z} - \frac{\partial (B\bar{v}^z)}{\partial r} \tag{4.48}$$

$$\bar{v}^\theta \qquad \text{given} \tag{4.49}$$

**Outflow Conditions:**

$$\frac{\partial \bar{\phi}}{\partial \bar{n}} = \bar{v}_n^o \tag{4.50}$$

$$\frac{\partial^2 (B\bar{A}^\theta)}{\partial \bar{s}^2} = 0 \tag{4.51}$$

$$\frac{\partial (B\bar{w}^\theta)}{\partial \bar{s}} = 0 \tag{4.52}$$

$$\frac{\partial (B\bar{v}^\theta)}{\partial \bar{s}} = 0 \tag{4.53}$$

where $\bar{v}_n^i$ and $\bar{v}_n^o$ are the average normal inlet and outlet velocities respectively.

# Chapter 5

# Coupling Between the 3DGE and the MPAGE

## 5.1 Introduction

The proposed model to simulate the interaction of the flow in a rotor-stator stage of a turbomachine consists of two sets of equations; the three-dimensional governing equations (3DGE) and the modified passage-averaged governing equations (MPAGE). The 3DGE are used within each blade region to provide the three-dimensional flow fields, while the MPAGE are used to achieve the link in an average sense of these flow fields through the passage-averaged flow field. The coupling between these two sets of equations and the data flow from each other will be described in this chapter.

## 5.2 Data Flow from the 3DGE to the MPAGE

The passage-averaged equations (4.13–4.18) have the same form as the axisymmetric flow equations (see, for example, Equations (4.1–4.4)) with the addition of external force terms which incorporate the three-dimensional effects into the MPAGE.

Outside the blade passages, the flow is taken to be axisymmetric and these external force terms are zero. Within the blade passages, they are computed from the 3DGE solutions. Most of these terms use only the values of the 3DGE solutions on the pressure and suction surfaces, while some terms, like $\overline{\tilde{\mathbf{W}} \times \tilde{\mathbf{V}}}$ require integration of the 3DGE solutions across the blade passage. All these terms can be computed explicitly and the calculations can be performed outside the 3DGE and MPAGE solvers. The input data are the geometry parameters and the 3DGE solutions. The output data are the external force terms which are needed for solving the MPAGE. The expressions are given by (4.19–4.27).

## 5.3 Data Flow from the MPAGE to the 3DGE

Since the Three-dimensional governing equations (2.29–2.32) are derived from steady, incompressible Navier-Stokes equations, this is a pure boundary

value problem. In duct flow problems, the inlet boundary conditions are problem dependent and can be imposed differently, but all other boundary conditions are developed by the flow physics. It is clear also that, from the formulation of 3DGE, to solve these equations, the only required information is the inlet velocity distribution.

To specify an accurate three-dimensional inlet velocity profile is very difficult and even impossible for a general configuration. However, in the present study, since the flow is taken to be axisymmetric outside the blade rows, the inflow conditions at the entrance of each blade row are also axisymmetric. The passage-averaged velocity can be used as inlet velocity profile. These inlet velocities are updated by the MPAGE solutions.

In summary, the iterative cycle between th 3DGE and the MPAGE can be described as follows.

- The inlet conditions for the 3DGE computation at the entrances of each blade rows are computed from the MPAGE solutions.
- The 3-D flow fields within each blade rows are solved.
- The external force terms in (4.19–4.27) are calculated from the updated 3DGE solutions.
- The MPAGE are solved again with updated external force terms.

# Chapter 6

# Solution Procedure

## 6.1 Introduction

Two different methods have been used to solve the Poisson equations for the potentials. The first one is the Line Relaxation Method, and the second is a direct Method. The line relaxation method solver has been developed by Yang (1988) and modified for the present application. The implicit method (or direct method) is presented in sections 6.3. Some practical experiences in using these methods are given in section 6.4. In sections 6.5 through 6.7, the global algorithms for the 3DGE and the MPAGE as well as the computational procedure to the interaction of the 3DGE and the MPAGE will be described.

## 6.2 Line Relaxation Method

One well-known overrelaxation method is the successive (point) overrelaxation (SOR) method developed by Frankel (1950) and Young (1954). The

convergence rate of the SOR method can be improved by successive line over-relaxation (Line SOR) method. It uses the tridiagonal algorithm implicitly solving the equations line-by-line. In the present three-dimensional applications, the relaxation sweep proceeds in the k-direction, section by section. Within each section, the sweep proceeds in the j-direction, line-by-line. When the sweep is at row $(j_0, k_0)$, the previous rows at $(j_0 - 1)$ and $(k_0 - 1)$ have been already solved for (n+1) values. The row $(j_0, k_0)$ is then solved implicitly along the i-direction using Thomas tridiagonal algorithm.

The relaxation factor is required to lie in the range, $0 < \omega < 2$. For convergence, over-relaxation is required for solving scalar and vector potential equations. Under-relaxation should be used for the solution of the vorticity transport equation.

## 6.3 Fully Implicit Method

In the present study, it is required to solve the scalar potential Laplace equation only once, in an arbitrarily shaped three-dimensional duct with Neumman boundary conditions. As remarked by Gary (1967) and Dorr (1969), the convergence rate for Line SOR method can be very slow with Neumann boundary conditions even on a rectangular domain. The experience (this will be discussed in the following section) with Line SOR method

on a domain with curved boundaries also shows convergence may be dramatically slowed down or may even diverge with increasing boundary curvature variation and the skewness of the local curvilinear coordinates. To avoid these drawbacks, an implicit method is proposed in the present investigations.

To solve Poisson type equations, some efficient direct methods and solvers have been developed. The papers by Dorr (1970) and Lancaster (1970) reviewed these methods and a computer program has been published by King (1976). However, most of these methods are limited to rectangular domains and cartesian coordinate systems. Recently, Algorithm to solve a global matrix equation have been developed by Page et al.(1989). These subroutines use the skyline technique to store the global matrix and the LU factorization method for the resolution of the equation system.

These subroutines are used for solving the finite difference equations of the scalar and vector potentials. The vorticity transport equations are solved by line under-relaxation method. The scalar potential Laplace equation need to be solved only once, while the vector potential equations are coupled with the vorticity equation by the source term. They must be solved in an iterative way. Since the vector potential equations are linear Poisson equations, the global matrix remains the same within the iteration procedure. Only the source term is updated after each iteration. Then the most expensive part of the calculations in the implicit solver, the LU factorization, is performed

only once. The forward elimination and backward substitution are repeated in the iterative procedure.

It should be pointed out that the scalar potential equation with Neumman boundary conditions everywhere on the boundary allows an infinite number of solutions. The discretized equations, together with the boundary conditions will lead to a singular global matrix. In order to obtain a unique solution and ensure a non-singular global matrix, a Dirichlet boundary condition is imposed at one boundary point.

## 6.4 Scalar Potential Test

As indicated by Gary (1967) and Dorr (1969), the convergence rate for Line SOR iterative method of Poisson equation with Neumann boundary conditions is much slower than that with Dirichlet boundary conditions. This had been experienced only on a rectangle. Applying the Line SOR method to solve Poisson equation with Neumann boundary conditions on three-dimensional curved ducts has also shown that the convergence rate strongly depends on the boundary curvature and the nonorthogonality of the curvilinear coordinate system.

In the test problems, the domain is chosen as a curved duct with unit square cross section. The length along the z-direction is four units. A uniform

grid is used and the boundary conditions on the scalar potential $\phi$ are

$$\frac{\partial \phi}{\partial z} = 1 \qquad on \quad k = 1 \tag{6.1}$$

$$\frac{\partial \phi}{\partial z} = -1 \qquad on \quad k = kmax \tag{6.2}$$

$$\frac{\partial \phi}{\partial z} = 0 \qquad elsewhere \tag{6.3}$$

The coordinates are generated as follows.

$$x(i,j,k) = (i-1)\delta x \tag{6.4}$$

$$y(i,j,k) = (j-1)\delta y + \alpha \sum_{l=1}^{k} \left(\frac{l-1}{kmax-1}\right)^2 \tag{6.5}$$

$$z(i,j,k) = (k-1)\delta z \tag{6.6}$$

with

$$\delta x = \frac{1}{imax-1}, \quad \delta y = \frac{1}{jmax-1}, \quad \delta z = \frac{1}{kmax-1} \tag{6.7}$$

where imax, jmax and kmax are the maximum grid size on x-, y- and z-directions respectively. $\alpha$ is a factor used to specify the curvature variation of the boundaries (j=1 and j=jmax) and the skewness of the coordinate system. Several sectional domains with different values of $\alpha$ are shown in Figure 6.1 to demonstrate the variation of the boundary curvature and the skewness.

The results after 1000 iterations for a 11x11x21 grid are presented in Table 6.1. The history of convergence for the scalar potential test problems are shown in Figure 6.2. For comparison, computations with the direct method

Table 6.1: Scalar potential test using Line SOR method

| After 1000 iterations | | | | | |
|---|---|---|---|---|---|
| | Log( ) | | Mass Cons. | Relax. | CPU time |
| $\alpha$ | Residue | $\|\phi^{n+1} - \phi^n\|$ | (%) | $\omega$ | (s) |
| 0.05 | -2.302 | -4.719 | 0.336 | 1.5 | 31.71 |
| 0.10 | -1.667 | -4.138 | 1.323 | 1.4 | almost the same |
| 0.20 | -1.116 | -3.751 | 4.951 | 1.3 | almost the same |
| 0.30 | -0.650 | -3.465 | 10.106 | 1.3 | almost the same |
| $\geq 0.35$ | Diverge | | | | |

are also performed and the results are given in Table 6.2.

Table 6.1 and Figure 6.1 show that, for a small factor $\alpha$, say $\alpha < 0.1$, the convergence using Line SOR method is relatively fast and the accuracy for volumetric flows is acceptable. With the increase of the factor $\alpha$, the convergence becomes very slow and it is very difficult to converge with $\alpha = 0.3$. For values of $\alpha$ exceeding 0.35, the method diverges. On the other hand, the direct method always gives a solution and the volumetric flow errors in Table 6.2 show that the results are acceptable for values of $\alpha$ up to 0.5.

These tests were not intended to be an exhaustive study of numerical methods for solving Poisson equation. The specific tests for the scalar potential were only carried out to assess the Line SOR solver and the implicit solver. The implicit method never encountered convergence problems, and

Table 6.2: Scalar potential test using implicit method

| $\alpha$ | Log( ) Residue | Mass Conservation (%) | CPU time (s) |
|---|---|---|---|
| 0.05 | -11.587 | 0.118 | 24.14 |
| 0.10 | -11.576 | 0.420 | almost the same |
| 0.20 | -11.568 | 1.363 | almost the same |
| 0.30 | -11.542 | 2.440 | almost the same |
| 0.50 | -11.350 | 4.407 | almost the same |

provides more accurate results than the Line SOR method. The computer time is also acceptable for a great number of mesh points (for example, with about 10000 mesh points, the CPU time on a 3090 IBM machine is about 4 minutes. Of course, as the number of mesh points increases, the computer time and storage requirement will also increase. With a very large number of mesh points, the implicit method may not be economical.

## 6.5 Global Algorithm for the 3DGE

As mentioned before, the computation of the scalar potential can be separated from the coupling of vorticity and vector potential, so that the scalar potential equation needs only be solved once. But the vector potential and vorticity are coupled to each other by the source term in the vector potential

equations, the convective terms in the vorticity transport equations and the boundary conditions. A cycling procedure is used for this coupling. The global algorithm is given in the following:

1. Specification of boundary conditions.

2. Computation of scalar potential using equation (2.34).

3. Computation of vorticity using the vorticity transport equation (2.33)

4. Computation of vector potential using equation (2.35) and the updated vorticity field.

5. Calculation of velocity field using equation (2.36) and the updated vector potential.

6. Stop if the convergence criteria are satisfied. Otherwise, go back to step 3.

## 6.6 Global Algorithm for the MPAGE

The vorticity transport equation, swirl equation and the Poisson equation for the potential $\bar{A}^{\theta}$ are coupled by the convective terms in the vorticity equation and swirl equation, the source terms in the vorticity equation and the potential equation. These equations are solved with the procedure which is described as follows:

1. Computation of the scalar potential to provide irrotational potential velocity field.

2. Computation of vorticity field using vorticity transport equation.

3. Computation of potential $\bar{A}^{\theta}$ using updated vorticity field.

4. Calculation of new velocity field using updated potential $\bar{A}^{\theta}$.

5. Computation of circumferential velocity using the swirl equation.

6. Stop if the convergence criteria are satisfied. Otherwise, go back to step 2.

## 6.7 Global Computational Procedure

The Global algorithm proposed in this study consists of two parts: the 3DGE solver within the blade rows and the MPAGE for the stage coupling. The computations for these two parts are coupled and performed in an iterative way. The global computational procedure is described below:

1. Generation of body-fitted grids for the 3DGE and the MPAGE domains.

2. Preparation of the geometry parameters and external force terms. Generally the external forces are taken to be zero.

3. Computation of the MPAGE to produce a passage-averaged through flow solution.

4. Computation of the 3DGE to provide three-dimensional solutions within the blade passages.

5. Calculation of the external forces using the updated 3DGE solutions.

6. Go back to step 3 until the residues of the MPAGE satisfy an acceptable limit.

# Chapter 7

# Validations

## 7.1 Introduction

The proposed model for the rotor-stator interactions in a turbomachine, and the resulting governing equations, the 3DGE and the MPAGE, have been implemented in a Fortran computer program. To validate this approach, numerical results for several simple flow problems are presented, the numerical predictions are compared with the available analytical and experimental results. To validate the interaction between the 3DGE and the MPAGE, the more realistic problem of an impeller with planar blades is investigated.

## 7.2 Validation for the 3DGE

### 7.2.1 Developing Flow in a Straight duct

The development of a laminar flow in a rectangular duct is a simple three-dimensional internal flow for which analytical solution and experimental results are available for comparison. The duct geometry, illustrated in Figure 7.1, with aspect ratio $\gamma = b/a = 1$, i.e. with square cross section, was first computed. Constant spacing was used in the two transverse x- and y-directions, with 15x15 points, and 23 points were stretched in the streamwise z-direction as follows.

$$z(k+1) = z(k) + dz(k) \qquad k = 1, 2, ..., n \tag{7.1}$$

with

$$dz(k) = \frac{\alpha - 1}{\alpha^n - 1} \alpha^{k-1} L \tag{7.2}$$

$$\alpha = 1.0618 \tag{7.3}$$

$$n = 22 \tag{7.4}$$

The Reynolds number, based on the hydraulic diameter $D_h$ is defined by

$$D_h = \frac{4ab}{a+b} \tag{7.5}$$

was chosen to be $Re = 100$. To ensure a fully developed flow at the exit, the duct length L was set to

$$L = 0.105\, D_h\, Re \tag{7.6}$$

based on the discussion on the entrance length by Han (1960). On the inlet plane, a uniform flow was specified with $v_x = v_y = 0$, and $v_z = 1$ (note that $v_z$ is set to zero at walls to satisfy the no-slip condition).

The predicted velocity along the central plane distributions in the developing region are shown in Figure 7.2a at several sections. Figure 7.2b shows the velocity profiles taken along the duct diagonal, i.e. with the coordinates x=y. These velocity profiles are compared with the analytical solution of Han (1960) and with the experimental data of Goldstein & Kreid (1967). The agreement between them is very good.

The predicted fully developed streamwise velocity profiles are presented in Figure 7.3, and the comparison with the analytical solutions of Han (1960) shows that the agreement is excellent.

The predicted centerline velocity is compared with the analytical and experimental results in Figure 7.4. The agreement between them is good.

The second computed duct has an aspect ratio $\gamma = 0.5$ and the grid used is 15x13x25. Again, the two transverse directions are uniformly spaced and the streamwise direction is stretched according to Eq.(7.2) with the stretch

factor $\alpha = 1.03$. The Reynolds number is $Re = 100$ and a uniform velocity profile is used on the inlet plane. The duct length is set to

$$L = 0.08\, D_h\, Re \tag{7.7}$$

The predicted developing velocity profiles are shown in Figure 7.5. Figure 7.5b presents velocity profiles in the vertical direction, and Figure 7.5a presents profiles across the horizontal direction. The fully developed velocities are shown in Figure 7.6 for both profiles across the width and height and the predicted centerline velocity development is displayed in Figure 7.7. These velocity profiles are compared with the analytical results of Han (1960) and the experimental data of Sparrow et al. (1967). Good agreement between them can be observed.

### 7.2.2 Developing Flow in Curved duct

The second test problem was the development of a laminar incompressible viscous flow in a curved duct with square cross section. The principal characteristic of such a flow is the presence of longitudinal curvature which generates secondary flows resulting in distortion of the streamwise velocity. The computation of curved duct flows usually serves as a model problem for understanding some of the important features in turbomachinery flows.

The duct geometry is illustrated in Figure 7.8. The centerline curvature $R_c$ of the curved duct is 14 times the duct width $D$. The Dean number K defined by

$$K = Re\,(\frac{D_h}{R_c})^{1/2} \tag{7.8}$$

is 55 corresponding to a Reynolds number of 206, based on the hydraulic diameter $D_h$ defined by equation (7.5). The turning angle is 110°. On a transverse cross section, 15 points are uniformly spaced in the radial direction and 13 on the width and 25 points were stretched in the streamwise direction (angular distance $\phi$) as indicated in Eq.(7.2) with $\alpha = 1.05$. At the entrance of the duct, a uniform streamwise velocity profile ($u_\zeta = 1$) and zero transverse velocities ($u_\xi = u_\eta = 0$) were specified.

Figure 7.9 shows the development of the streamwise velocity profiles in the mid-plane parallel to the top and bottom walls. The profiles in Figure 7.9b, along the vertical direction, remain symmetric as they should on the vertical mid-surface. The profiles in Figure 7.9a, along the horizontal direction, become more asymmetric as the flow develops downstream. This can be explained by the centrifugal force generated by the longitudinal curvature which forces the peak value of the velocity profile towards the outer wall of the duct.

In Figure 7.10, the predicted velocity profiles at the cross section with angular position $\theta = 102.4°$ are chosen for comparison with the fully devel-

oped flow predicted by Ghia & Sokhey (1977) and Cheng et al. (1975), and with the experimental data of Mori et al. (1971). The present calculations and the previous numerical predictions agree very well while the comparison between the numerical results and experimental data is not so good.

Figure 7.11 shows the secondary flow development as the flow proceeds downstream. The vortices start between $\phi = 5.07^o$ and $\phi = 16.8^o$ and developed toward the outer wall. There is no significant change after $\theta = 63.9^o$.

## 7.3 Validation of the MPAGE

### 7.3.1 Developing Flow in Channels

The first test is the developing flow between two parallel plates, in which the through flow program is used to evaluate the accuracy and stability of the present scheme. The coordinate system is chosen as cartesian and the calculation is made for a channel with a length-to-width ratio $L/D = 10$, a Reynolds number $Re = 50$ based on the inlet velocity and the channel width. The grid used for this computation is 49x15. The inlet velocity is assumed uniform and the developed velocity profile is given in Figure 7.12. The exit velocity is compared with the analytical solution

$$u(y) = 6(y - y^2) \tag{7.9}$$

The numerical solution agrees well with the analytical one.

The second test is the developing axisymmetric flow between two cylinders with ratios of the inner radius to width $r_1/D = 0.5$, and of the outer radius to width $r_2/D = 1.5$ and of the length to width $L/D = 10$. The Reynolds number, based on the width and the inlet velocity, is also $Re = 50$. The grid is 49x15. Here, the cylindrical coordinate system is used and a uniform velocity profile is specified at the inlet location. The computed axisymmetric velocity profile at the outlet is compared with the developed analytical solution expressed as follows

$$u_z(r) = -A_p[r^2 - \frac{(D_2^2 - D_1^2)Ln(2r/D_1)}{4Ln(D_2/D_1)} - \frac{D_1^2}{4}] \tag{7.10}$$

with

$$D_1 = 2\,r_1, \quad D_2 = 2\,r_2$$

$$A_p = \frac{32Q}{\pi D_2^4\,[(1-(D_1/D_2)^2)(1+(D_1/D_2)^2) + \frac{(1-(D_1/D_2)^2)^2}{Ln(D_1/D_2)}]} \tag{7.11}$$

where $Q$ is the mass flux across the annular section. Figure 7.13 shows that the agreement between the solutions is quite good.

### 7.3.2 Flow in a Rotating Annulus

To validate the approach for a rotating configuration, the next test is performed in a rotating annulus. Its geometrical parameters are indicated

in Figure 7.14a, the ratio of the inner radius to width is $r_1/D = 1.5$ and the ratio of the outer radius to width is $r_2/D = 2.5$. The inlet velocity is set to zero and the inner and outer walls rotate with specified angular velocity $\omega_1$ and $\omega_2$ respectively.

The computed axisymmetric tangential velocity is also compared with the analytical solution given by the following formula

$$u_\theta(r) = \frac{r(\omega_2 r_2^2 - \omega_1 r_1^2) - r_1^2 r_2^2(\omega_2 - \omega_1)/r}{r_2^2 - r_1^2} \tag{7.12}$$

Figure 7.14b shows the tangential velocity with $\omega_1 = 0.5, \omega_2 = 0.0$, Figure 7.14c shows the result with $\omega_1 = 1.0, \omega_2 = 0.0$ and Figure 7.14d presents the solution with $\omega_1 = 0.3, \omega_2 = -0.3$. All of these calculated velocities are in excellent agreement with the analytical solutions.

### 7.3.3 Flow in Rectangular Duct

Another test problem is a rectangular duct geometry representing the configuration of a blade row with parallel plates $y = \pm b$ as the two neighbour blades. This means that the plate $y = -b$ represents the suction surface of one blade and the plate $y = +b$ represents the pressure surface of the next blade, while the other two parallel sides $x = \pm a$ represent the inner wall and the outer shell of the blade passage between the two blades (see Figure

7.1). The coordinate system here is chosen as cartesian instead of cylindrical. An analytical solution given by Han (1960) in the form of an axial velocity profile is available for comparison. This represents the smooth transition from a uniform profile to a fully developed one.

The passage-average technique is applied to this expression and the analytical averaged solution including the velocity and shear force can be obtained for comparison with the computed averaged solutions(see Appendix $C$). The numerical solutions are calculated with aspect ratio $\gamma = \frac{b}{a} = 1.0$, 0.5 and 0.25. The Reynolds number, based on the inlet velocity and the hydraulic diameter defined by equation (7.5), is $Re = 100$ for these tests. The computations were carried out using three uniformly spaced grids, 15x15x31, 15x13x31 and 15x11x31, with aspect ratios $\gamma = 1.0$, 0.5 and 0.25 respectively. The profiles of the passage-average velocities and shear forces are presented at several sections.

From the velocity profiles shown in Figure 7.15, one can observe that the numerical solution is concave along the central line near the inlet region, while the analytical solution is not. This behaviour remains even with grid refinement near the inlet.

Such a discrepancy between analytical and numerical solutions is due to the fact that Han's solution is simply an approximation. In his development, some of the convection terms were neglected using a technique introduced by

Langhaar (1942). More precisely, it was assumed that the convection term is replaced by

$$u_x\frac{\partial u_z}{\partial x}+u_y\frac{\partial u_z}{\partial y}+u_z\frac{\partial u_z}{\partial z}\cong u_z\frac{\partial u_z}{\partial z} \tag{7.13}$$

Then the remaining term is linearized as

$$u_z\frac{\partial u_z}{\partial z}=\nu\beta u_z \tag{7.14}$$

where the parameter $\beta$ is assumed to be a function of the axial distance $z$ only and its values have been tabulated by Han (1960). However we know that the term

$$u_x\frac{\partial u_z}{\partial x}+u_y\frac{\partial u_z}{\partial y} \tag{7.15}$$

is not identically zero near the inlet region, especially within the boundary layer. Therefore this will result in some difference between Han's result and the present numerical solutions near the inlet region.

For completeness, the following heuristic analysis is presented. We divide the convection term as follows

$$I=u_x\frac{\partial u_z}{\partial x}+u_y\frac{\partial u_z}{\partial y}+u_z\frac{\partial u_z}{\partial z}=I_1+I_2 \tag{7.16}$$

with

$$I_1=u_x\frac{\partial u_z}{\partial x}+u_y\frac{\partial u_z}{\partial y},\qquad I_2=u_z\frac{\partial u_z}{\partial z} \tag{7.17}$$

From the boundary conditions and the symmetric property, it is clear that

$$I_1=0,\quad \begin{matrix}\text{when} & x=0;\ \pm a\\ \text{or} & y=0;\ \pm b\end{matrix} \tag{7.18}$$

While, from the boundary layer theory, we have

$$I_1 > 0, \qquad \text{elsewhere,} \tag{7.19}$$

this means that the difference

$$I_1 = I - I_2 \geq 0, \qquad \text{everywhere} \tag{7.20}$$

and reaches its maximum at the four points where the real velocity $u_z$ with respect to $I$ is larger than Han's analytical velocity with respect to $I_2$. At the same time they must satisfy the continuity equation and the boundary conditions, thus $u_z$ must be smaller than the analytical value on the central line (i.e. $x = 0$, or $y = 0$).

The shear forces are the slopes of the velocities $u_z, u_z^h$ on the boundaries (i.e. $y = \pm b$). Their contributions to the passage-averaged $z$-momentum equation are their differences $f_z, f_z^h$ between two boundaries (i.e. $y = -b$ and $y = b$). The shear force distributions are presented in Figure 7.16. From the above discussion, it is expected that

$$f_z \leq f_z^h \qquad \text{near the inlet region} \tag{7.21}$$

see Figure 7.17 in which the 15x11x31 grid generated by distributing points uniformly along $x$- and $y$-direction with a ratio of the nearby $dz$ of $dz_{i+1}/dz_i = 1.071$.

Note that such properties will also hold for the passage-averaged variables. The above discussion gives us some information as to why the numerical

velocity has such a concave profile and why the numerical shear force is smaller than the analytical one near the inlet region. It seems that the numerical solution is more realistic.

Figure 7.16 shows the shear force profiles in which the comparison between the computed results and the approximate analytical solutions is reasonable except for a value of the aspect ratio $\gamma = 0.25$ near the leading edge($\xi = 0.033$). It is expected that with a refined grid, this would be improved. However, for higher aspect ratio, $\gamma \geq 0.5$, the approximation is good.

### 7.3.4 Flow in an Impeller with Planar Blades

A more realistic computation is a test problem with a flow passage containing a rotor with planar blades. The geometry is divided into three regions as shown in Figure 7.18. The first one is the entrance region where a uniform inlet velocity develops axially toward a rotor. The second region is the rotor blade channel with 21 blades and the third one is the discharge region downstream of the rotor.

For the through-flow computation, the grid sizes were 21x15 for the entrance region, 21x31 for the blade region and the 21x21 for discharge region.

The grid size for internal flow computation was 21x15x31. In the blade region, the hub radius varies from 0.5 to 1.0, the height of the blade varies from 0.5 to 0.25 and the area of the grid sections varies from 0.112 to 0.135.

In this test problem, the non-dimensional uniform inlet velocity was chosen as $v_i = 1.0$. In order to gain a better understanding of the effects of blades, rotation and viscosity, the numerical results are presented into three groups. The first group shows the blade effects in which the through-flow solutions with and without the external forces are presented (Figure 7.19). In the second group, the computations were carried out with fixed Reynolds number Re = 100, and the angular velocities were chosen to be 0.0, 0.5 and 1.0. Both passage-averaged solutions and averaged three-dimensional internal flow solutions are presented and distinguished by line and symbol profiles (Figure 7.20). While in the third group, the computations were carried out by changing the Reynolds number to 100, 300 and 500, but with fixed angular velocity $\omega = 0.5$ (Figure 7.21).If one considers, for example, a machine with $v_i^0 = 25$ m/sec as its inlet velocity and with $r_1^0 = 0.5$m and $r_2^0 = 1.0$m as the radii of its inner wall and outer shell respectively at the inlet location, then the rotating speed of the rotor is approximately 746 r.p.m. with the non-dimensional angular velocity chosen as $\omega = 1.0$.

The development of the secondary flow along the rotor passage, the velocity vectors of the three-dimensional solution at several hub-to-shroud planes

are presented in Figure 7.22 for Re = 100 and $\omega = 1.0$. Some streamwise ribbon patterns are shown in Figure 7.23 to illustrate the recirculating nature of the flow.

Without the action of the rotor, the field is simply an axisymmetric flow with zero tangential velocity. Otherwise, the field is perturbed by the blade boundary layer, the end-wall boundary layer and the pressure jump between the pressure side and suction side of the blades. Figure 7.19 shows the difference between them, in which the passage-averaged axial, radial and tangential velocity distributions at several hub-to-shroud sections are presented. From them one can observe that, within the rotor, the boundary layer has a greater effect near the hub than near the shroud because the blades are closer. The tangential velocity develops gradually as the hub radius increases along the rotor passage and is attenuated rapidly in the discharge region.

Figure 7.20 shows the dramatic effects of rotation. With the increase of the rotational speed of the blade passage, the increase of the tangential velocity is significant and their profiles are roughly proportional. Because the tangential velocity is mainly generated by the hub and shroud boundary layers and the pressure difference between two blade surfaces, such effects are dominated by the rotational speed for a given Reynolds number. The profiles of the axial and radial velocities also change due to the secondary flow. The main feature of the secondary flow, in this test problem, is the fixed shroud

within the rotor. This, of course, will be affected strongly by the rotational speed of the rotor. It should be noted that the effects of the fixed shroud also depends on the Reynolds number. In fact, as it increases, this leads to a decrease of the effects of the fixed shroud. These can be observed in Figure 7.21.

Figures 7.20 and 7.21 also show that the passage-averaged solutions and the averaged three-dimensional internal flow solutions agree well except for the tangential velocity near the inlet of the rotor because of very sharp changes in that region. However, these small acceptable differences confirmed again that the prediction of the external forces from the internal computation is accurate enough for simulating the most dominant properties of the flow in an impeller.

# Chapter 8

# Applications to a Rotor-Stator Stage

## 8.1 Introduction

Using the approach developed in the previous chapters, numerical investigations were performed to the flow of a mixed-flow pump. The numerical predictions are presented in this chapter and are compared with experimental data provided by Carey et al. (1985a, 1985b).

## 8.2 Description of the NEL Pump

The NEL model pump is a mixed-flow machine. Its cross section through the axis of the machine is illustrated in Figure 8.1. This pump includes a rotor/impeller and a stator/diffuser. There are no inlet guide-vanes. The fluid enters the pump axially through the inlet, proceeds directly into the rotor, exits from the rotor outlet, and there its follows a unbladed passage in

which the flow is turned from the outward direction towards the stator and is diffused into a outlet duct.

There are five rotor blades and nine stator blades. The rotor outlet diameter, measured from the axis to the centre of the blade trailing edge, is $D_t$ = 430mm and the maximum internal shroud diameter is 536mm. The hub and shroud have conical geometries. The cone half-angles of the hub and shroud are 32.3° and 17.6° for the rotor, and −20.6° and −11.4° for the stator respectively. The details of the physical dimensions of the blades and a general description of the pump facility are given in Carey et al. (1985a).

The measurements reported by Carey et al. (1985b) were performed in a air model of the machine at a shaft speed 1200 r.p.m. of the impeller. The experimental data for all velocities are normalized by the blade velocity at the midpoint of the rotor trailing edge, which is $U_t = 27m/s$ at 1200 r.p.m., corresponding to a Reynolds number of Re=1.5x$10^6$.

The meridional cross-section for the passage-averaged through-flow computation is shown in Figure 8.2, which is divided into five regions along the streamwise direction. The first region from $s = 0$ to $s = 1.0$ is the flow entrance zone, the second region from $s = 1.0$ to $s = 2.0$ is the blade passage of the rotor, the third region from $s = 2.0$ to $s = 3.0$ is the unbladed passage between the rotor and the stator, the fourth region from $s = 3.0$ to $s = 4.0$ is the blade passage of the stator and the fifth and final region from $s = 4.0$ to

$s = 5.0$ is the discharge zone of the machine. No tip clearance was considered in these tests. The three-dimensional domain for the rotor and stator blade passages are illustrated in Figs. 8.3a and 8.3b. A grid of 59x13 was used for the MPAGE computation with 13 points in the radial direction. In the streamwise direction, 7 points were used in the first region, 15 points in the second region, 11 points in the third region, 21 points in the fourth region and 9 point in the final region respectively with constant spacing within each region (see Figure 8.4). There were 15 points spaced uniformly in the circumferential direction for the rotor and 13 points for the stator. The grids used for the 3DGE computations are shown in Figure 8.5a and 8.5b.

The inlet flow profile was specified based on the flow rate 1.01 $m^3/s$ corresponding to the best efficiency $\eta = 87\%$.

Since the present study is for laminar flow, the Reynolds number for the computation was 1500 based on the characteristic length $D_t$ and velocity $U_t$.

## 8.3 Numerical Predictions

### 8.3.1 Rotor Three-Dimensional Results

Because of the complex geometry of the annular flow passage in the pump and in order to compare the velocity distribution with the experimental data

in Carey et al. (1985b), as they did in their report, the results are plotted in terms of the following velocity components as illustrated in Figure 8.6

- $V_p$ – The velocity component parallel to the streamwise grid line.
- $V_n$ – The velocity component normal to the streamwise grid line.
- $W_t$ – The tangential velocity component in the relative rotating frame of reference.

In order to show the development of the boundary layers, secondary flows and the effects of the relative motion of the shroud, three stations are chosen to present the predicted velocity field. These three stations are located near the inlet ($s = 0.07$), at the mid-chord ($s = 0.5$) and near the outlet ($s = 0.86$) as indicated in Figure 8.7.

Surfaces plots of these three velocity components are plotted in Figs. 8.8, 8.9 and 8.10 respectively at the above stations. The blade-to-blade velocity distributions which are numbered in Figure 8.7, are shown in Figs. 8.11 through 8.13 with comparisons against the experimental data in Carey et al. (1985b).

These blade-to-blade velocity vector fields are also shown in Figure 8.14 which are accompanied by the same vector fields based on the measurement. Figure 8.15 shows the cross-stream flows of the rotational part of the relative

velocity field, i.e. the velocity

$$V_A = V + \nabla\phi \;=\; \nabla \times \mathbf{A} \tag{8.1}$$

at the three passage stations.

At first sight, Figs. 8.8 through 8.14 show the main features of the flow development through the rotor. There is a steady acceleration of the flow because of the contraction of the annular flow area. The growth of blade surface boundary layers are significant, while the hub boundary layer is less significant. This agrees with the observation by the experimenters who stated that "It was found that viscous effects were relatively unimportant to the flow in the inner annular" and "the hub boundary layer was found to be too thin for observation...". It should be mentioned that, since the absence of an appropriate turbulence model and a much lower Reynolds number, these boundary layers are much thicker and discrepancies with the measurement as should be expected.

In the mainstream flow region (with $R < 0.7$, where R is a normalized parameter with values within the interval [0,1] measured from hub to shroud), the velocity component $V_p$ near the pressure surface of the blade is accelerated more rapidly than that near the suction surface. While the relative tangential component $W_t$ near the suction surface is accelerated more rapidly than that near the pressure surface due to the change of geometry of the rotor. These

agree well with the experimental data except those at the edge of the blade boundary layers. There, the predicted velocities are relatively higher than measured the ones. Such differences may be caused by a much thicker blade boundary layer which squeezes the mainstream flow toward the mid-pitch.

In the near shroud region, including R=0.833 and R=0.917, complex turbomachinery flow phenomena are encountered. The blade boundary layers, the shroud boundary layer, the effects of the relative motion of the shroud and the associated secondary flow interacts to generate rapid changes in the fluid behaviour. It is evident that there is a discrepancy between the predictions and the measurements for velocity components $V_p$ and $W_t$ shown in Figs. 8.11 and 8.12.

The main reason for such a discrepancy is probably the exclusion of the effects of the gap between blade and shroud in the present numerical modeling. The tip leakage flow is a jet flow, as explained by Carey and his co-authors, "is directed forwards across the blade tip and becomes entrained in the suction flow, adding to its volume and momentum". So that a bulge in component $V_p$ and an increment in the component $W_t$ close to the suction surface can be expected as shown in Figs. 8.11 and 8.12 for the experimental results. When the flow proceeds downstream, the tip leakage flow will meet and interact with blade and shroud boundary layers, giving rise to a mixing region. This mixing process will further move away from the suction surface

due to the relative movement between the blade and shroud and the secondary flows. These flow phenomena are illustrated in Figure 8.16. Without the tip leakage flow, the shroud boundary layer will play an important role in the outer annular region. Indeed, the numerical predictions in Figs. 8.11 and 8.12 show that, downstream of the rotor passage, the boundary layer decelerated the flow close to the suction surface, while near the pressure surface, the flow is accelerated by the moving shroud and blade boundary layer scraping.

The cross-stream flows are shown in Figure 8.15. These flows are mainly induced by secondary flows which are generally due to the relative motion of the shroud and the curvature changes of the blade passage. It is the curvature effects that causes the through flow vortex to move from the near corner of the shroud and pressure side to the near corner of the hub and suction side. If the blade passage were a straight duct, the relative motion would drive the vortex to the shroud-pressure side corner as in a driven cavity. It is observed that in the corner of the shroud and pressure blade surface, there is a small scraping vortex (see Figure 8.15c) which is believed to be the result of the relative movement between the shroud and the blade.

### 8.3.2 Stator Three-Dimensional Results

Like the rotor, the results of the stator are plotted in terms of the same velocity components, except that the absolute tangential velocity component is used instead of the relative one, as the stationary frame of reference is used for the stator.

- $V_p$ – The velocity component parallel to the streamwise grid line.
- $V_n$ – The velocity component normal to the streamwise grid line.
- $V_t$ – The tangential velocity component in the stationary frame of reference.

Figure 8.17 through 8.19 show the three-dimensional surface plots of these three velocity components at three chosen stations $s = 3.1$, $s = 3.5$ and $s = 3.9$. Figs. 8.20 through 8.21 present the blade-to-blade velocity distributions with the corresponding numbering in Figs. 8.17, 8.18 and 8.19 respectively. The blade-to-blade velocity vector fields are shown in Figure 8.23 and the cross-flows of the rotational part of the velocity expressed by (8.1) are shown in Figure 8.24.

From Figs. 8.17 through 8.21, one can see that the boundary layer development in the stator passage, for both blade surfaces and the end-walls, is more significant than in the rotor passage, as the passage of the stator is much longer than that of the rotor. Because of the conically inward shaped

hub and shroud and the presence of the pressure surface of the blade, the mainstream flow develops toward the region near the pressure surface and the shroud as shown in Figure 8.17. These have been also shown in Figure 8.20, in which the velocity component $V_p$ is almost symmetric near the inlet($s = 3.1$), when the flow proceeds downstream, it is accelerated in the region near the pressure surface and shroud, but decelerated in the region near the suction surface and the hub.

Another important feature of the flow in the stator is that, as shown in Figure 8.21, the tangential velocity $V_t$ is reduced very rapidly along the passage. Near the hub and exit region, the tangential velocity even becomes positive. This behavior is as expected, since the function of a diffuser (the stator in the present pump model) is to reduce the high velocity in order to convert the kinetic energy to static pressure (see, Shepherd 1956). Although a quantitative comparison with measurement is not available, the revealed flow features by the numerical prediction are reasonable and quite encouraging. One can also see that, from Figure 8.21, the deceleration of the tangential velocity is more evident in the region near hub and suction surface, as the mainstream flow shows a higher concentration in the region near shroud and pressure surface.

From Figure 8.22, one can observe that, near the inlet, the positive velocity component $V_n$ indicates a outward flow because of the effects of the

upstream flow. As the flow develops downstream, $V_n$ exhibits an outward flow towards the suction side of the passage, and an inward flow towards the pressure side indicating the presence of secondary flows within the stator passage. These are shown more clearly in Figure 8.24.

### 8.3.3 Comparison between the MPAGE and 3DGE Results

The MPAGE velocities, the passage-averaged velocity components $\bar{V}_p$ and $\bar{V}_t$ around the rotor and stator, are presented in Figure 8.25 and 8.26 with comparison to the 3DGE results within the rotor and stator. The passage-averaged 3DGE velocities presented in these Figures are integrated from the 3DGE solutions across the blade pitch according to the definition of the passage-averaged operator in the Section 2 of Chapter 2. The 3DGE absolute tangential velocity $V_t$ within the rotor is obtained by adding the relative rotating velocity

$$V_t = W_t + \omega R \tag{8.2}$$

where, $R$ is the radial distance measured from the axis, and $\omega$ is the shaft speed of the machines.

The MPAGE results are shown as straight lines and the 3DGE results as dotted lines. Good agreement can be observed, indicating again that the present passage-averaged approach is relatively accurate and can provide

reasonable passage-averaged solutions to a large number of turbomachines, and even to multistage machines.

### 8.3.4 MPAGE Results without Stator

It is interesting to conduct a test for the performance of the stator/diffuser. This can be done by imposing all the external force terms to zero within the stator passage while keeping these terms within rotor passage as they should be. In other words, the presence of the diffuser(stator) is totally neglected. As mentioned before, the function of the stator is to convert the kinetic energy into static pressure. Without the stator, the exit velocity can be expected to be larger than with the stator. Indeed, this is supported by the present numerical prediction in Figure 8.27. It is observed that the velocity component $V_p$ has no significant changes (since the flow must conserve the mass across the blade section), while the velocity component $V_t$ is dramatically decreased with the stator as the flow develops downstream.

From Figure 8.27a, it can also be observed that the viscous blade effects are relatively stronger near the hub region as shown by the straight line (with stator) against the dotted line(without stator). The explanation is that near the hub region, the blade surfaces are much closer because of the annular cross section and small blockage factor B.

# Chapter 9

# Conclusion and Recommendations

The fluid mechanics of turbomachinery is one of the most complex research field of engineering science. Although much progress has been achieved in studying various kind of turbomachines with both numerical and experimental techniques, there are still many flow phenomena in turbomachines that are not well understood. One of the most difficult phenomena is the rotor-stator interaction with one blade row rotating with respect to another.

The problem associated with the rotor-stator interaction of turbomachinery flows has been studied in this research and a mathematical model for the flow simulation has been proposed. This model has been implemented by the passage-averaged through-flow computation without considering explicitly the presence of the blade rows. The effects of the blade rows are accounted for by averaged force terms, which are computed from the three-dimensional solutions within each blade passage. This approach has many advantages with regarding to the available capability of computer resources:

(i) It avoids a full three-dimensional time dependent computation through a whole machine, (ii) It does not require the use of adaptive moving grid to couple the flows in the rotating and stationary frame of references, (iii) The full three-dimensional computations within blade passages can provide more accurate three-dimensional information, incorporated into the external force terms, than blade-to-blade computations, (iv) It can capture the passage-averaged properties and some three-dimensional behaviours of the complex flow in a rotor-stator stage turbomachines.

Two solvers for the passage-averaged through-flow computation and the three-dimensional internal flow computation have been developed. In the present study, the vorticity, scalar and vector potential formulation of the Navier-Stokes equations has been used. These solvers are able to predict the flow through an axisymmetric channel, a straight duct, a curved duct and over a rotating blade passage. It has been shown through numerical test cases that the coupling of these two solvers can provide satisfactory solutions of the flow in a rotor-stator stage turbomachines.

The proposed model has been applied successfully to a mixed-flow pump with a rotor(impeller) and a stator(diffuser) equipped in the National Engineering Laboratory. The predicted solutions were compared with the experimental data. Even considering the absence of a proper turbulent model, the numerical results were reasonable and correctly represent the complex

three-dimensional flow pattern found in the experimental studies.

It is felt that the present model presents a good starting point for the numerical analyse of a rotor-stator interaction flow using passage-averaged approximation. The application of this approach has shown its capability to a multistage turbomachinery configuration. To provide a better understanding of turbomachinery flows, a series of numerical studies is needed. This series of studies should include the following: (i) appropriate turbulence model for turbomachinery flows, (ii) implementation of the effects of the tip-leakage flow.

In the present study, three-dimensional computations were only performed within blade passages. Outside the blade passages, the flow was taken to be axisymmetric and the effects of the wakes were assumed to mix out along the circumferential direction. Extending the three-dimensional blade duct in the upstream and downstream directions of the blade passage may be a good way to capture more three-dimensional effects of the flow, especially the wake effects. And thus improve the coupling.

# References


[1] **Adamczyk,J.J. (1984)**, Model equation for simulating flows in multistage turbomachinery, NASA TM 86869.

[2] **Adamczyk,J.J., Mulac,R.A. and Celestina,M.L. (1986)**, A model for closing the inviscid form of the average-passage equations system, J. Turbomachines, ASME, 108, pp180-186.

[3] **Adamczyk,J.J., Celestina,M.L.,Beach,T.A. and Barnett,M (1990)**, Simulation of three-dimensional viscous flow within a multistage turbine, J. Turbomachines, ASME, 112, pp370-376.

[4] **Aregbesola,Y.A.S. and Burley,D.M. (1977)**, The vector and scalar potential for the numerical solution of two- and three-dimensional Navier-Stokes equations, J. Comp. Phys., 24, pp.389-415.

[5] **Aziz,K. and Hellums,J.D. (1967)**, Numerical solution of the three-dimensional equations of motion for laminar nature convection, Phys. Fluids, 10, pp.314-325.

[6] **Beam,R.M. and Warming,R.F. (1978)**, An implicit factored scheme for the compressible Navier-Stokes equations, **AIAA J., 16**, 393-401.

[7] **Bosman,C. and El Shaarawi,M.A.I. (1977)**, Quasi three-dimensional numerical solution of flow in turbomachines, J. Fluid Eng., ASME, 99, pp.132-140.

[8] **Bosman,C. and Marsh,H. (1974)**, An improved method for calculating the flow in turbomachines including a consistent loss model, J. Mech. Eng. Sci., 16, pp.25-31.

[9] **Briley,W.R. and McDonald,H. (1977)**, Solution of the multidimensional compressible Navier-Stokes equations by a generalized implicit method, J. Comp. Phys., 24, 372-379.

[10] **Camarero,R., Caille,J. and McNabb,J. (1985)**, Numerical simulation of axisymmetric swirling flows with application to turbine diffusers, EPM RT 85-5, École Polytechnique de Montréal.

[11] **Carey,C., Fraser,S.M., Rachman,D. and Wilson,G. (1985a)**, Studies of the flow of air in a model mixed-flow pump using laser doppler anemometry, Part 1: Research facility and instrumentation, NEL Report 698.

[12] **Carey,C., Fraser,S.M., Rachman,D. and Wilson,G. (1985b)**, Studies of the flow of air in a model mixed-flow pump using laser doppler anemometry, Part 2: Velocity measurements within the impeller, NEL Report 699.

[13] **Celestina,M.L., Mulac,R.A. and Adamczyk,J.J. (1986)**, A numerical simulation of the inviscid flow through a counterrotating propeller, J. Turbomachines, ASME, 108, pp.187-193.

[14] **Chang,J.L.C. and Kwak,D. (1984)**, On the method of pseudo compressibility for numerical solving incompressible flows, AIAA Paper, 84-0252.

[15] **Chapman,D.R. (1979)**, Computational aerodynamics development and outlook, AIAA J., 17, pp.1293-1313.

[16] **Cheng,K.C., Lin,R.C. and Ou J.W. (1976)**, Fully developed laminar flow in curved rectangular channels, J. Fluids Eng., ASME, 98, pp.41-48.

[17] **Chorin,A.J. (1967)**, A numerical method for solving incompressible viscous flow problems, J. Comp. Phys., 2, pp.12-26.

[18] **Davis,R.L., Carter,J.E. and Hafez,M. (1989)**, Three-dimensional viscous flow solutions with a vorticity-stream function formulation, AIAA J., 27, pp.892-900.

[19] **Dennis,S.C.R., Ingham,D.B. and Cook,R.N. (1979)**, Finite-difference method for calculating steady incompressible flows in three-dimensions, J. Comp. Phys., 33, pp.325-339.

[20] **Dorr,F.W. (1969)**, Remarks on the iterative solution of the Neumann problem on a rectangle by successive line overrelaxation. Math. Comp., 23, pp.177-179.

[21] **Dorr,F.W. (1970)**, The direct solution of the discrete Poisson equation on a rectangle, SIAM Review, 12, pp.248-263.

[22] **El-Refaee,M.M.,Wu,J.C. and Lekoudis,S.G. (1981)**, Solutions of the compressible Navier-Stokes equations using the integral method, AIAA J., 20, pp.356-362.

[23] **Farok,B. and Fusegi,T., (1985)**, A coupled solution of the vorticity-velocity formulation of the incompressible Navier-Stokes equations, Int. J. Numer. Meth. Fluids, 5, pp.1017-1034.

[24] **Fasel,H. (1976)**, Investigation of the stability of boundary layers by a finite-difference model of the Navier-Stokes equations, J. Fluid Mech., 78, pp.355-383.

[25] **Frankel S.P. (1950)**, Convergence rates of Iterative treatments of partial differential equations, Math. Tables and other Aids to Computation, 4, pp.65-75.

[26] **Garon,A. (1987)**, Modèle pour l'étude des écoulement visqueux et incompressibles dans les turbines hydrauliques", Ph.D thèse, École Polytechnique de Montréal.

[27] **Garon,A., Pelletier,D. and Camarero,R. (1989)**, Passage-averaged Navier-Stokes equations with finite element application, AIAA Paper, 89-0208.

[28] **Gary,J. (1967)**, On convergence rates for line overrelaxation, Math. Comp., 21, pp.220-223.

[29] **Gatsti,T.B., Grosch,C.E. and Rose,M.E. (1982)**, A numerical study of the two-dimensional Navier-Stokes equations in vorticity-velocity variables, J. Comp. Phys., 48, pp.1-22.

[30] **Gerard,G.S. (1989)**, A Dual potential formulation of the Navier-Stokes equations, Ph.D Thesis, Iowa State University.

[31] **Ghia,K.N. and Sokhey,J.S. (1977)**, Laminar incompressible viscous flow in curved ducts of regular cross-sections, J. Fluids Eng., 99, pp.640-648.

[32] **Goldstein,R.J. and Kreid,D.K. (1967)**, Measurement of laminar flow development in a square duct using a laser-doppler flowmeter, J. Appl. Mech., ASME, 34, pp.813-818.

[33] **Gresho,P.M. (1987)**, On pressure boundary conditions for the incompressible Navier-Stokes Equations, Int. J. Numer. Meth. Fluids, 7, pp.1111-1145.

[34] **Guevremont,G., Habashi,W.G. and Hafez,M.M. (1990)**, Finite-element solution of the Navier-Stokes equations by a velocity-vorticity method, Int. J. Numer. Meth. Fluids, 10, pp.461-475.

[35] **Guj,G. and Stella,F. (1988)**, Numerical solutions of high-Re recirculating flows in vorticity-velocity form, Int. J. Numer. Meth. Fluids, 8, pp.405-416.

[36] **Habashi,W.G., Peeters,M.F., Guevremont,G. and Hafez,M.M. (1987)**, Finite-element solutions of the compressible Navier-Stokes equations, AIAA J., 25, pp.944-948.

[37] **Han,L.S. (1960)**, Hydrodynamic entrance lengths for incompressible laminar flow in rectangular ducts, J. Appl. Mech., ASME, 27, pp.403-409.

[38] **Harlow,F.H. and Welch,J.E. (1965)**, Numerical calculation of time-dependent viscous incompressible flow with free surface, Phys. of Fluids, 8, pp.2182-2189.

[39] **Hirasaki,G.J. and Hellums,J.D. (1968)**, A general formulation of the boundary conditions on the vector potential in three-dimensional hydrodynamics, Quart. Appl. Math., 26, pp.331-342.

[40] **Hirasaki,G.J. and Hellums,J.D. (1970)**, Boundary conditions on the vector and scalar potentials in viscous three-dimensional hydrodynamics, Quart. Appl. Math., 28, pp.293-296.

[41] **Hirsch,Ch. and Deconinck,H. (1985a)**, Description of viscous flow models from Navier-Stokes to potential flow models, Thermodynamics and Fluid Mechanics of Turbomachinery, 1, pp.3-35.

[42] **Hirsch,Ch. and Deconinck,H. (1985b)** Through flow models in turbomachines: Stream surface and passage average equation representation, Thermodynamics and Fluid Mechanics of Turbomachinery, 1, pp.73-129.

[43] **Jennions,I.K. and Stow,P. (1985a)**, A Quasi-three-dimensional turbomachinery blade design system: Part I - Throughflow analysis, J. Eng. Gas Turbines and power, ASME, 107, pp.301-307.

[44] **Jennions,I.K. and Stow,P. (1985b)**, A Quasi-three-dimensional turbomachinery blade design system: Part II - Computerized system, J. Gas Turbines and power, ASME, 107, pp.308-316.

[45] **Krimerman,Y. and Adler,D. (1978)**, The complete three-dimensional calculation of the compressible flow field in turbo impellers, J. Mech. Eng. Sci., 20, pp.149-158. 24, pp.389-415.

[46] **Kwak,D., Chang,J.L.C., Shanks,S.P. and Chakravarthy,S. (1984)**, An incompressible Navier-Stokes flow solver in three-dimensional curvilinear coordinate system using primitive variables, AIAA Paper, 84-0253.

[47] **Langhaar,H.L. (1942)**, Steady flow in the transition length of a straight tube, J. Appl. Mech., ASME, 64, pp.A55-A58.

[48] **McNally,W.D. and Sockol,P.M. (1985)**, Review-computational methods for internal flow with emphasis on turbomachines, J. Fluid Eng., ASME, 107, pp.6-22.

[49] **Mori,Y., Uchida,Y. and Ukon,T. (1971)**, Forced convection heat transfer in a curved channel with a square cross section, Int. J. Heat Mass Transfer, 14, pp.1787-1805.

[50] **Morino,L. (1985)**, Scalar/vector potential formulation for compressible viscous unsteady flows, NASA CR 3921.

[51] **Obayashi,S. and Kuwahara,K. (1986)**, LU factorization of an implicit scheme for the compressible Navier-Stokes equations, J. Comp. Phys., 63, pp.157-167.

[52] **Ozoe,H., Yamamoto,K., Churchill,S.W. and Sayama,H. (1976)**, Three-dimensional numerical analysis of laminar nature convection in a confined fluid heated from below, J. Heat Transfer, ASME, 98, pp.2

[53] **Ozoe,H., Mouri,A., Ohmuro,M., Churchill,S.W. and Lior,N. (1985)**, Numerical calculations of laminar and turbulent nature convection in water in rectangular channels heated and cooled isothermally on the opposing vertical walls, Int. J. Heat Mass Transfer, 28, pp.125-13

[54] **Page M., Garon A. and Camarero R. (1989)**, LUSS: Sous-programmes pour la résolution d'un systeme d'équations algébriques stockées en ligne de ciel, EPM RT-89-13.

[55] **Patankar,S.V. (1980)**, Numerical heat transfer and fluid flow, Hemisphere Publishing Corporation.

[56] **Pouagare,M.C. (1984)**, Numerical and experimental investigation of turbomachinery rotor flow fields, Ph.D. Thesis, The Pennsylvania state university.

[57] **Pulliam,T.H. and Steger,J.L. (1980)**, Implicit finite-difference simulations of three-dimensional compressible flow, AIAA J., 18, pp.159-167.

[58] **Rao,k.V., Steger,J.L. and Pletcher,R.H. (1989)**, Three-dimensional dual potential procedure for inlets and indraft wind tunnels, AIAA J., 27, pp.876-884.

[59] **Richardson,S.M. and Cornish,A.R.H. (1977)**, Solution of three-dimensional incompressible flow problems, J. Fluid Mech., 82, pp.309-319.

[60] **Roache,P.J. (1982)**, Computational fluid dynamics, Hermosa Publishers.

[61] **Shang,J.S., Buning,P.G., Hankey,W.L. and Wirth,M.C. (1980)**, Performance of a vectorized three-dimensional Navier-Stokes code on the Cray-1 computer, AIAA J., 18, pp.1073-1079.

[62] **Shehperd,D.G. (1956)**, Principles of Turbomachinery, The Macmillan Company.

[63] **Sieverding,C.H. (1985)**, Recent progress in the understanding of basic aspects of secondary flows in turbine blade passages, J. Eng. Gas Turbines and Power, ASME, 107, pp.248-257.

[64] **Sparrow,E.M., Hixon,C.W. and Shavit,G. (1967)**, Experiments on laminar flow development in rectangular ducts, J. Basic Eng., ASME, 89, pp.116-124.

[65] **Speziale,C.G. (1987)**, On the advantages of the vorticity-velocity formulation of the equations of fluid dynamics, J. Comp. Phys., 73, pp.476-480.

[66] **Steger,J.L. and Kutler,P. (1977)**, Implicit finite-difference procedures for the computation of vortex wakes, AIAA J., 15, pp.581-590.

[67] **Stow,P. (1985)**, Modeling of viscous flows in turbomachinery, Thermodynamics and Fluid Mechanics of Turbomachinery, 1, pp.37-71.

[68] **Wang,Q.H., Zhu,G.X. and Wu,C.H. (1985)**, Quasi-three-dimensional and full three-dimensional rotational flow calculations in turbomachines, J. Eng. Gas Turbines and Power, ASME, 107, pp.277-285.

[69] **Wong,A.k. and Reize,J.A. (1984)**, An effective vorticity-vector potential formulation for the numerical solutions of three-dimensional duct flow problems, J. Comp. Phys., 55, pp.98-114.

[70] **Wong,A.k. and Reize,J.A. (1986)**, The vector potential in the numerical solutions of three-dimensional fluid dynamics problems in multiple connected regions, J. Comp. Phys., 62, pp.124-142.

[71] **Wu,C.H. (1952)**, A general theory of three-dimensional flow in subsonic and supersonic turbomachines of axial, radial and mixed-flow types, NACA TN 2604.

[72] **Yang H.R. (1988)**, Three-dimensional calculation of the internal flow using vorticity-potential method, Ph.D. Thesis, École Polytechnique de Montréal.

[73] **Yang H.R. and Camarero R. (1986)**, An improved vorticity-potential method for three-dimensional duct flow simulations, Int. J. Numer. Meth. Fluids, 6, pp.35-45.

[74] **Yang H.R. and Camarero R. (1991)**, Internal three-dimensional viscous flow solutions using the vorticity-potential method, Int. J. Numer. Meth. Fluids, 12, pp.1-15.

[75] **Young D. (1954)**, Iterative methods for solving partial differential equations of elliptic type, Transaction of AMS, 76, pp.92-111.

# APPENDIX A

## Relations between rotating and stationary frame of references

The relationship for the primitive variables between rotating and stationary frame of references are simple. But for non-primitive variables, like the scalar and vector potentials, these relationships are not straightforward.

If, for instance, we consider a duct rotating with respect to an axis with shaft speed $\Omega$, and assume the following relationships are holding

$$\begin{aligned} \mathbf{V} &= \mathbf{U} + \mathbf{V}_\Omega \\ \mathbf{W} &= \mathbf{W}_R + \mathbf{W}_\Omega \\ \phi &= \phi_R + \phi_\Omega \\ \mathbf{A} &= \mathbf{A}_R + \mathbf{A}_\Omega \end{aligned} \tag{9.1}$$

where, subscript $R$ represents the relative variables in the rotating frame of reference, and subscript $\Omega$ represents the variables generated by the shaft speed or the difference of the absolute and relative variables. The problem is to determine the variables with subscripts $\Omega$.

It is easy to show that, in an axisymmetric coordinate system, the velocity and vorticity have the following expressions

$$\begin{aligned} \mathbf{V}_\Omega &= (0,\ \omega r,\ 0) \\ \mathbf{W}_\Omega &= (0,\ 0,\ 2\omega) \end{aligned} \tag{9.2}$$

Since the velocity produced by the scalar potential is the irrotational part of the velocity field, while the velocity $\mathbf{V}_\Omega$ is generated by the rotation with vorticity $\mathbf{W}_\Omega$. The following relation can be imposed

$$\phi_\Omega = 0 \tag{9.3}$$

or

$$\phi_\Omega = \phi \tag{9.4}$$

Therefore, for vector potential, we have

$$\begin{aligned} \mathbf{V}_\Omega &= \mathbf{V} - \mathbf{U} \\ &= \nabla \times (\mathbf{A} - \mathbf{A}_\mathbf{R}) \\ &= \nabla \times \mathbf{A}_\Omega \end{aligned} \tag{9.5}$$

Note that

$$\mathbf{W}_\Omega = \nabla \times \mathbf{V}_\Omega \tag{9.6}$$

and

$$\begin{aligned} \mathbf{W}_\Omega &= \nabla \times (\nabla \times \mathbf{A}_\Omega) \\ &= \nabla(\nabla \cdot \mathbf{A}_\Omega) - \nabla^2 \mathbf{A}_\Omega \\ &= -\nabla^2 \mathbf{A}_\Omega \end{aligned} \tag{9.7}$$

here, we used $\nabla \cdot \mathbf{A}_\Omega = 0$, since both $\mathbf{A}$ and $\mathbf{A}_R$ are assumed to be solenoidal (or divergence free).

Now the linear equation for $\mathbf{A}_\Omega$

$$\nabla^2 \mathbf{A}_\Omega = -\mathbf{W}_\Omega \tag{9.8}$$

can be easily solved since the velocity $\mathbf{V}_\Omega$ and vorticity $\mathbf{W}_\Omega$ are known everywhere.

# APPENDIX B

## Local orthogonal coordinate curvilinear system

It will be convenient to use a local orthogonal coordinate curvilinear system ($\xi_{t_1}$, $\xi_{t_2}$, $\xi_n$) on general boundary surfaces instead of the Cartesian coordinate system ($x$, $y$, $z$) as illustrated in Figure B.1.

Let

$$\vec{\mathbf{r}} = \vec{\mathbf{r}}(\xi_{t_1}, \xi_{t_2}, \xi_n) \tag{9.9}$$

be the position vector of a point on S and let introduces the scalar factors

$$\begin{aligned}
h_{t_1} &= \|\frac{\partial \mathbf{r}}{\partial \xi_{t_1}}\| \\
&= [(\frac{\partial x}{\partial \xi_{t_1}}) + (\frac{\partial y}{\partial \xi_{t_1}}) + (\frac{\partial x}{\partial \xi_{t_1}})]^{1/2} \\
h_{t_2} &= \|\frac{\partial \mathbf{r}}{\partial \xi_{t_2}}\| \\
&= [(\frac{\partial x}{\partial \xi_{t_2}}) + (\frac{\partial y}{\partial \xi_{t_2}}) + (\frac{\partial x}{\partial \xi_{t_2}})]^{1/2} \\
h_n &= \|\frac{\partial \mathbf{r}}{\partial \xi_n}\| \\
&= [(\frac{\partial x}{\partial \xi_n}) + (\frac{\partial y}{\partial \xi_n}) + (\frac{\partial x}{\partial \xi_n})]^{1/2}
\end{aligned} \tag{9.10}$$

One can show that the expressions for gradient, divergence and cross product in terms of the orthogonal curvilinear coordinates take the following form

$$\nabla\phi = \frac{1}{h_{t_1}}\frac{\partial \phi}{\partial \xi_{t_1}}\vec{\mathbf{t}}_1 + \frac{1}{h_{t_2}}\frac{\partial \phi}{\partial \xi_{t_2}}\vec{\mathbf{t}}_2 + \frac{1}{h_n}\frac{\partial \phi}{\partial \xi_n}\vec{\mathbf{n}} \tag{9.11}$$

$$\begin{aligned}
\nabla \cdot \mathbf{V} &= \frac{1}{h_{t_1} h_{t_2} h_n}\Big[\frac{\partial}{\partial \xi_{t_1}}(h_{t_2} h_n v_{t_1}) \\
&\quad + \frac{\partial}{\partial \xi_{t_2}}(h_{t_1} h_n v_{t_2}) + \frac{\partial}{\partial \xi_n}(h_{t_1} h_{t_2} v_n)\Big] \qquad (9.12) \\
\nabla \times \mathbf{V} &= \frac{1}{h_{t_2} h_n}\Big[\frac{\partial}{\partial \xi_{t_2}}(h_n v_n) - \frac{\partial}{\partial \xi_n}(h_{t_2} v_{t_2})\Big]\vec{\mathbf{t}}_1 \\
&+ \frac{1}{h_{t_1} h_n}\Big[\frac{\partial}{\partial \xi_n}(h_{t_1} v_{t_1}) - \frac{\partial}{\partial \xi_{t_1}}(h_n v_n)\Big]\vec{\mathbf{t}}_2 \\
&+ \frac{1}{h_{t_1} h_{t_2}}\Big[\frac{\partial}{\partial \xi_{t_1}}(h_{t_2} v_{t_2}) - \frac{\partial}{\partial \xi_{t_2}}(h_{t_1} v_{t_1})\Big]\vec{\mathbf{n}} \qquad (9.13)
\end{aligned}$$

and

$$\begin{aligned}
\nabla_S \times \mathbf{V} &= \frac{1}{h_{t_2} h_n}\Big[\frac{\partial}{\partial \xi_{t_2}}(h_n v_n)\Big]\vec{\mathbf{t}}_1 \\
&+ \frac{1}{h_{t_1} h_n}\Big[-\frac{\partial}{\partial \xi_{t_1}}(h_n v_n)\Big]\vec{\mathbf{t}}_2 \\
&+ \frac{1}{h_{t_1} h_{t_2}}\Big[\frac{\partial}{\partial \xi_{t_1}}(h_{t_2} v_{t_2}) - \frac{\partial}{\partial \xi_{t_2}}(h_{t_1} v_{t_1})\Big]\vec{\mathbf{n}} \qquad (9.14)
\end{aligned}$$

Where, $\vec{\mathbf{t}}_1$, $\vec{\mathbf{t}}_2$ and $\vec{\mathbf{n}}$ are the unit vectors tangential to the directions $\xi_{t_1}$, $\xi_{t_2}$ and $\xi_n$ respectively, and $\nabla_S$ is the surface gradient operator.

# APPENDIX C

## Passage-averaged analytical solution for straight duct

From the paper of Han (1960), one can express the axial velocity to a rectangular duct (see Figure 7.1) as follows

$$u_z = \frac{\pi^2}{4} C^{-1} \sum_{m,n=1}^{\infty} \frac{(-1)^{m+n} \cos[(2m-1)\pi x/2a] \cos[(2n-1)\pi y/2b]}{(2m-1)(2n-1)[(2m-1)^2\gamma^2 + (2n-1)^2 + (2\beta b/\pi)^2]} \tag{9.15}$$

where

$$C = \sum_{m,n=1}^{\infty} 1/(2m-1)^2(2n-1)^2[(2m-1)^2\gamma^2 + (2n-1)^2 + (2\beta b/\pi)^2] \tag{9.16}$$

The parameter $\beta$ and its relations with axial distance can be found in Han (1960).

Employing the passage-averaging procedure described in section 3.2, the velocity in (9.15) is averaged across the y-direction and gives

$$\overline{u}_z = \frac{\pi}{2} C^{-1} \sum_{m=1}^{\infty} \frac{(-1)^{m+1}}{2m-1} D_m \cos[(2m-1)\pi x/2b] \tag{9.17}$$

and

$$D_m = \sum_{n=1}^{\infty} 1/(2n-1)^2[(2m-1)^2\gamma^2 + (2n-1)^2 + 2\beta b/\pi)^2] \tag{9.18}$$

The derivatives of the velocity with respect to the $y$-direction on the two parallel plates (i.e. $y = \pm b$) have the following form

$$\left(\frac{\partial u_z}{\partial y}\right)_b = \frac{\pi^3}{8b} C^{-1} \sum_{m=1}^{\infty} E_m \cos[(2m-1)\pi x/2a] \tag{9.19}$$

$$\left(\frac{\partial u_z}{\partial y}\right)_{-b} = -\left(\frac{\partial u_z}{\partial y}\right)_{b} \tag{9.20}$$

Then the $z$-component of the difference of the shear forces on the two plates is

$$\begin{aligned} f_z &= \frac{1}{2b}[(\frac{\partial u_z}{\partial y})_b - (\frac{\partial u_z}{\partial y})_{-b}] \\ &= \frac{\pi^3}{8b^2} C^{-1} \sum_{m=1}^{\infty} \frac{(-1)^m}{2m-1} E_m \cdot \cos[(2m-1)\pi x/2a] \end{aligned} \tag{9.21}$$

and

$$E_m = \sum_{n=1}^{\infty} 1/[(2m-1)^2\gamma^2 + (2n-1)^2 + (2\beta b/\pi)^2] \tag{9.22}$$

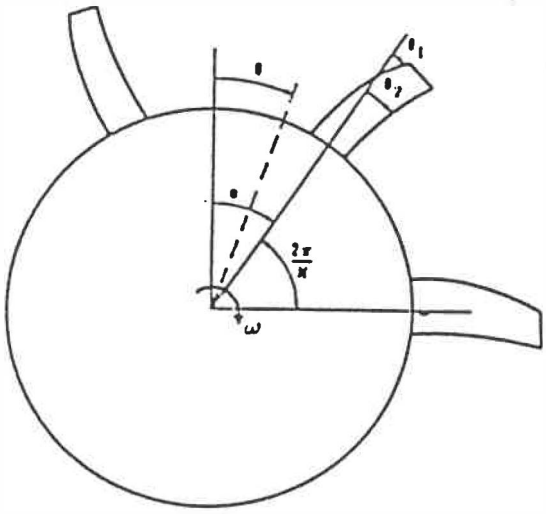
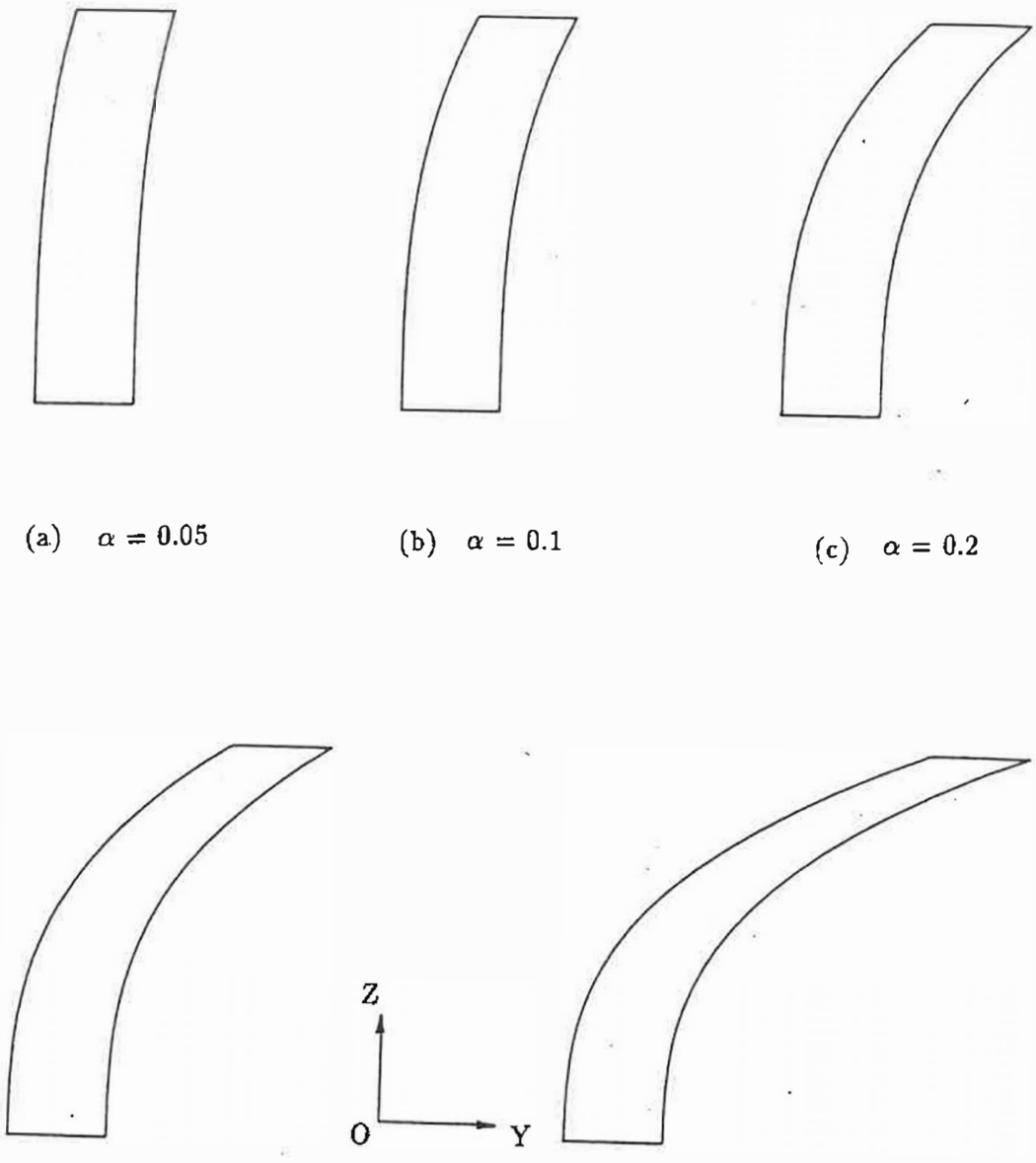


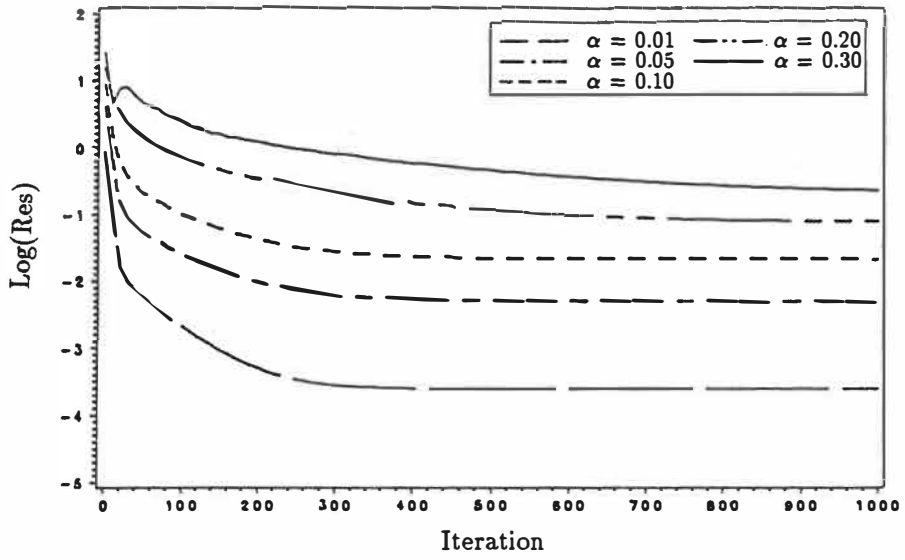

Figure 3.1: Configuration of a Blade Row
(From Adamczyk 1984)



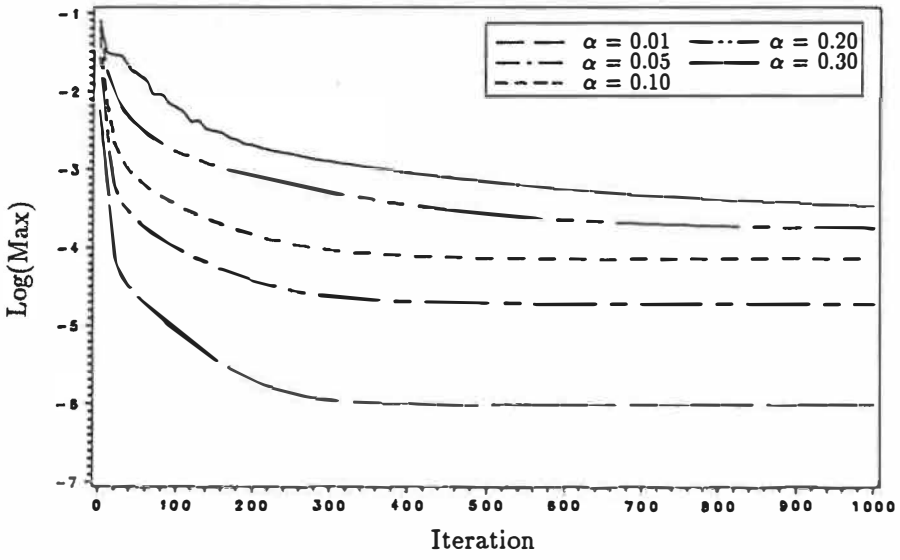

(a) $\alpha = 0.05$ (b) $\alpha = 0.1$ (c) $\alpha = 0.2$

(d) $\alpha = 0.3$ (e) $\alpha = 0.5$

Figure 6.1: Sectional View of Domains with Skewness, $\alpha$




(a) Res = Residue




(b) Max = $\|\phi^{n+1} - \phi^n\|$

Figure 6.2: History of Convergence for Scalar Potential Test

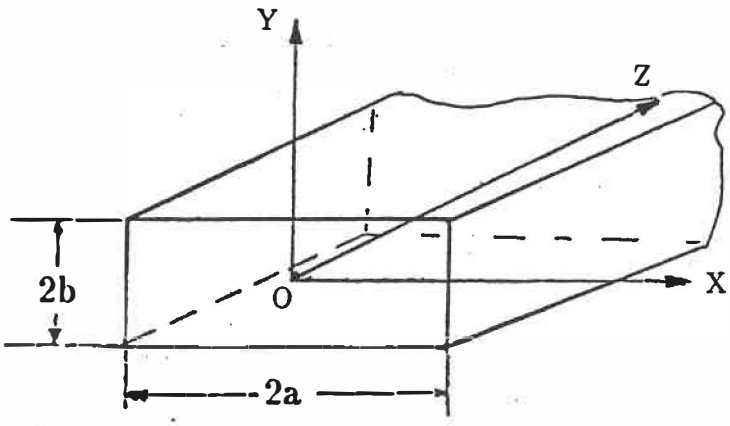
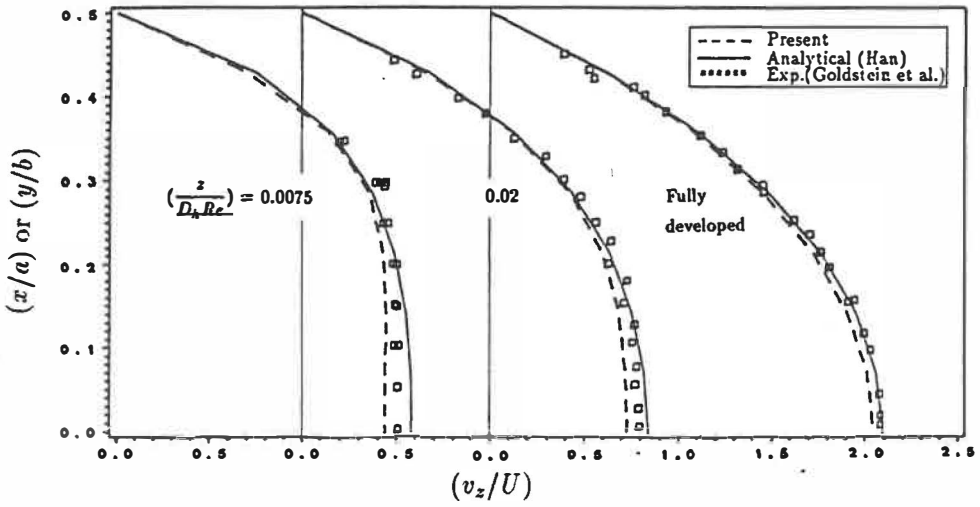
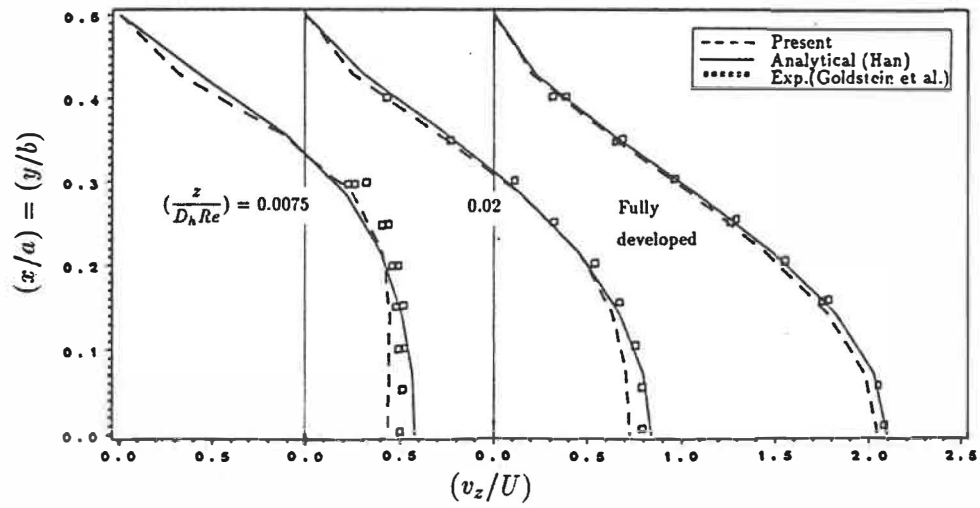



Figure 7.1: Duct Configuration




(a) Central plane




(b) Diagonal plane

Figure 7.2: Velocity Development for a Straight Duct with Aspect Ratio $\gamma = 1.0$

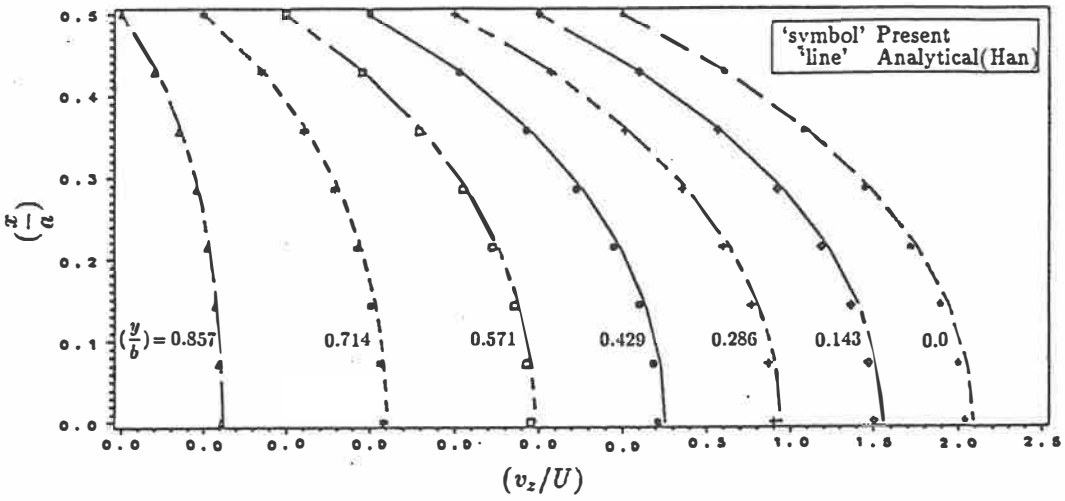



Figure 7.3: Fully-Developed Velocity Profiles, $\gamma = 1.0$

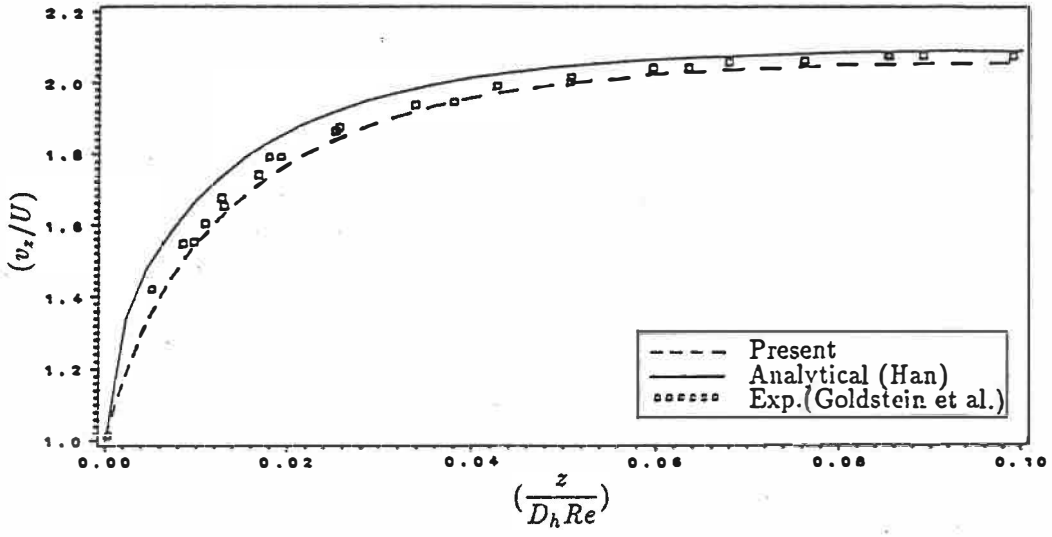
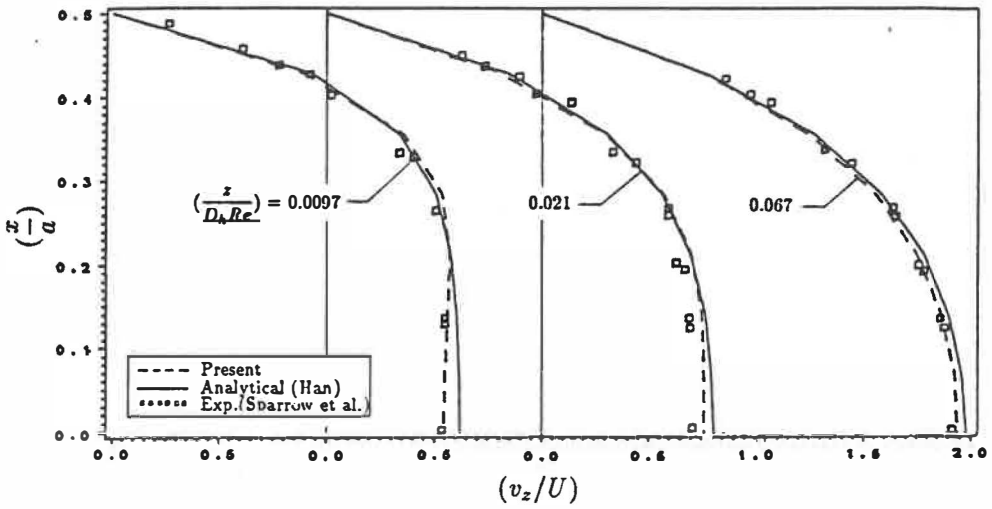
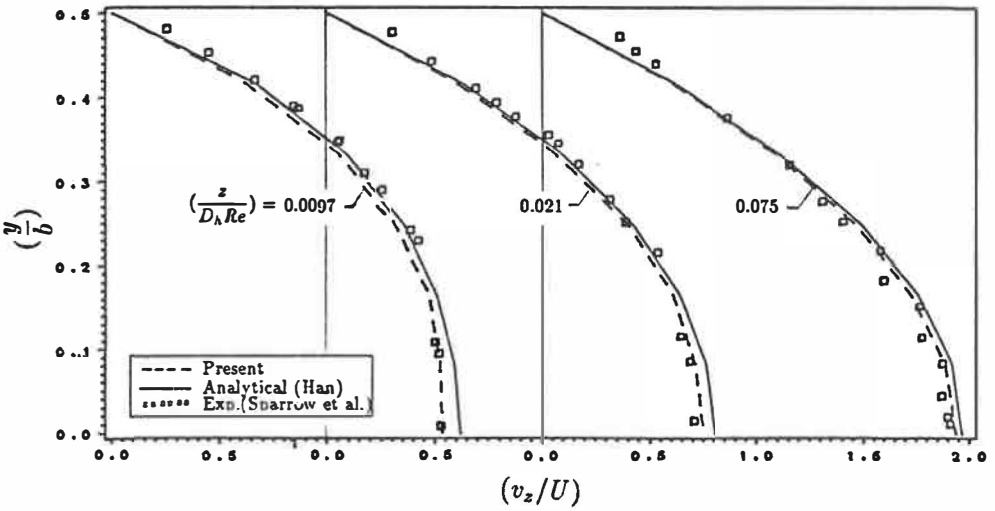



Figure 7.4: Center-Line Velocity Development, $\gamma = 1.0$

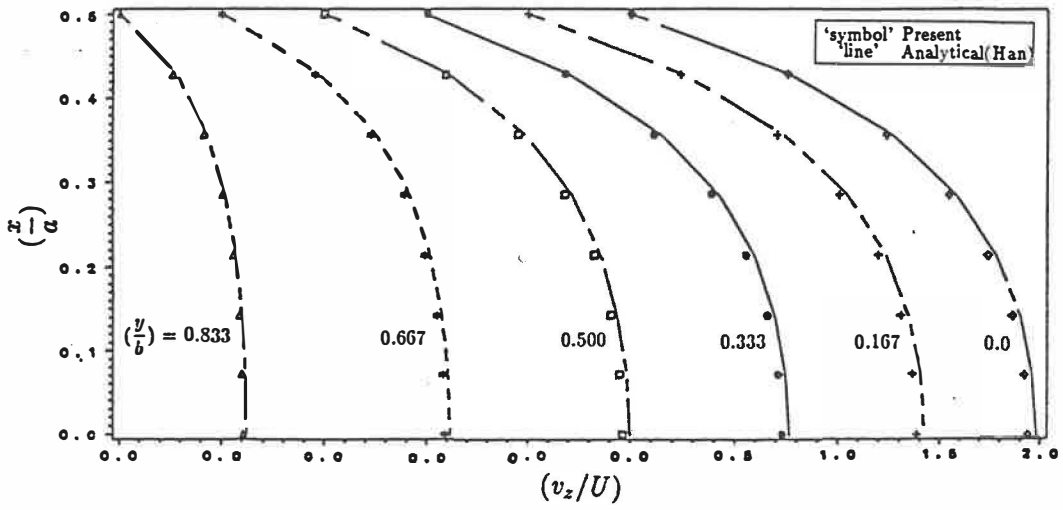



(a) Width section

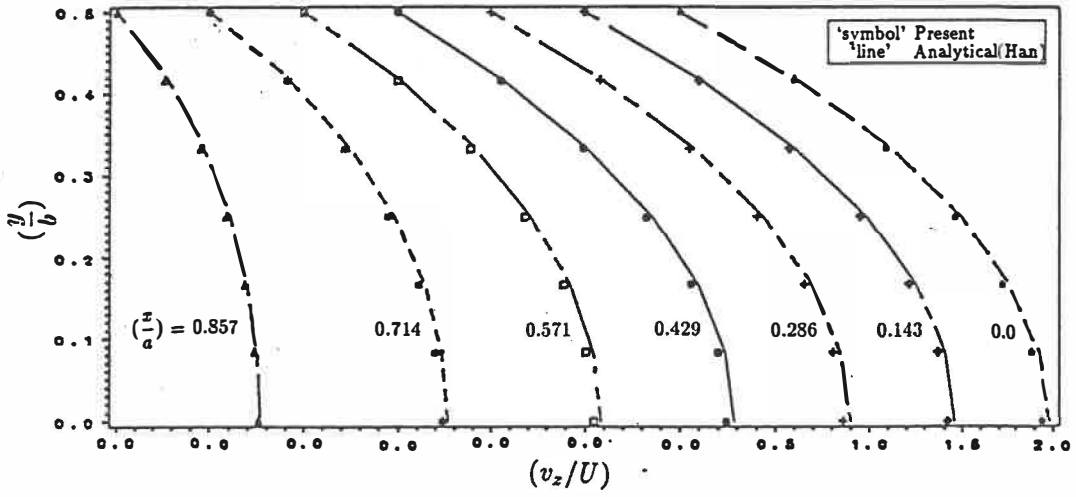



(b) Height section

Figure 7.5: Velocity Development for a Straight Duct with Aspect Ratio $\gamma = 0.5$




(a) Width section




(b) Height section

Figure 7.6: Fully Developed Velocity Profiles, $\gamma = 0.5$

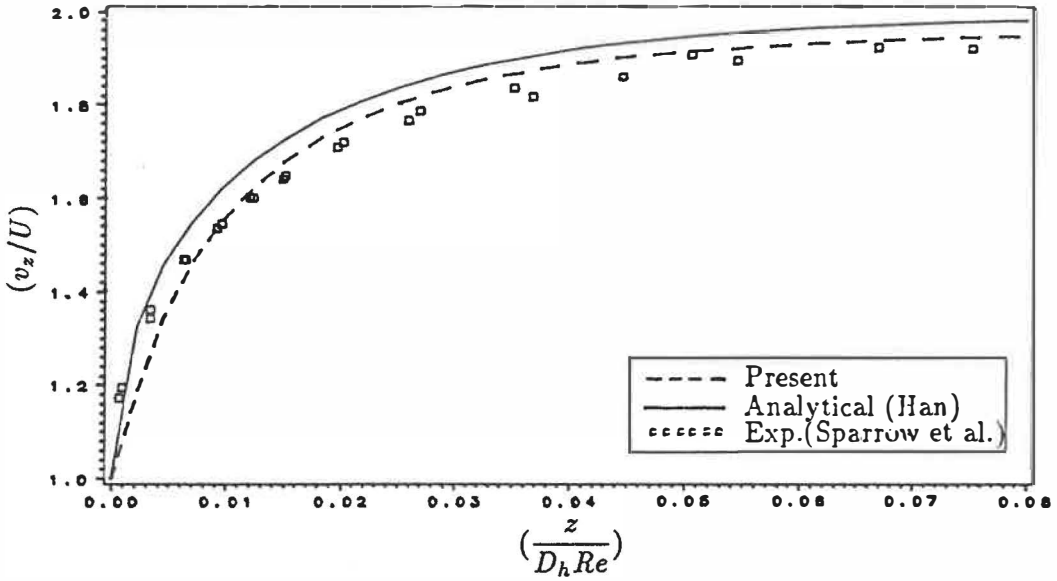



Figure 7.7: Center-Line Velocity Development, $\gamma = 0.5$

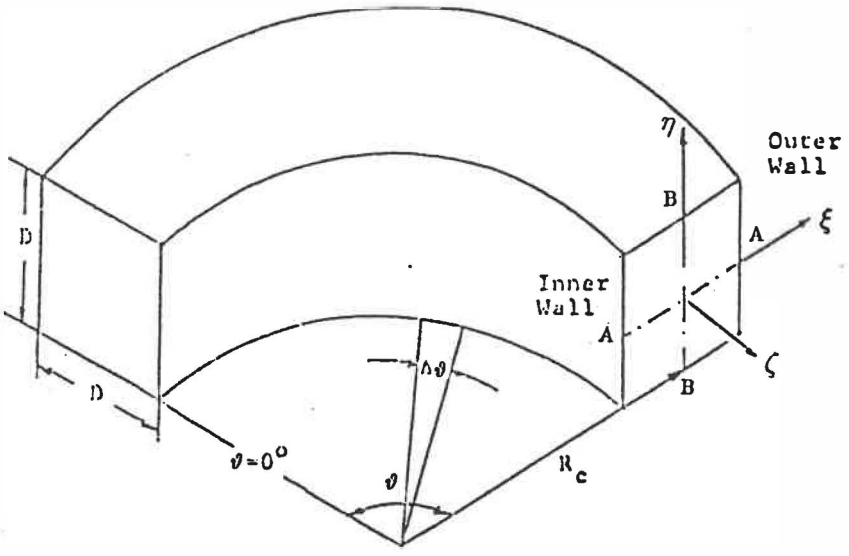
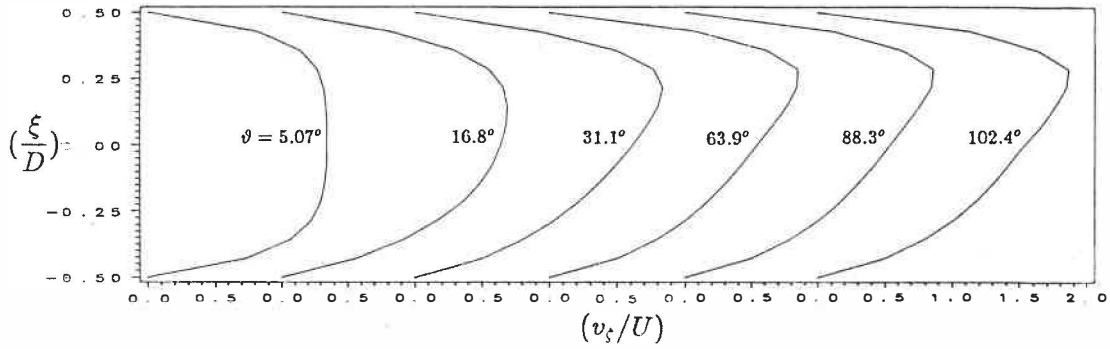
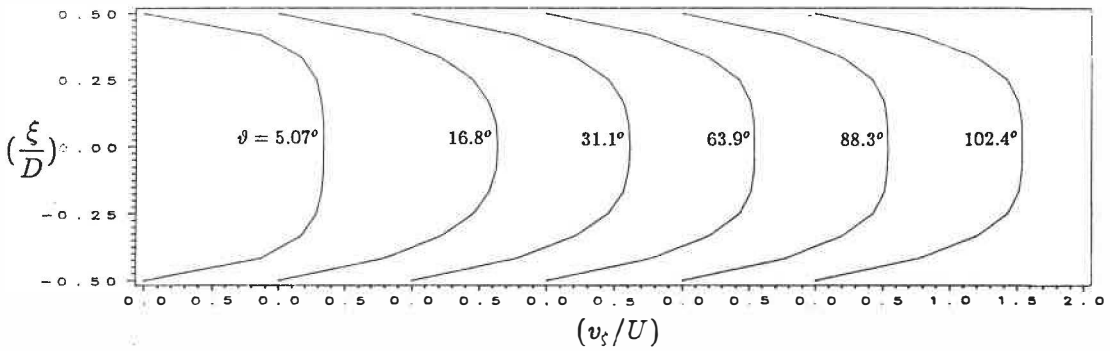



Figure 7.8: Square Curved Duct

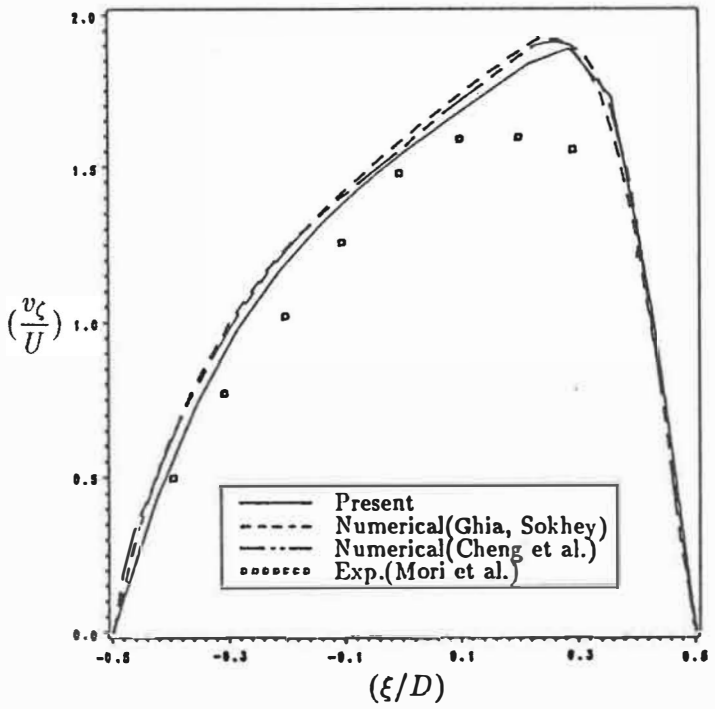



(a) Profile along A-A

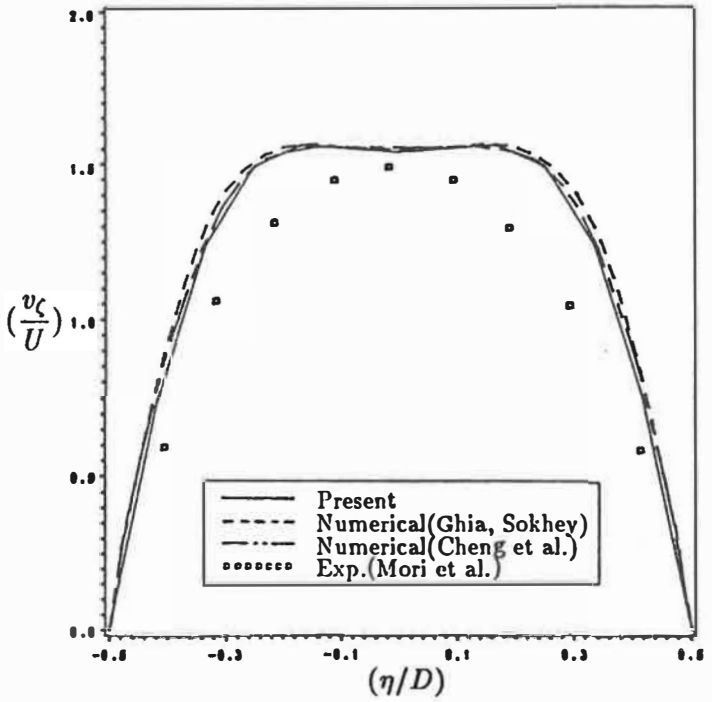



(b) Profile along B-B

Figure 7.9: Streamwise Velocity Development

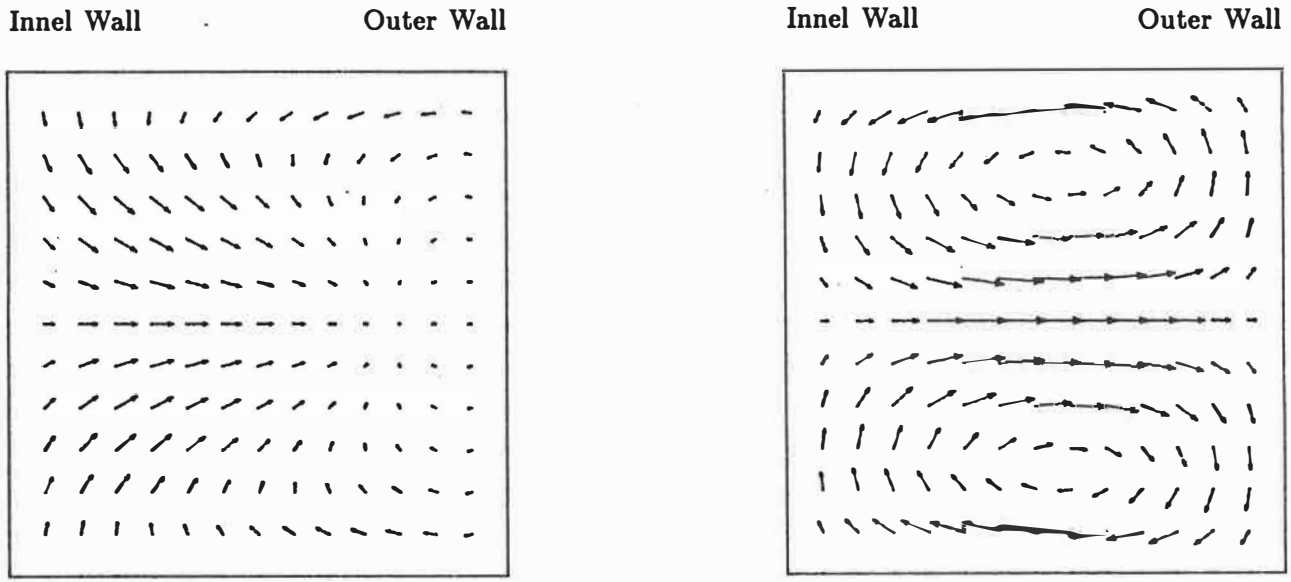



(a) Profile along A-A



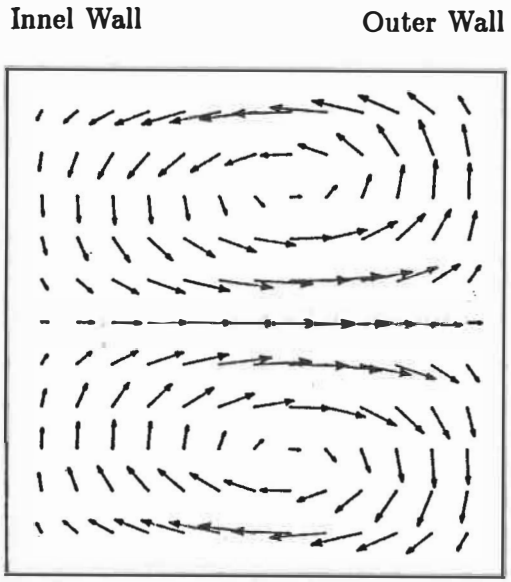

(b) Profile along B-B

Figure 7.10: Fully Developed Velocity, $\vartheta = 102.4^0$

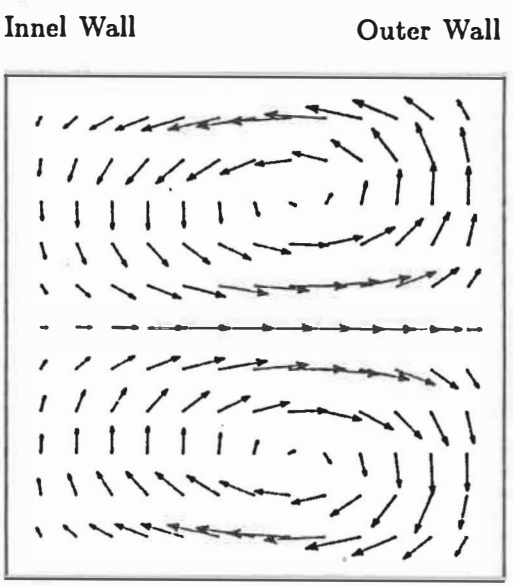



(a) $\vartheta = 5.07^o$ (b) $\vartheta = 16.8^o$

Figure 7.11: Secondary Velocity Vectors

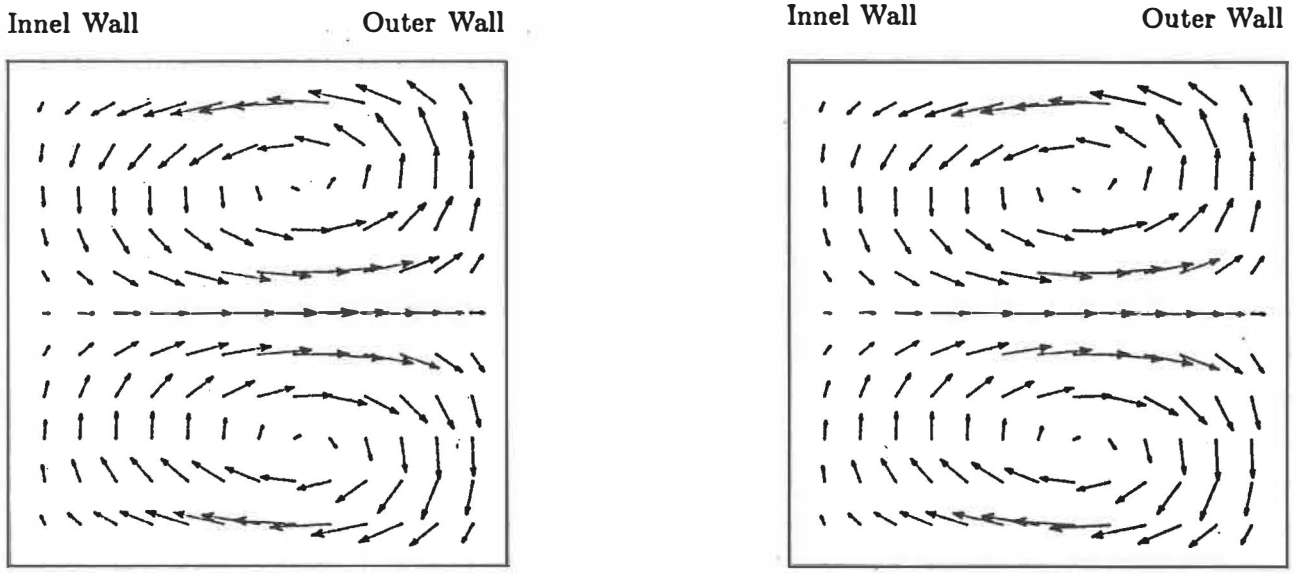



(c) $\vartheta = 31.1^o$



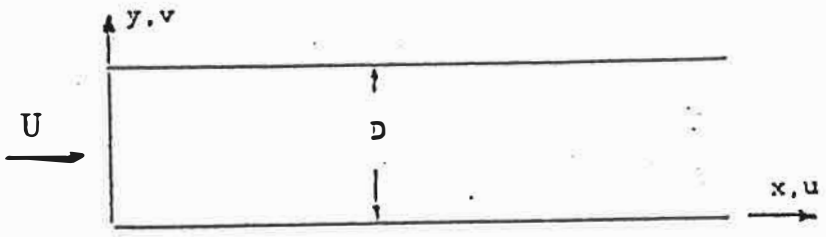

(d) $\vartheta = 63.9^o$

Figure 7.11: Secondary Velocity Vectors




$(e)\ \vartheta = 88.3^o$ $(f)\ \vartheta = 102.4^o$

**Figure 7.11: Secondary Velocity Vectors**



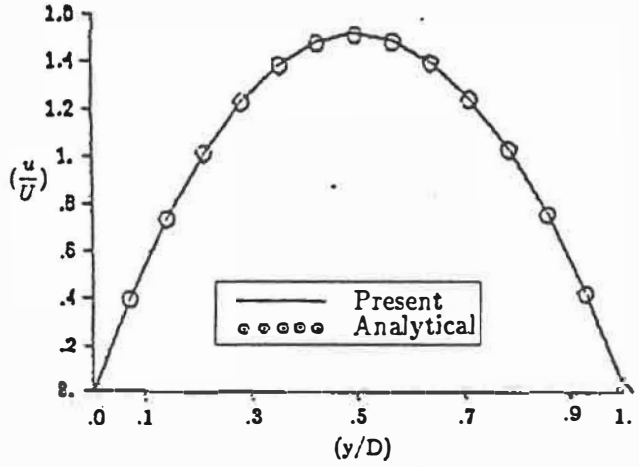
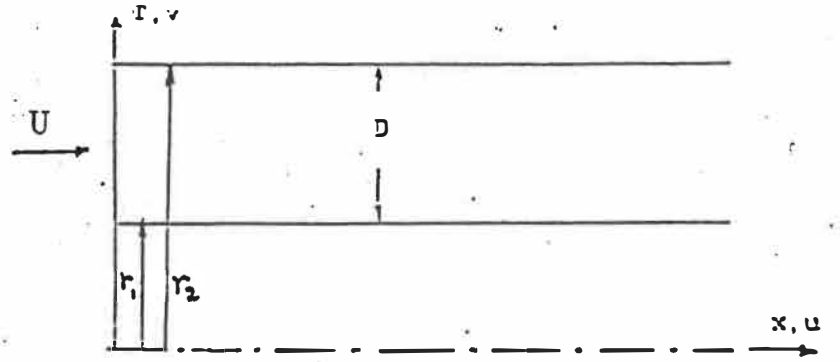




Figure 7.12: Fully Developed Flow Through a Two-Dimensional Channel



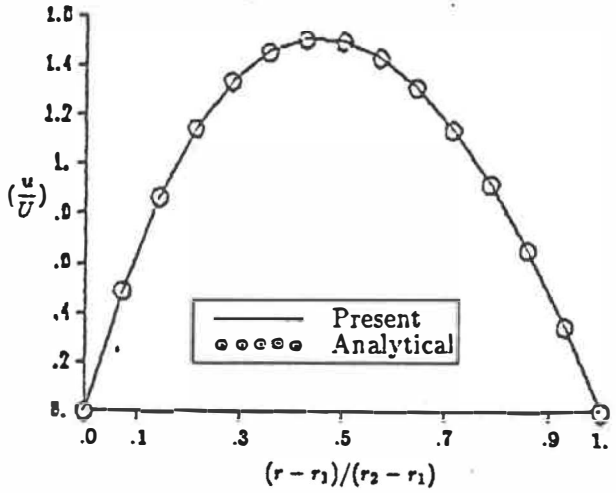
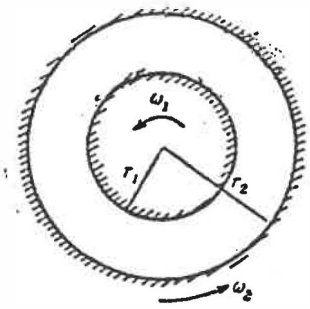
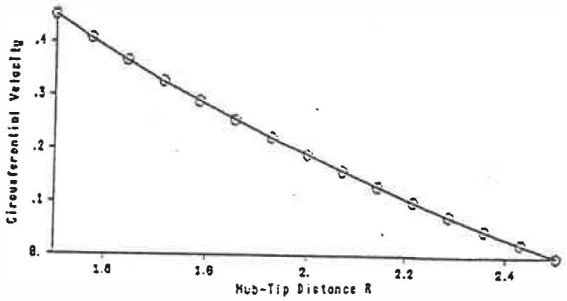




Figure 7.13: Fully Developed Axisymmetric Flow

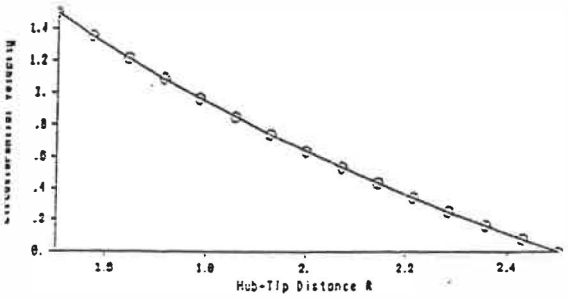



(a) Annulus configuration

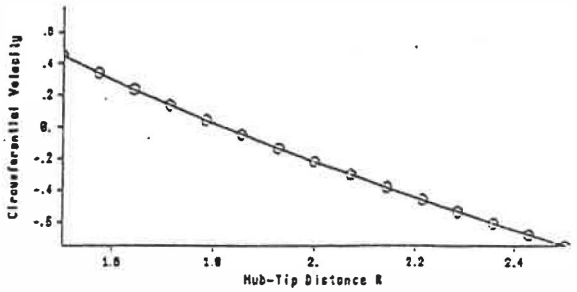



(b) $\omega_1 = 0.5, \omega_2 = 0.0$



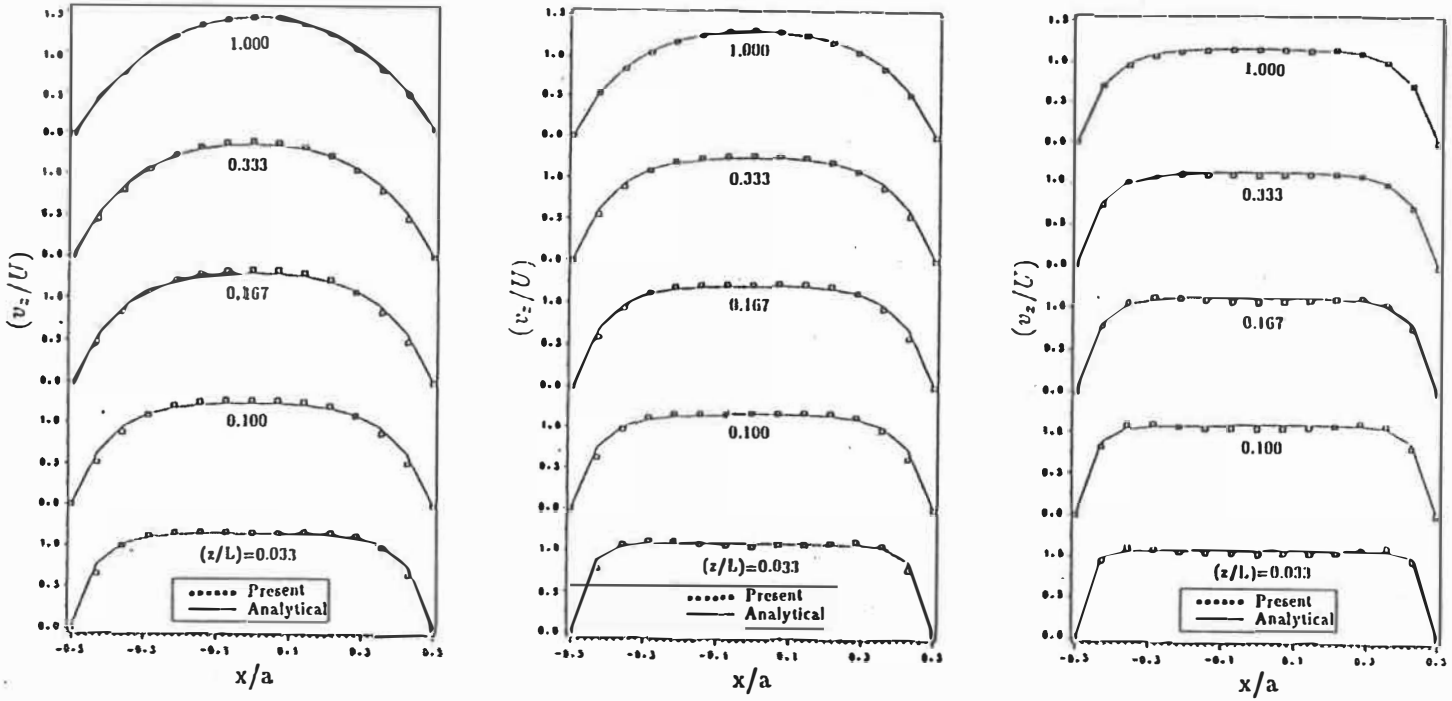




(c) $\omega_1 = 1.0, \omega_2 = 0.0$




(d) $\omega_1 = 0.3, \omega_2 = -0.3$

Figure 7.14: Flow in a Rotating Annulus




(a) $\gamma = 1.0$ (b) $\gamma = 0.5$ (c) $\gamma = 0.25$

Figure 7.15: Passage-Averaged Axial Velocity Profiles

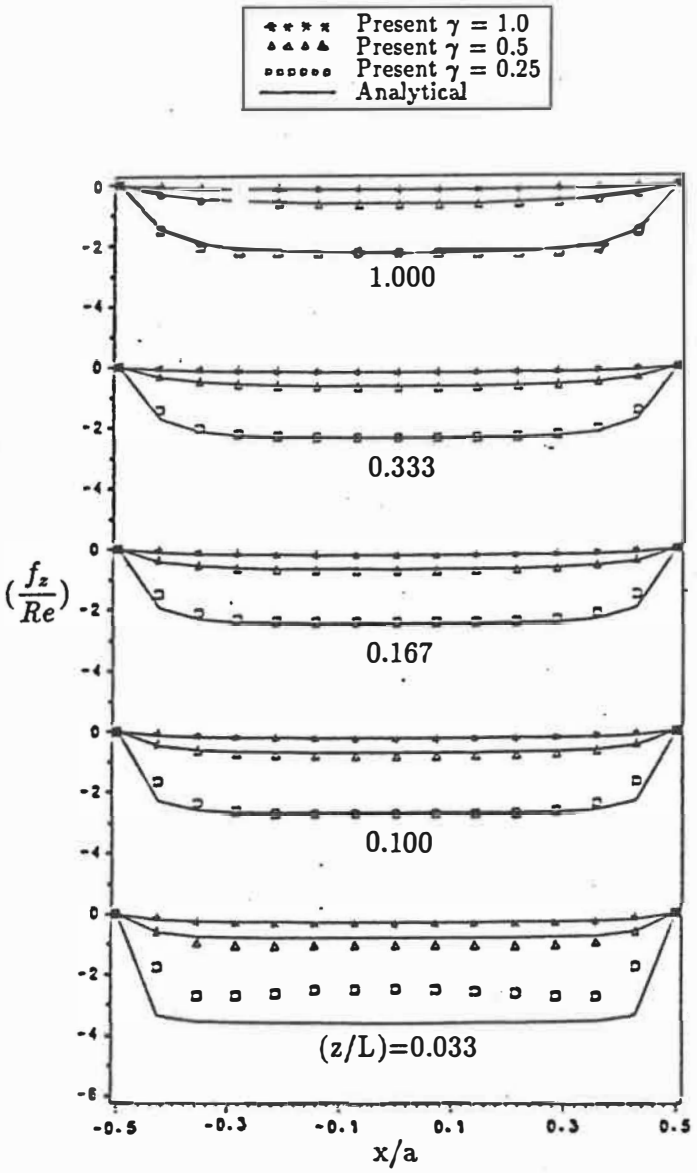



Figure 7.16: Passage-Averaged Shear Force Profiles

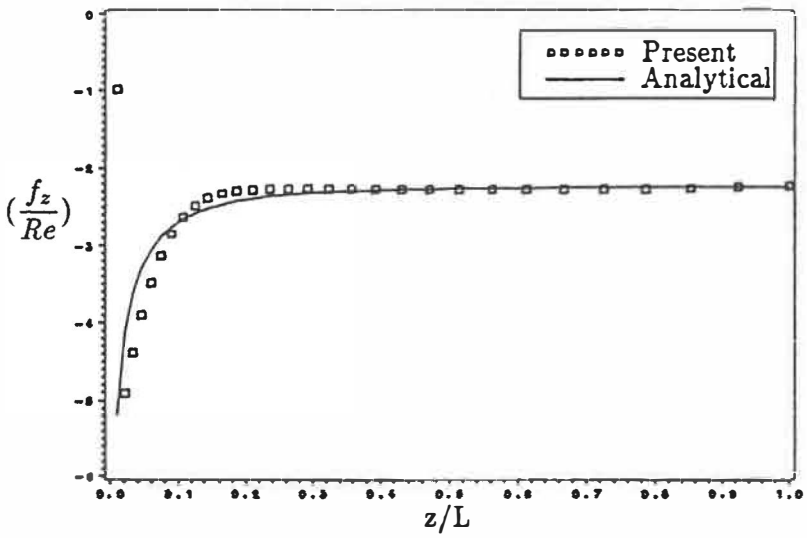



Figure 7.17: Center-Line Shear Force Development with Aspect Ratio $\gamma = 0.25$

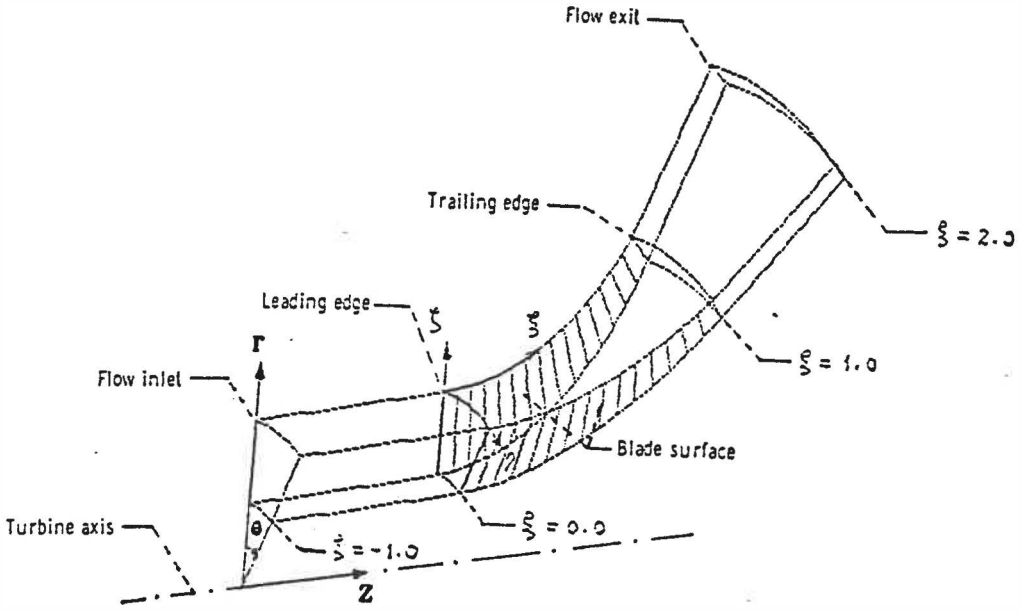
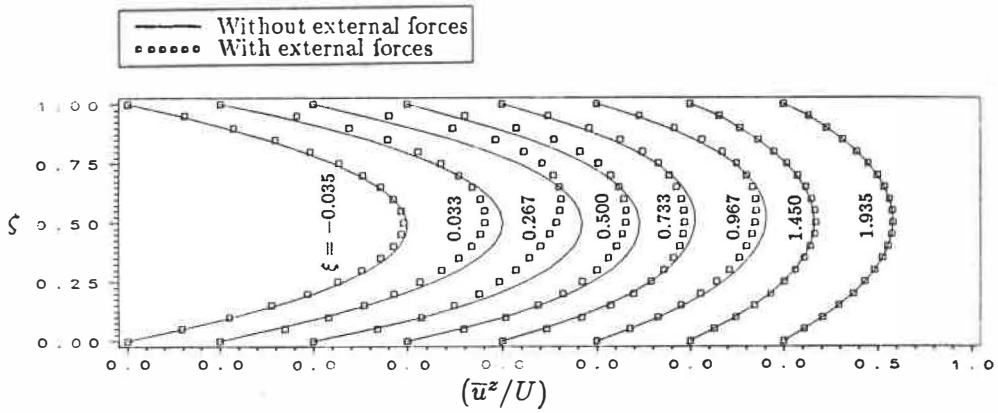
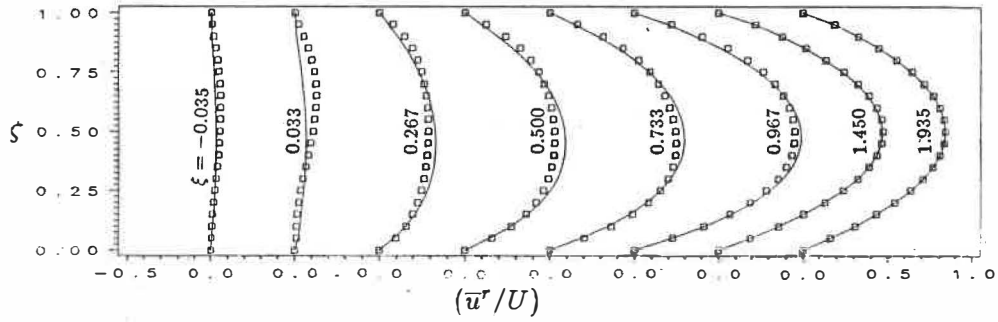


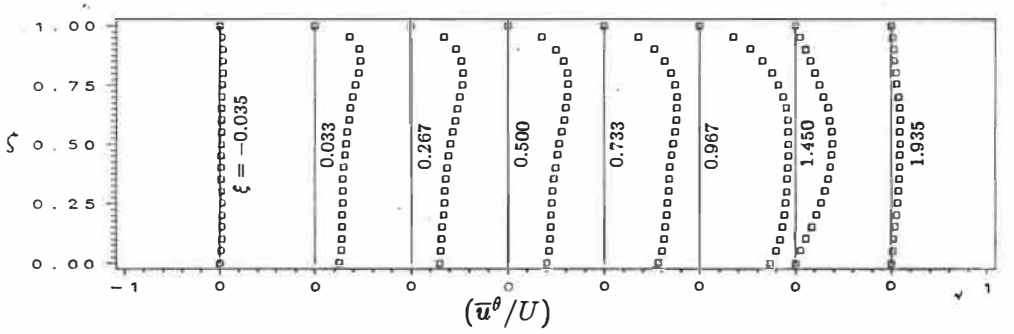

Figure 7.18: Impeller Geometry




(a) Axial velocity

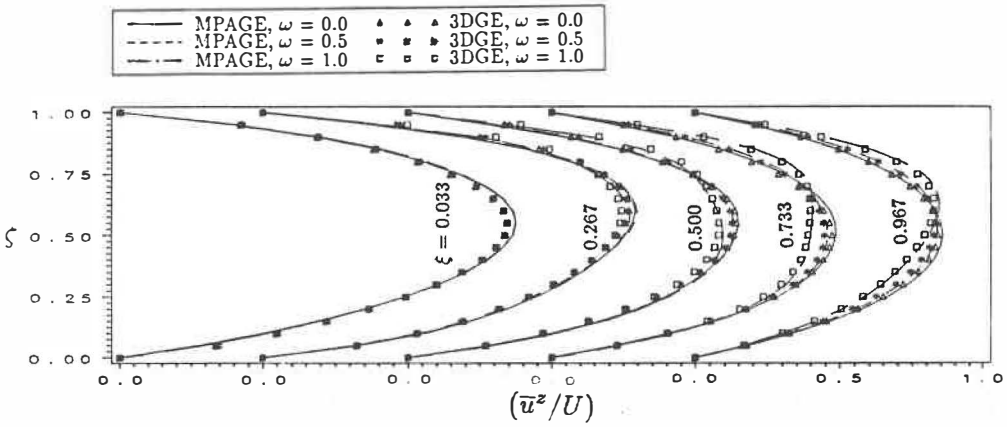



(b) Radial velocity

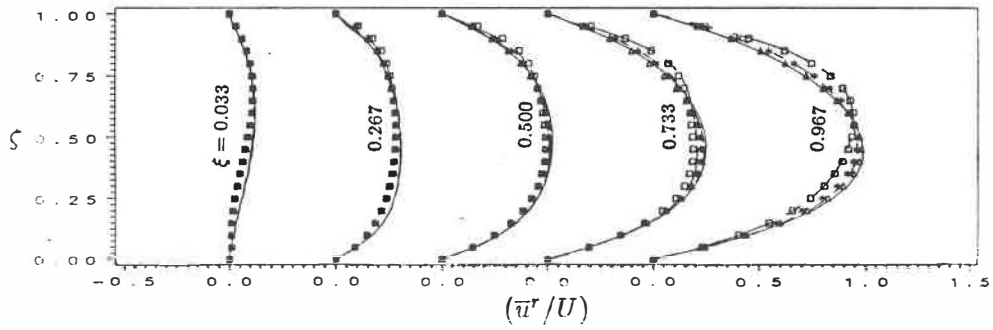



(c) Tangential velocity

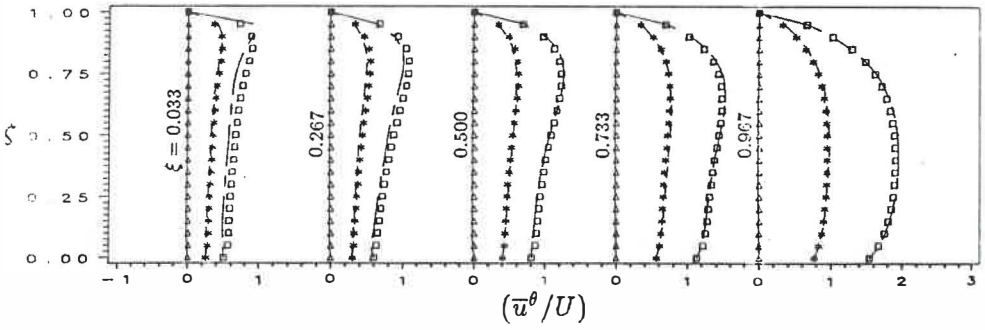
Figure 7.19: Development of Velocity Components with and without the External Forces




(a) Axial velocity

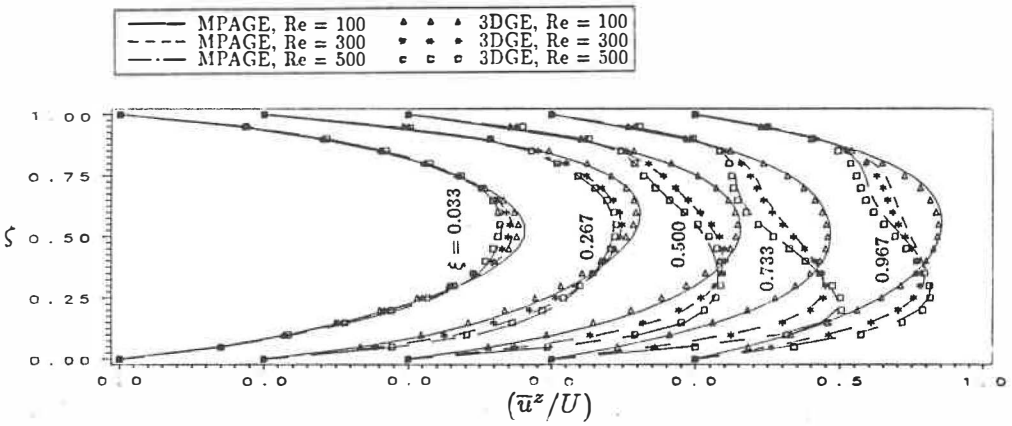



(b) Radial velocity

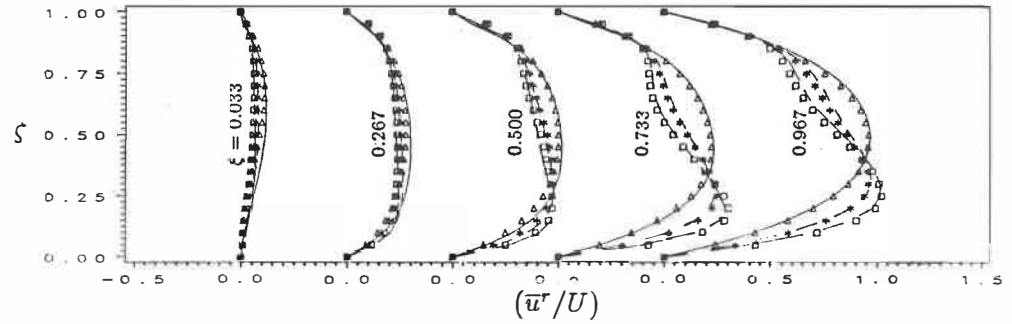



(c) Tangential velocity

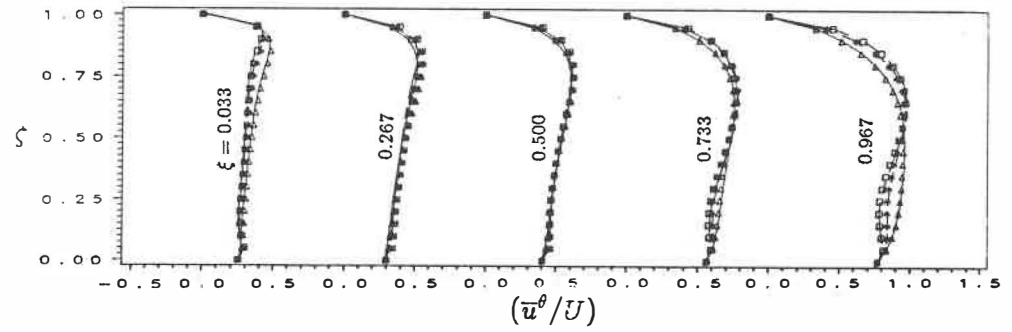
Figure 7.20: Velocity Comparisons with Different Angular Velocities, Re = 100




(a) Axial velocity

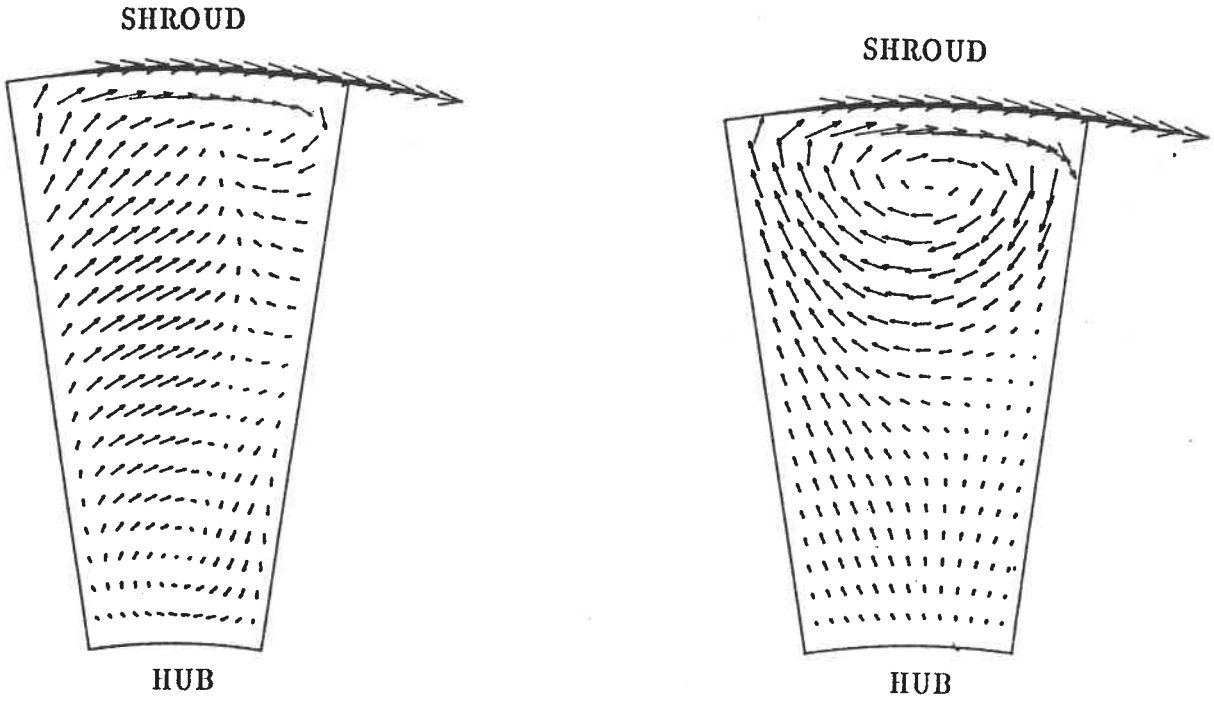



(b) Radial velocity



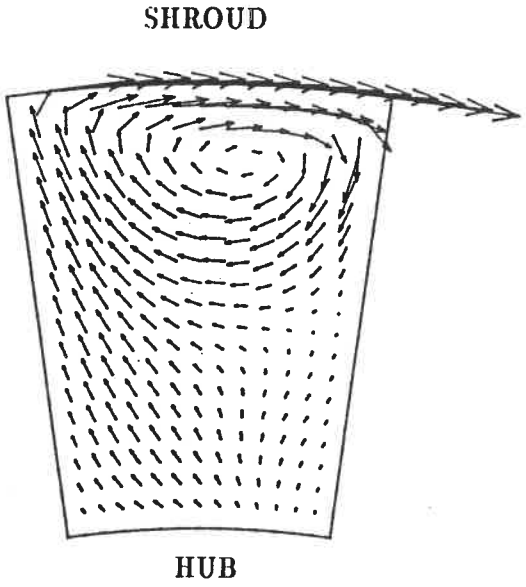

(c) Tangential velocity

Figure 7.21: Velocity Comparisons with Different Reynolds Numbers, $\omega = 0.5$

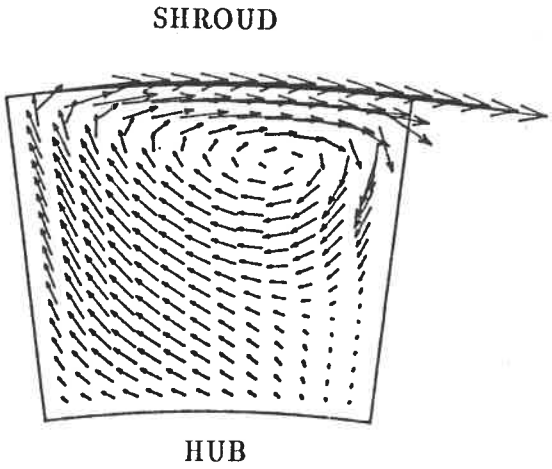



(a) $\xi = 0.033$ (b) $\xi = 0.267$

Figure 7.22: Secondary Velocity Vectors, Re = 100, $\omega = 1.0$



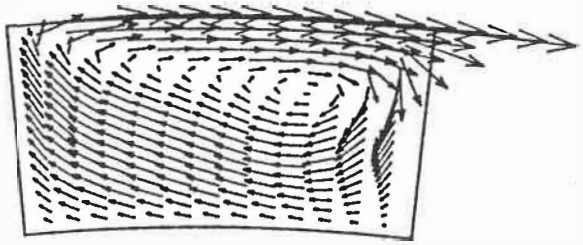

(c) $\xi = 0.500$




(d) $\xi = 0.733$

Figure 7.22: Secondary Velocity Vectors, Re = 100, $\omega = 1.0$

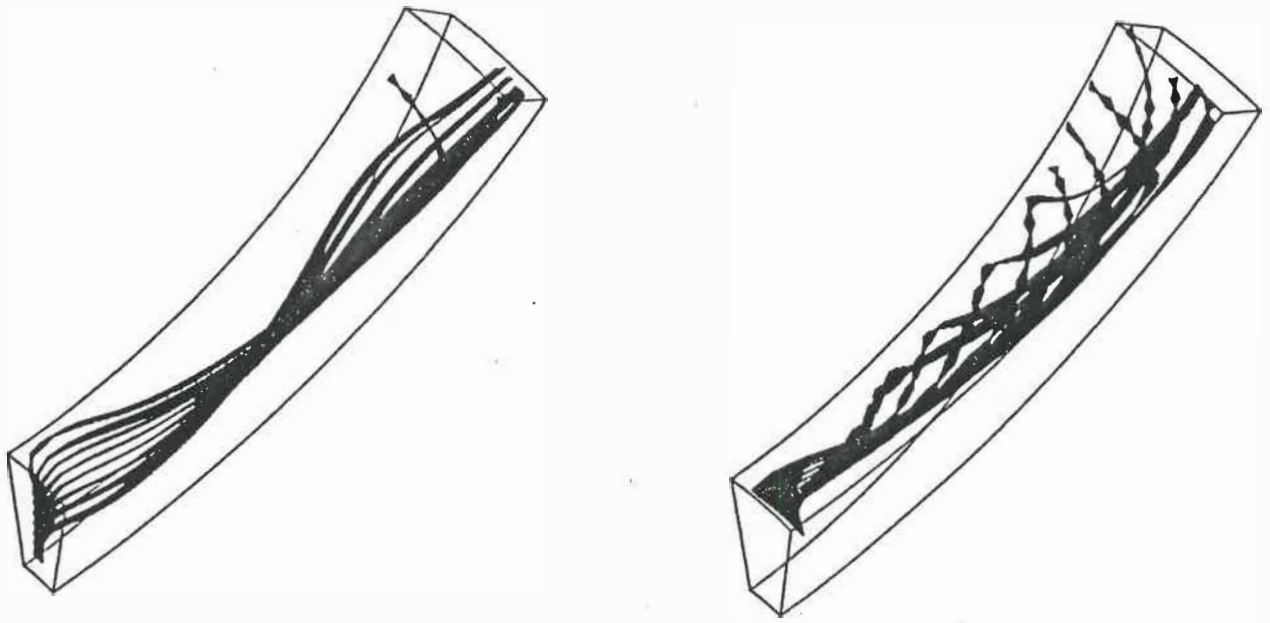
SHROUD



HUB

(e) $\xi = 0.967$

Figure 7.22: Secondary Velocity Vectors, Re = 100, $\omega$ = 1.0



(a) Inlet Hub-to-Shroud streamsurface

(b) Inlet Blade-to-Blade streamsurface

Figure 7.23: Ribbon Patterns within Impeller, Re = 100, $\omega = 1.0$

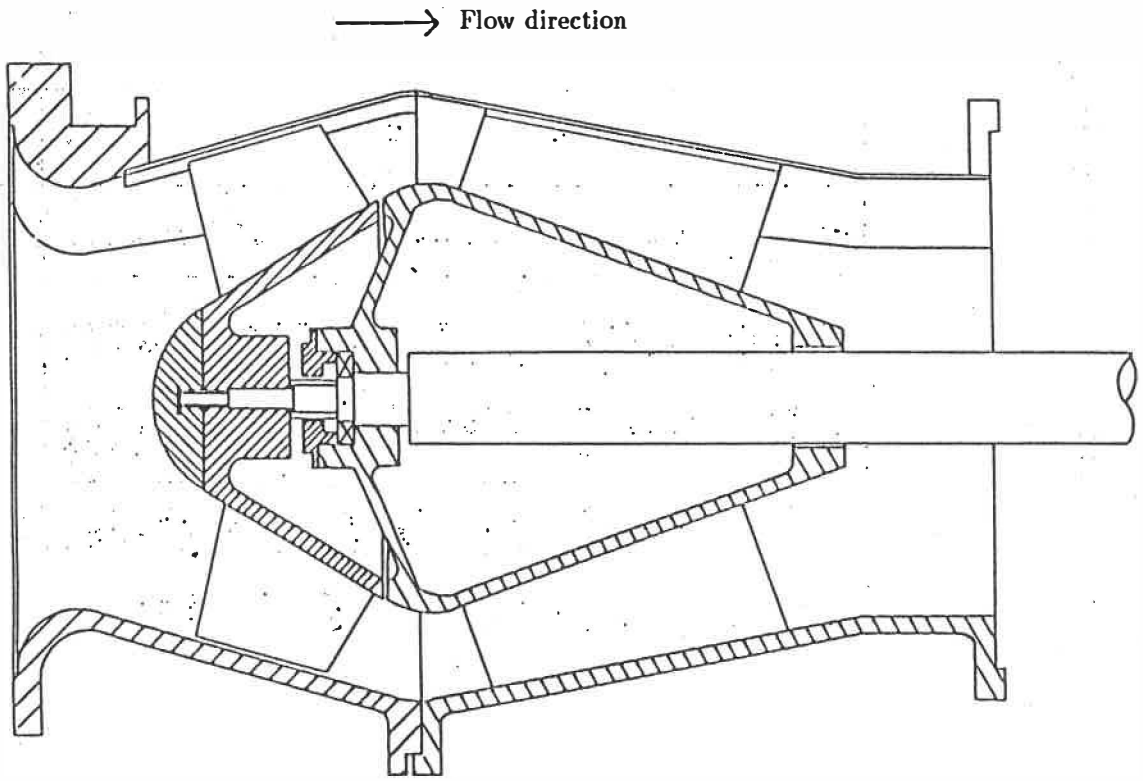



Figure 8.1: Cross-Section Through the Mixed-Flow Pump
(From Carey et al. 1985a)

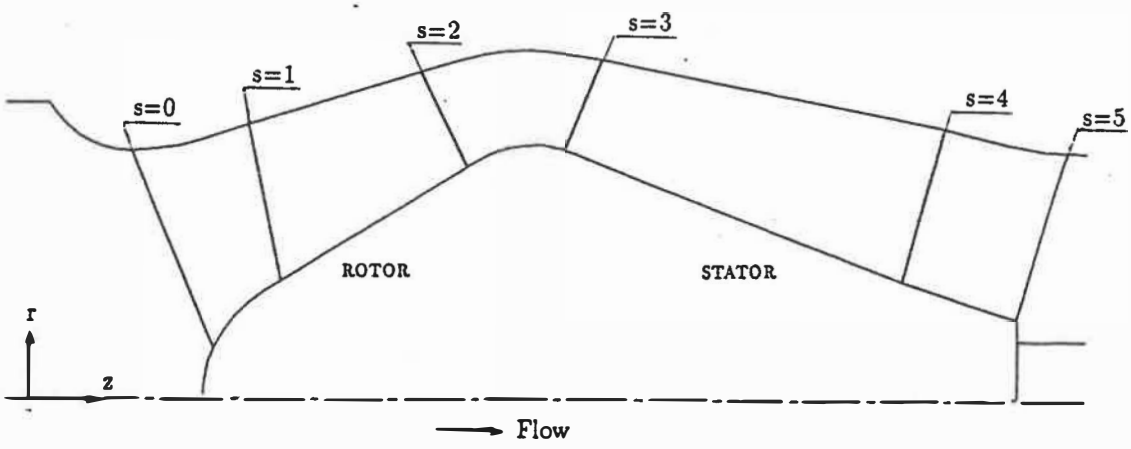
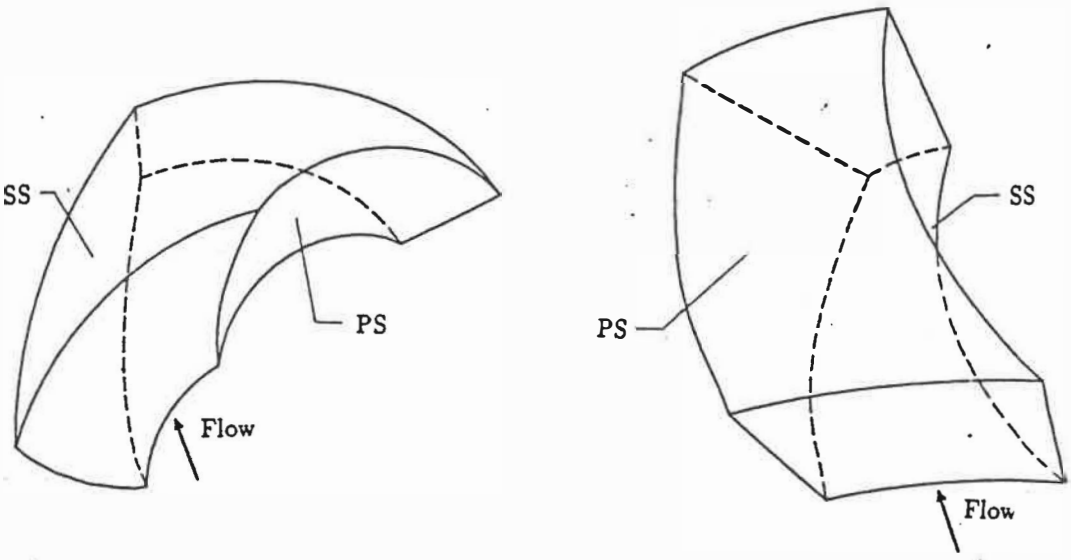



Figure 8.2: Domain for the MPAGE Computation




(a) Rotor

(b) Stator

Figure 8.3: Domains for the 3DGE Computations

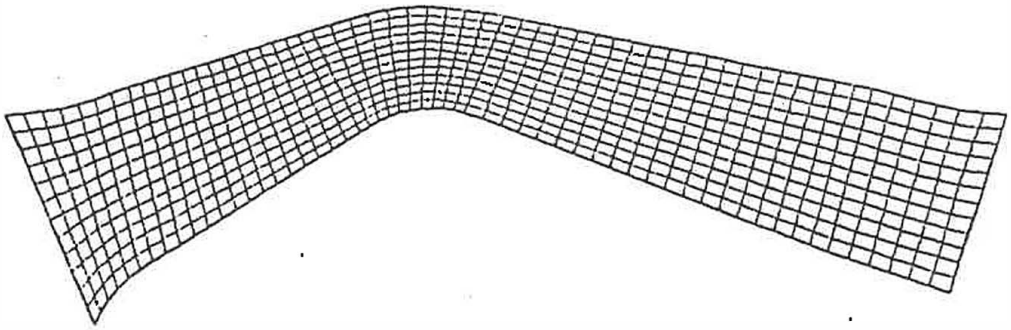
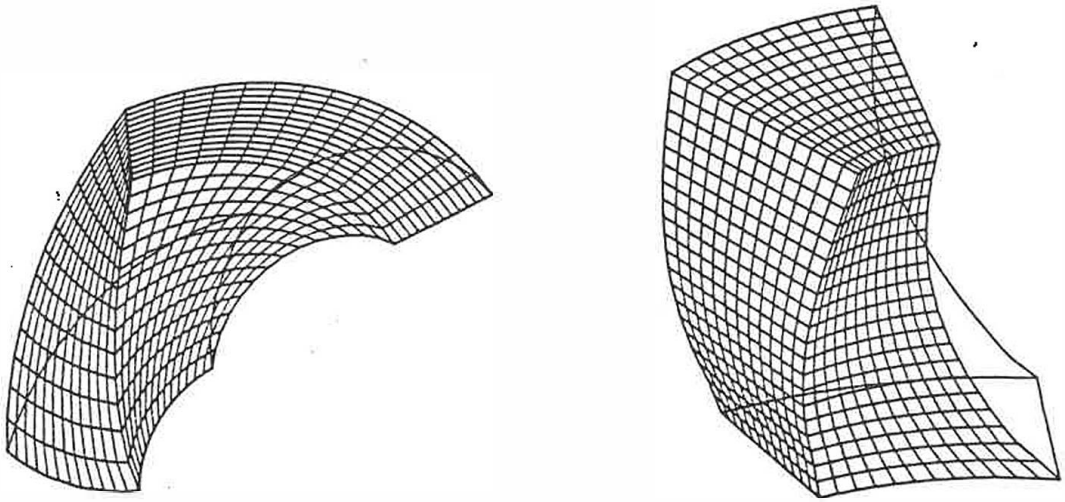


Figure 8.4: Grid for the MPAGE Computation



(a) Rotor

(b) Stator

Figure 8.5: Grids for the 3DGE Computations

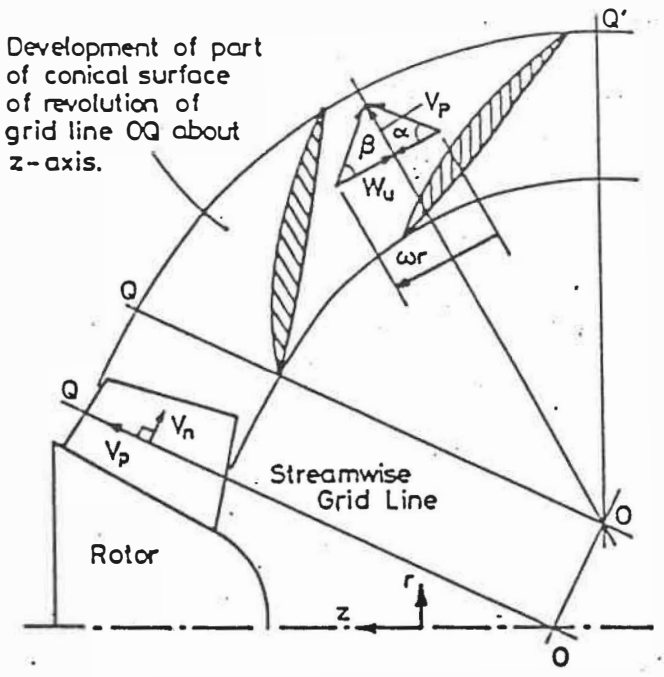



Figure 8.6: Definition of Velocity Components (From Carey et al. 1985b)

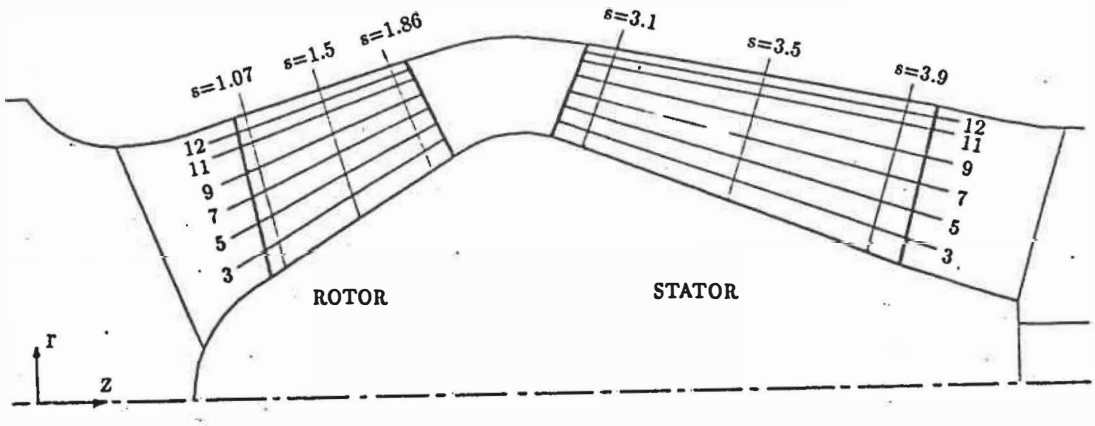
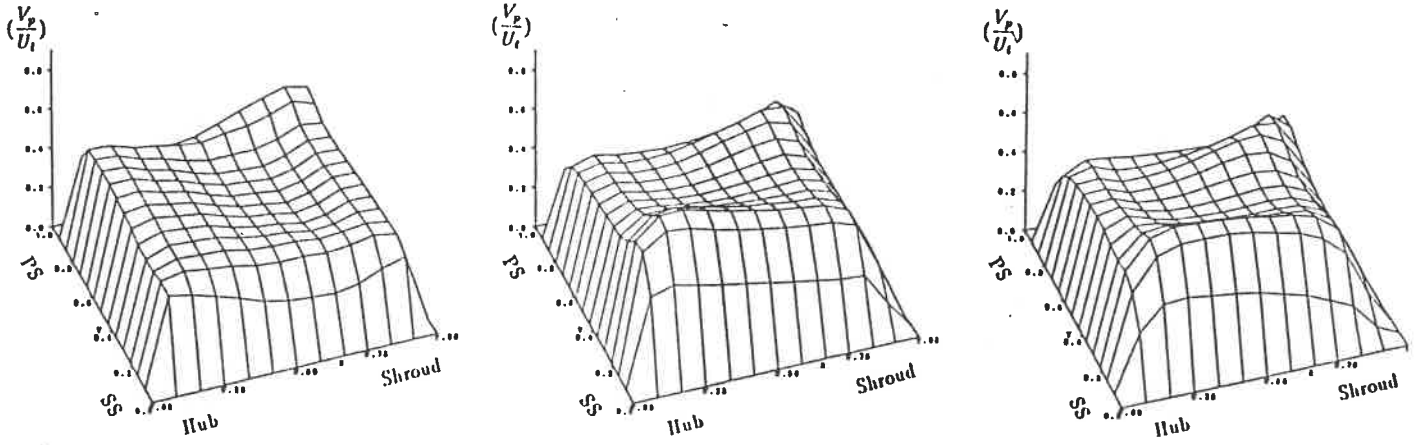
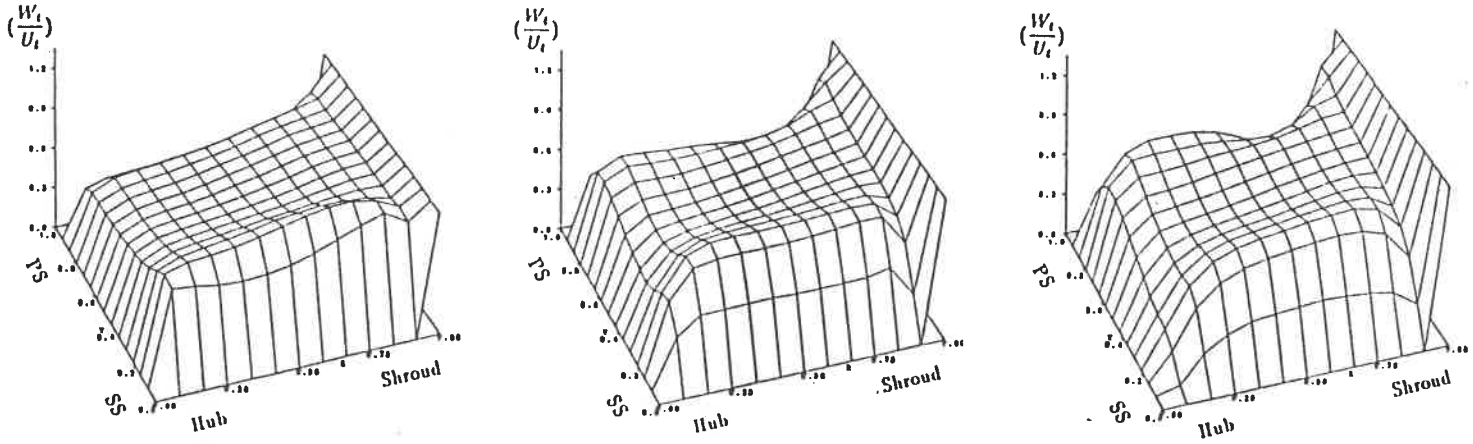



Figure 8.7: Station Locations



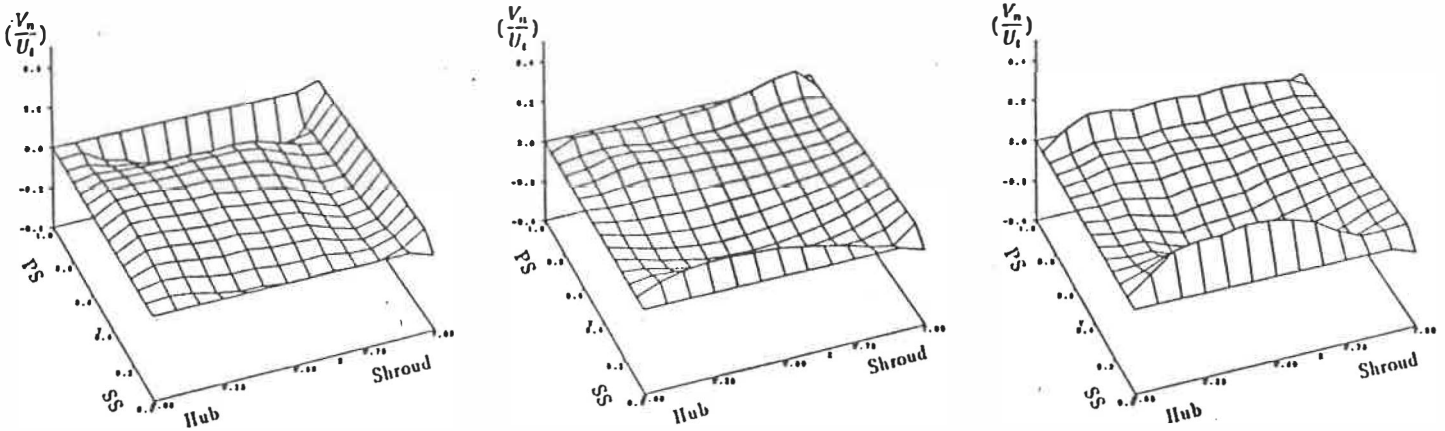

(a) s=1.07 (b) s=1.50 (c) s=1.86

Figure 8.8: Surface Plots for Component $V_p$, Rotor



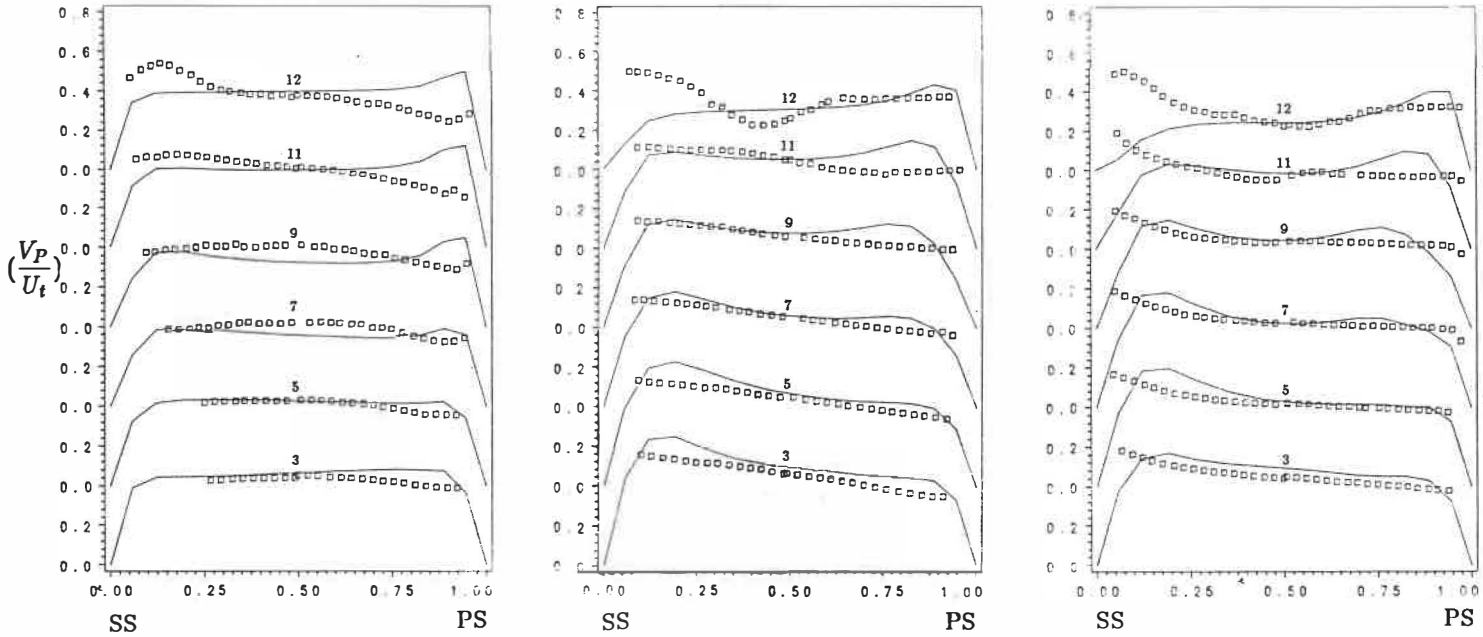

(a) s=1.07 (b) s=1.50 (c) s=1.86

Figure 8.9: Surface Plots for Component $W_t$, Rotor




(a) s=1.07 (b) s=1.50 (c) s=1.86

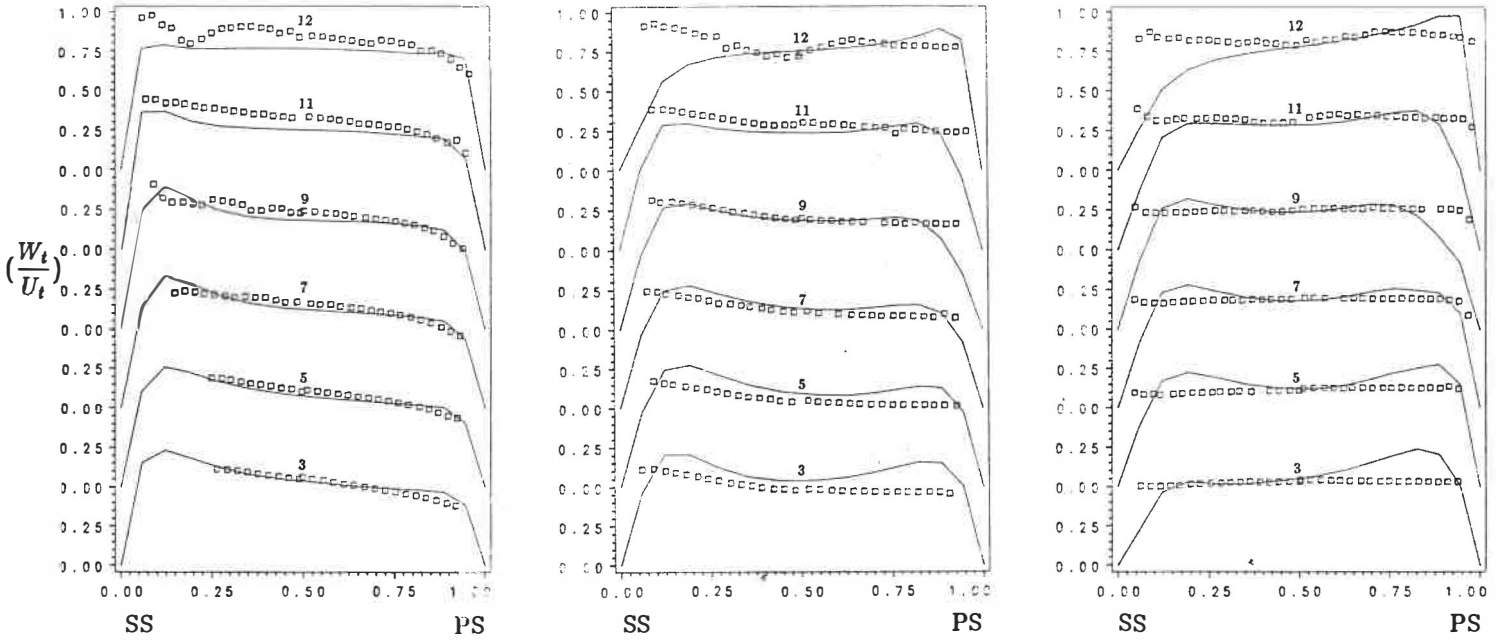
Figure 8.10: Surface Plots for Component $V_n$, Rotor




(a) s = 1.07 (b) s = 1.50 (c) s = 1.86

Figure 8.11: Blade-to-Blade Velocity Component $V_p$, Rotor

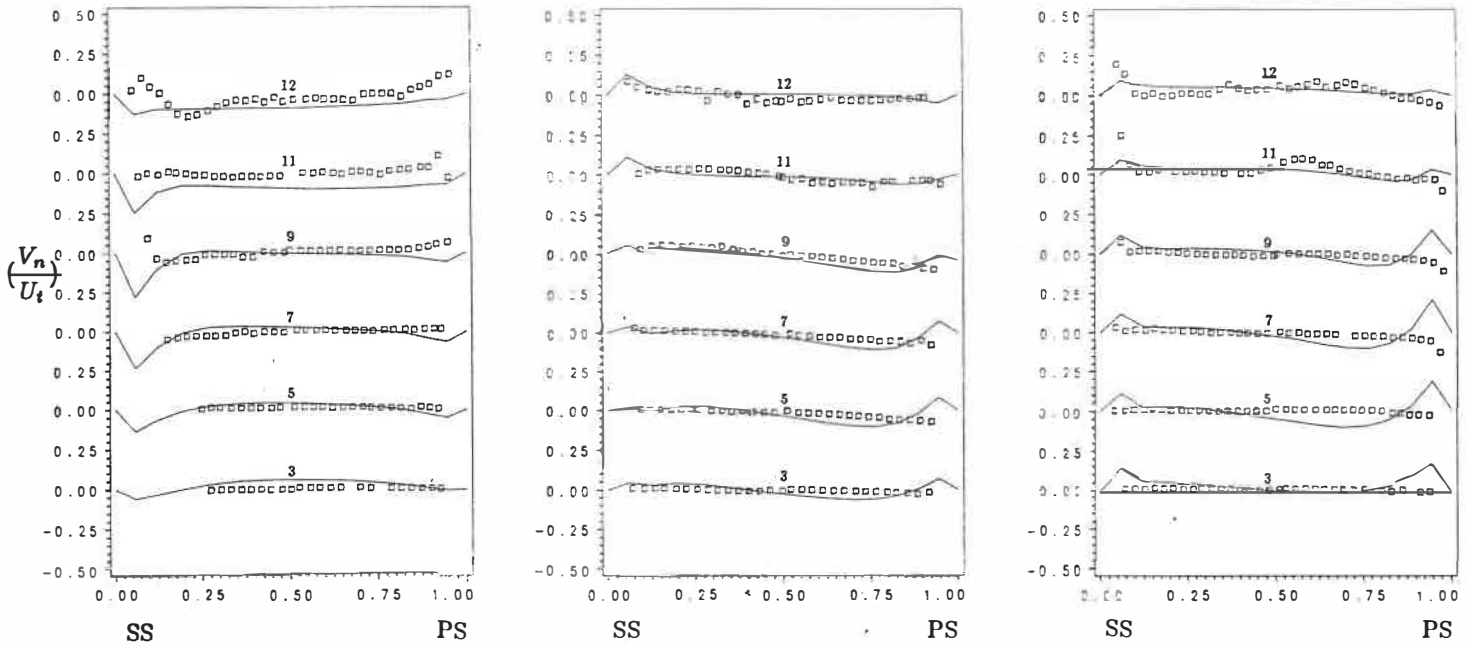
( ——— Present , ▫▫▫▫▫▫ Exp.(Carey et al.) )




(a) s = 1.07 (b) s = 1.50 (c) s = 1.86

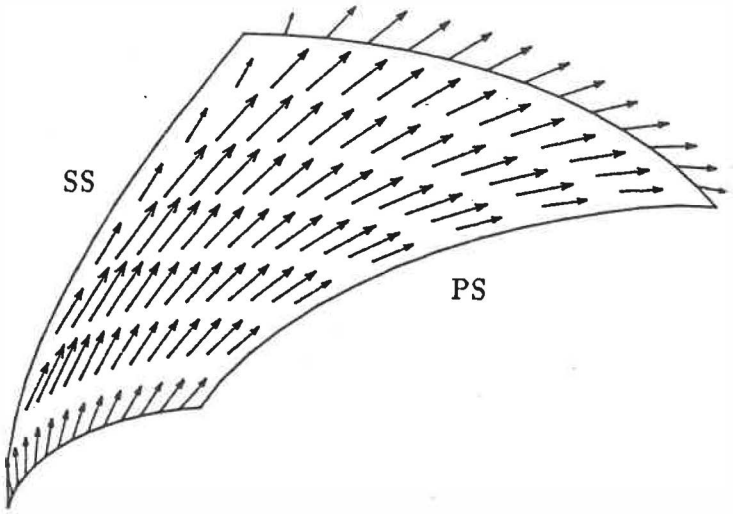
Figure 8.12: Blade-to-Blade Velocity Component $W_t$, Rotor

( —— Present , ▫▫▫▫▫ Exp.(Carey et al.))

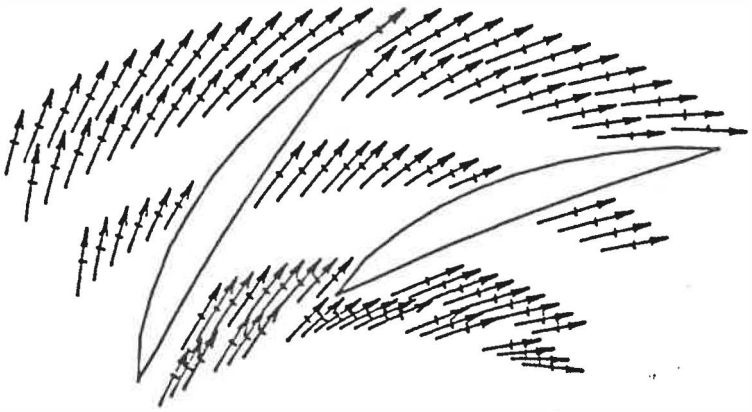



(a) s = 1.07 (b) s = 1.50 (c) s = 1.86

Figure 8.13: Blade-to-Blade Velocity Component $V_n$, Rotor
(——— Present , ◦◦◦◦◦◦ Exp.(Carey et al.))

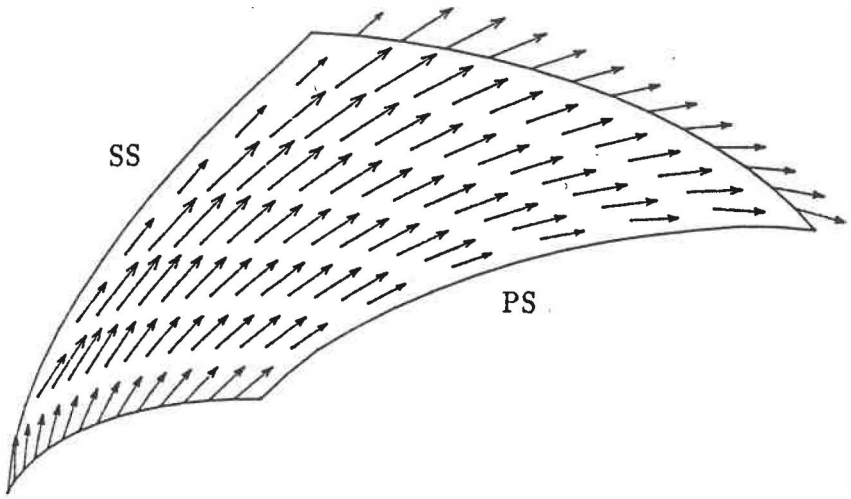



(i) Present

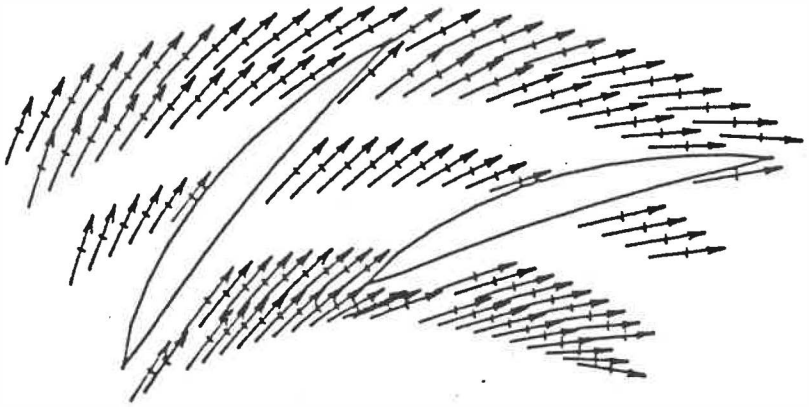


(ii) Experiment

Figure 8.14a: Blade-to-Blade Velocity Vector at R = 0.167, Rotor

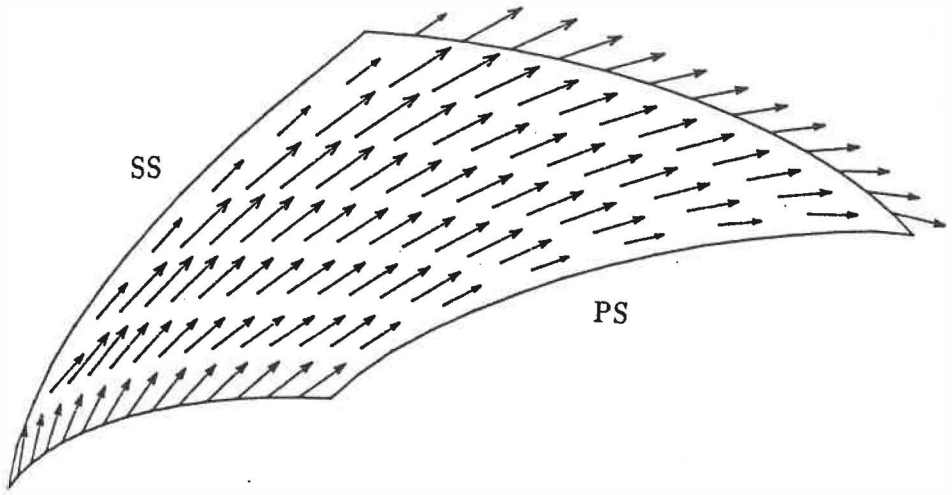



(i) Present

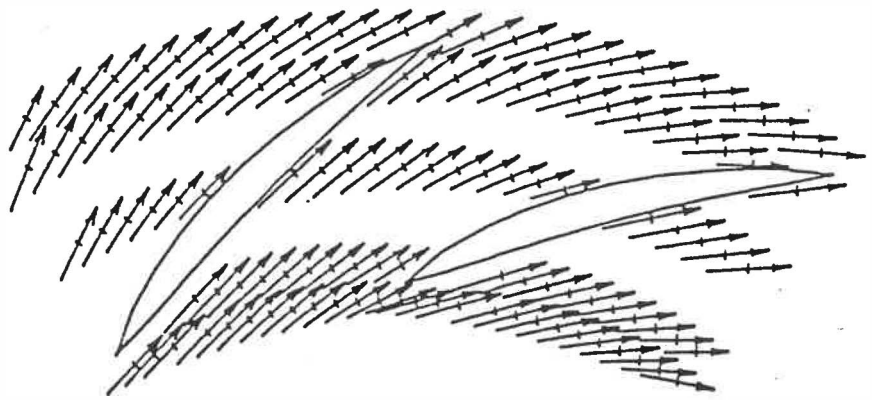


(ii) Experiment

Figure 8.14b: Blade-to-Blade Velocity Vector at R = 0.333, Rotor

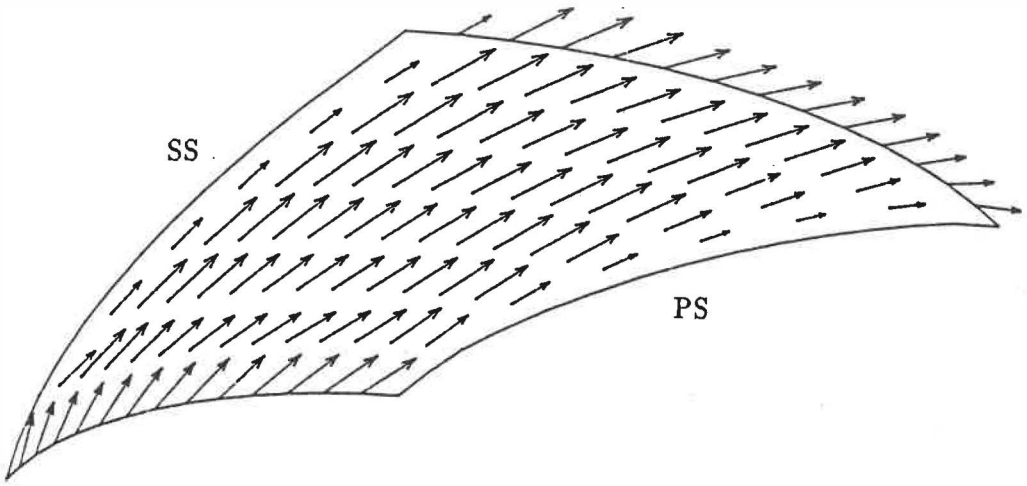



(i) Present

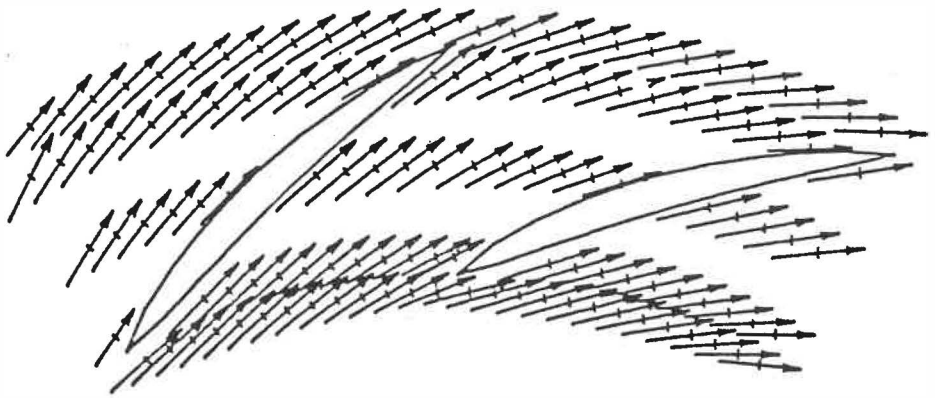


(ii) Experiment

Figure 8.14c: Blade-to-Blade Velocity Vector at R = 0.500, Rotor

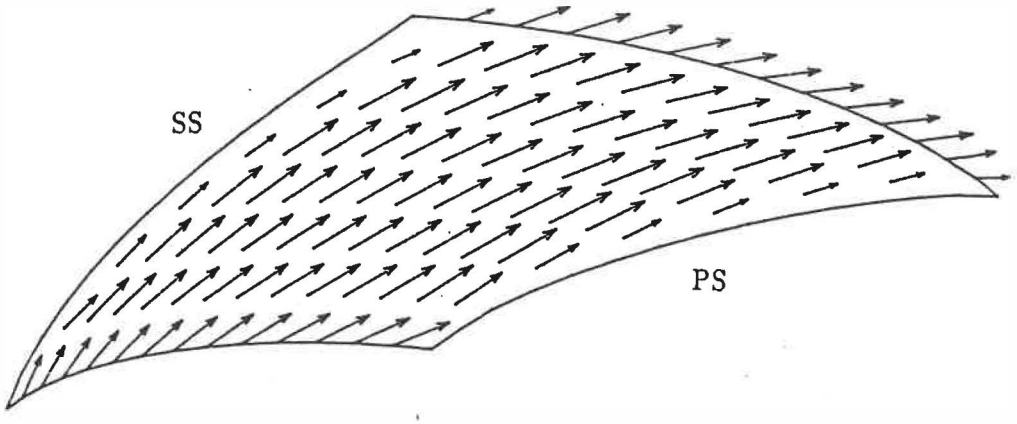



(i) Present

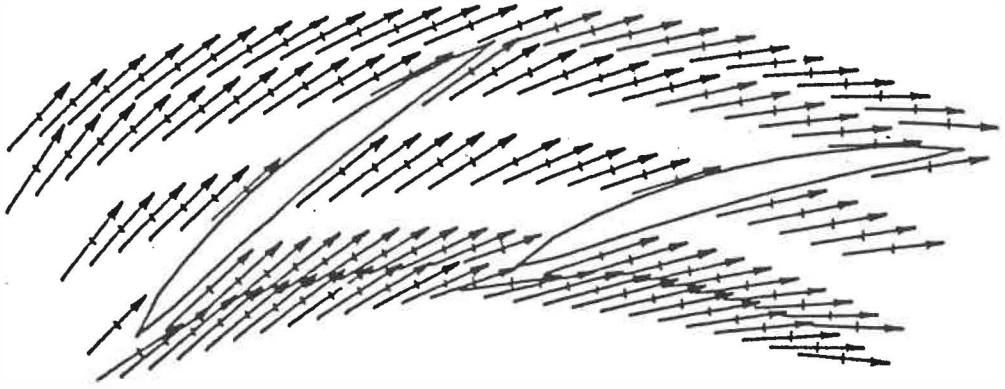


(ii) Experiment

Figure 8.14d: Blade-to-Blade Velocity Vector at R = 0.667, Rotor

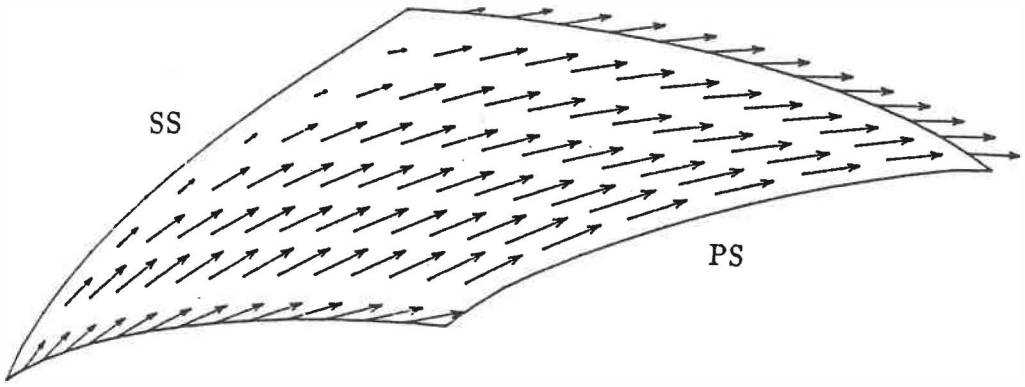



(i) Present

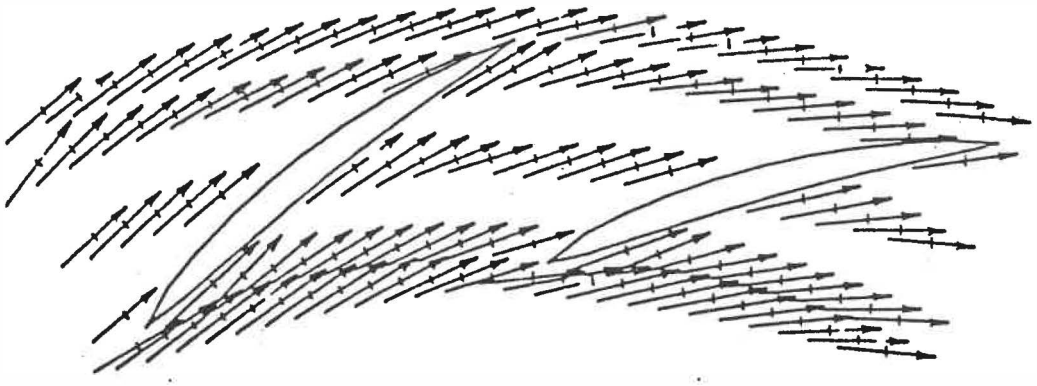


(ii) Experiment

Figure 8.14e: Blade-to-Blade Velocity Vector at R = 0.833, Rotor

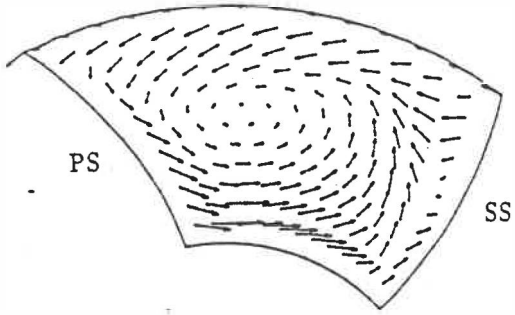



(i) Present

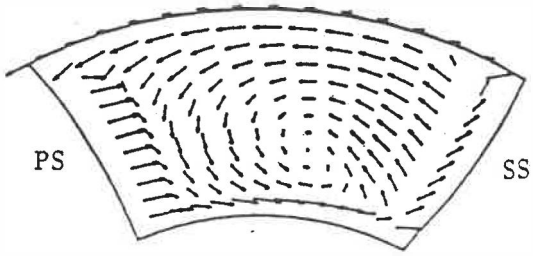


(ii) Experiment

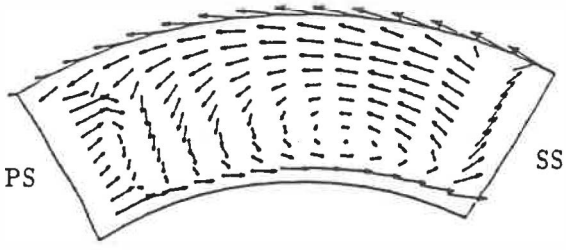
Figure 8.14f: Blade-to-Blade Velocity Vector at R = 0.917, Rotor




(a) s=1.07

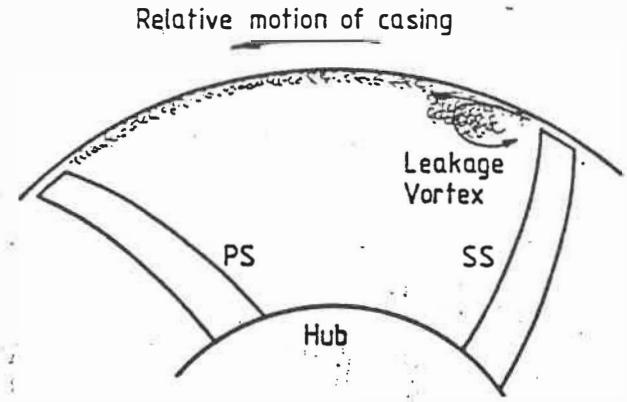



(b) s=1.50

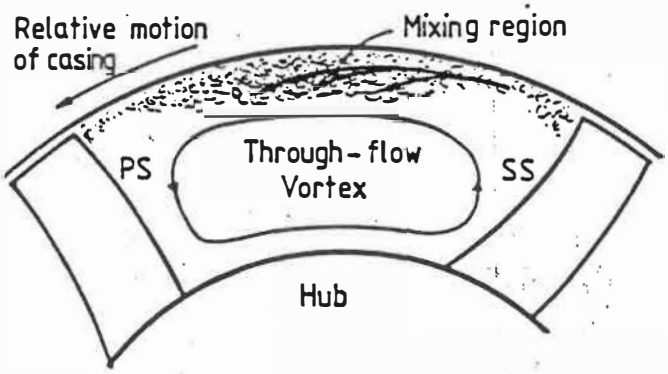



(c) s=1.86

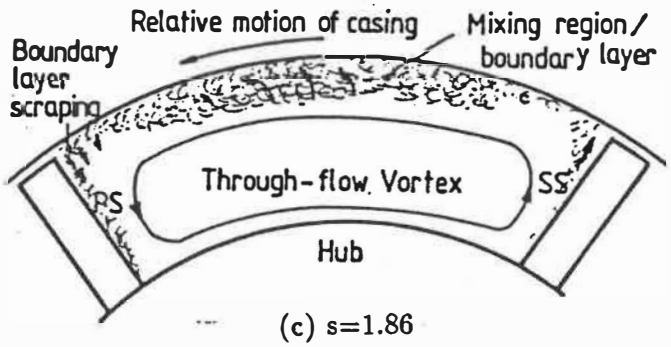
Figure 8.15: Secondary Velocity Vectors, Rotor




(a) s=1.07

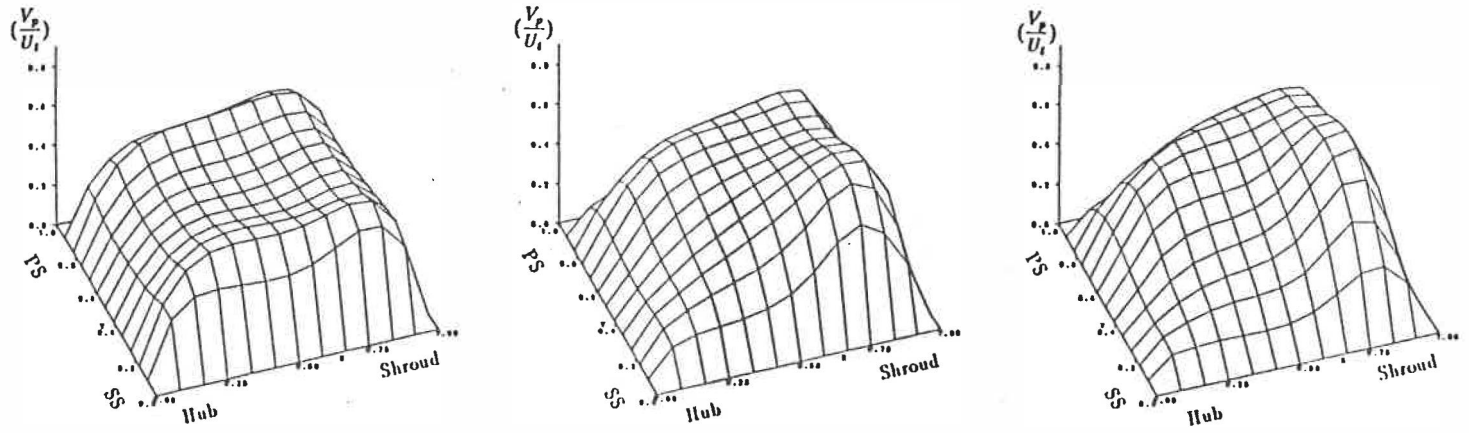



(b) s=1.50



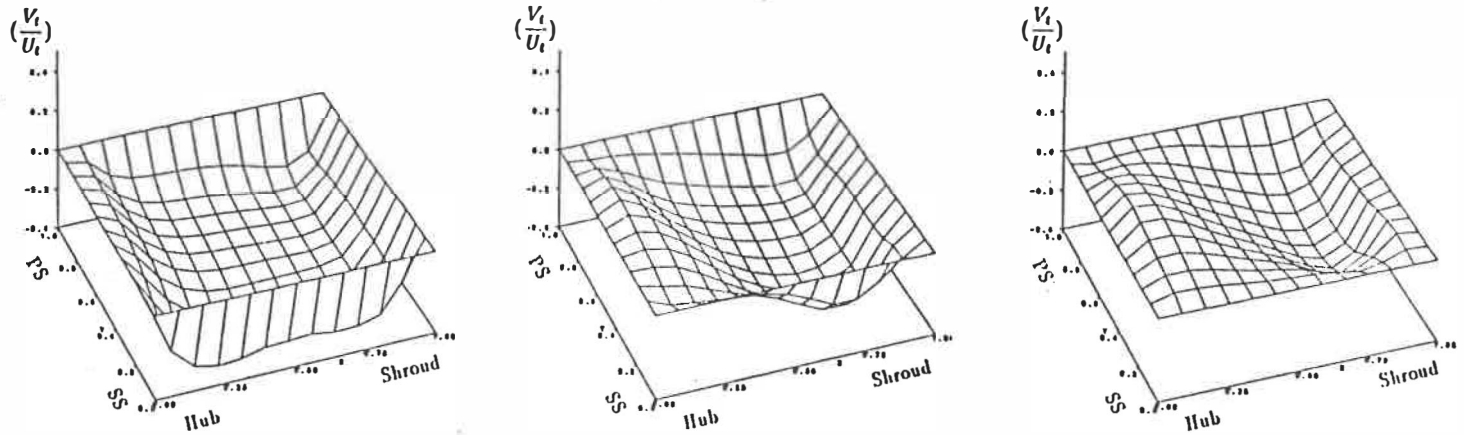

(c) s=1.86

Figure 8.16: Flow Phenomena with Tip Leakage Flow, Rotor
(From Carey et al. 1985b)



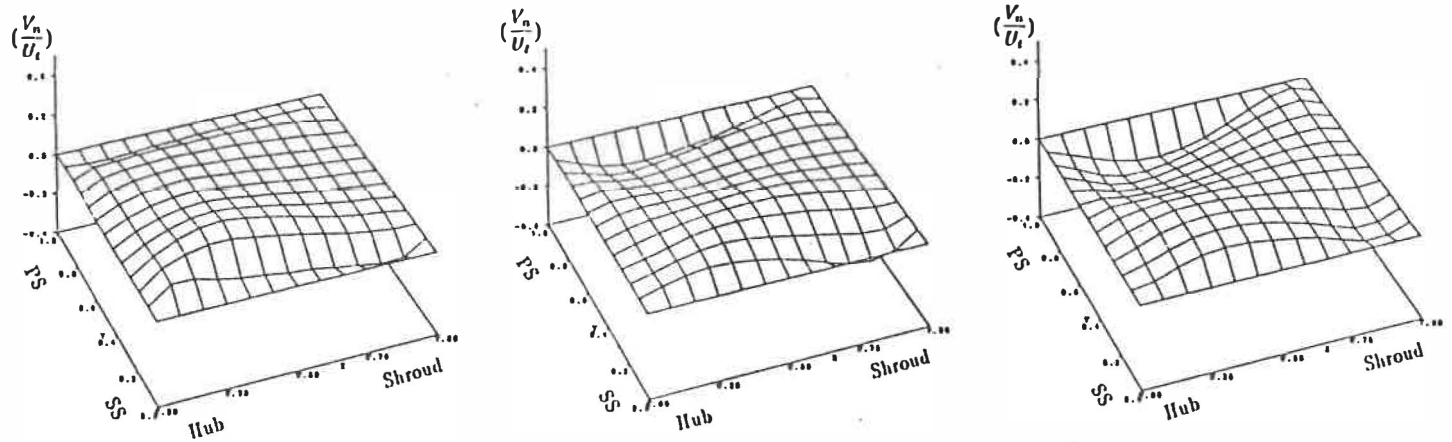

(a) s=3.1 (b) s=3.5 (c) s=3.9

Figure 8.17: Surface Plots for Component $V_p$, Stator



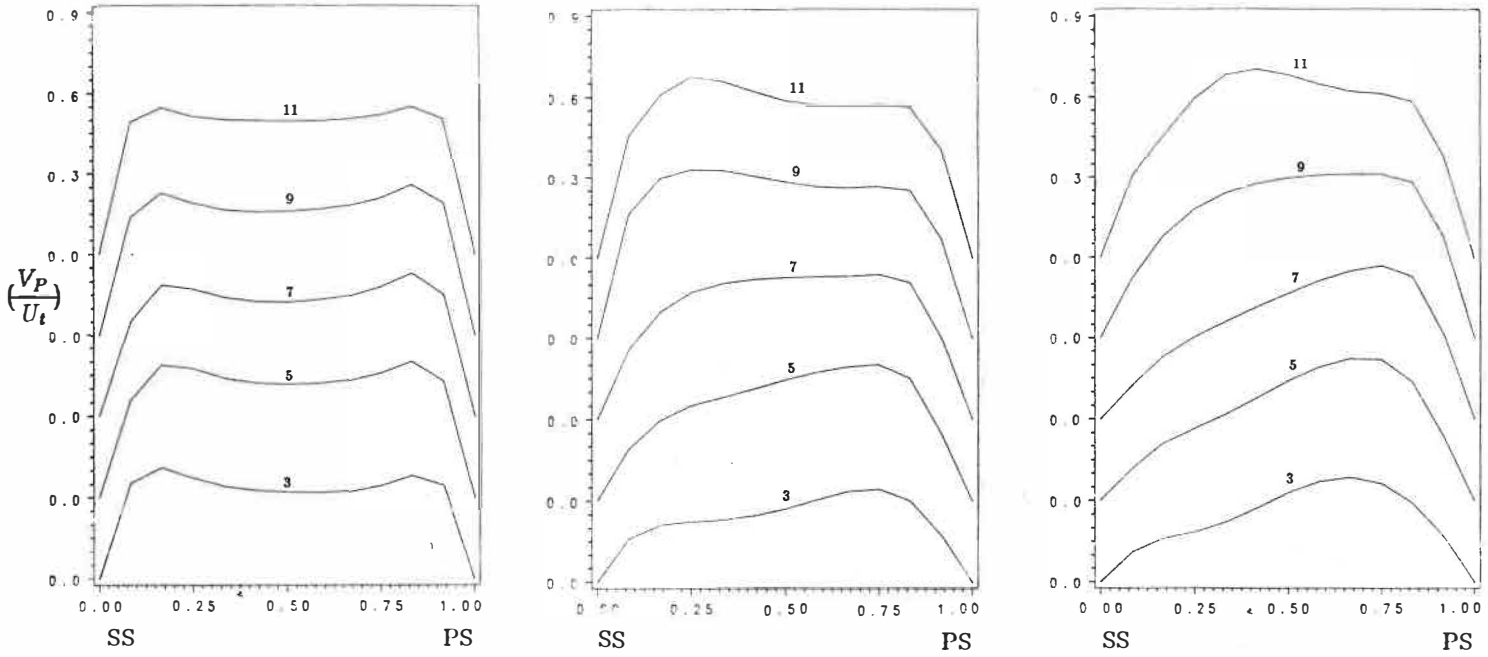

(a) s=3.1 (b) s=3.5 (c) s=3.9

Figure 8.18: Surface Plots for Component $V_t$, Stator



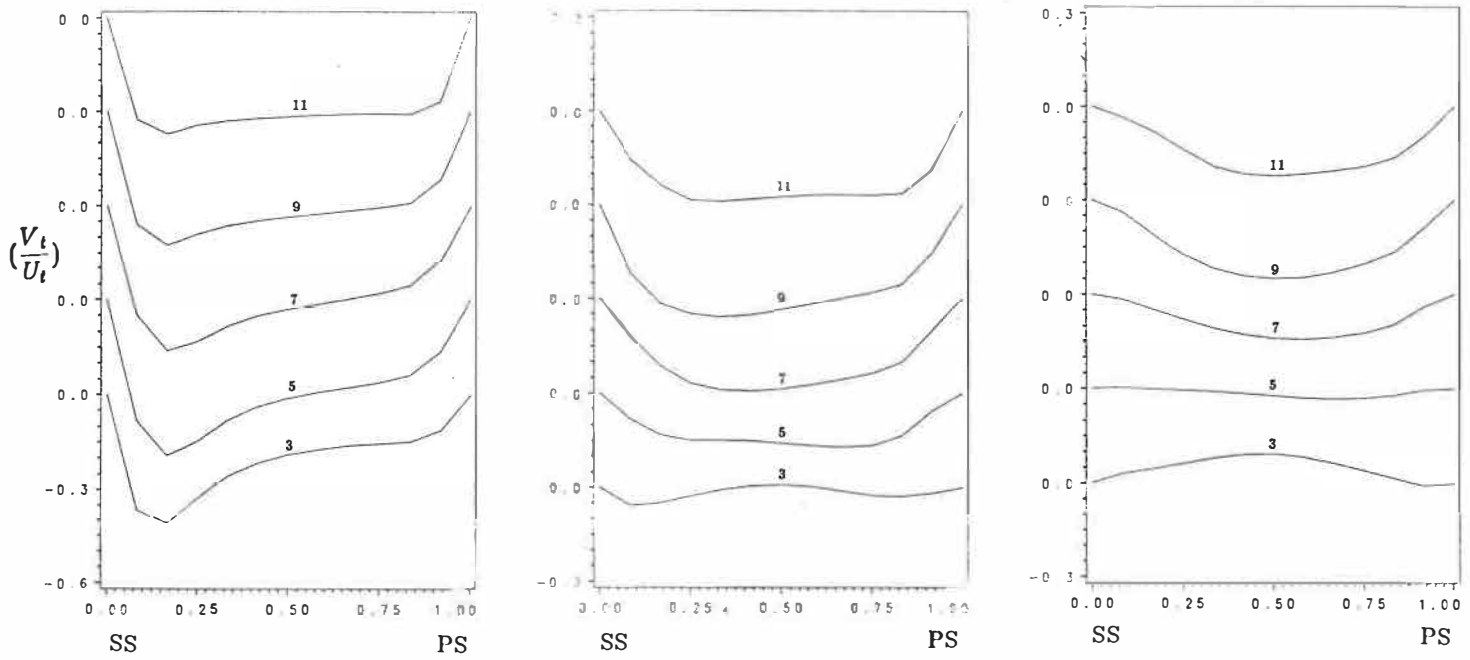

(a) s=3.1 (b) s=3.5 (c) s=3.9

Figure 8.19: Surface Plots for Component $V_n$, Stator



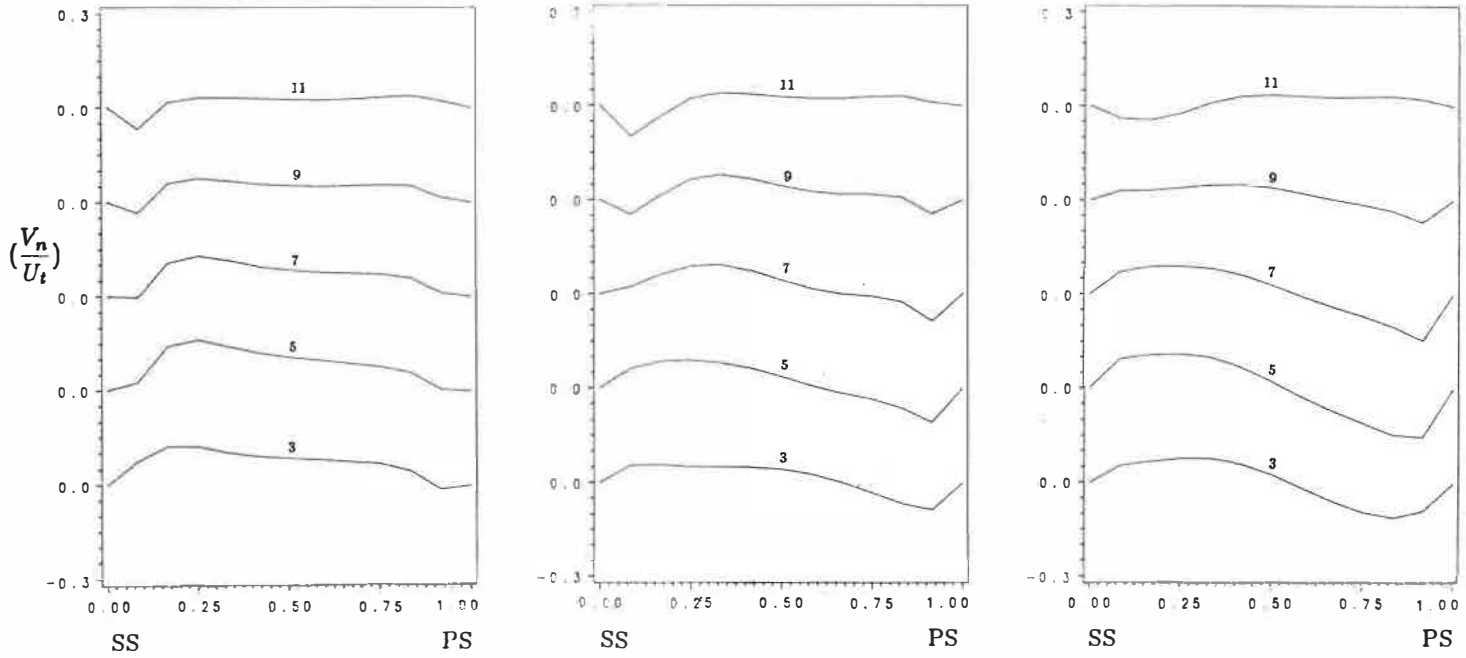

(a) s = 3.1 (b) s = 3.5 (c) s = 3.9

Figure 8.20: Blade-to-Blade Velocity Component $V_p$, Stator



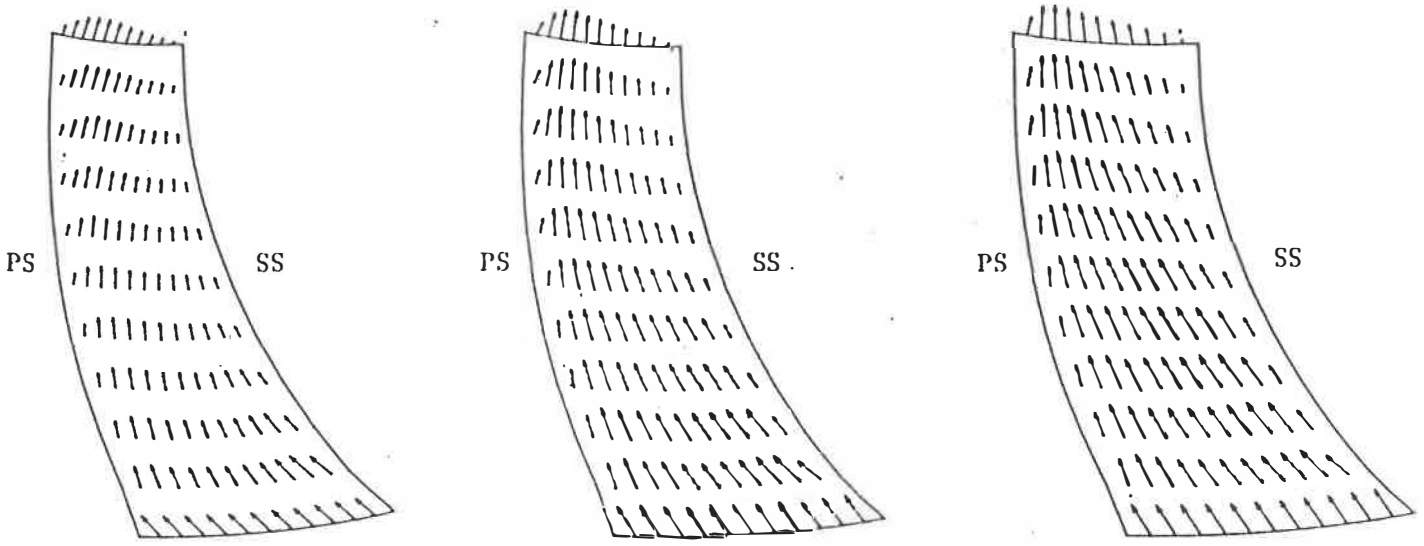

(a) s = 3.1 (b) s = 3.5 (c) s = 3.9

Figure 8.21: Blade-to-Blade Velocity Component $V_t$, Stator



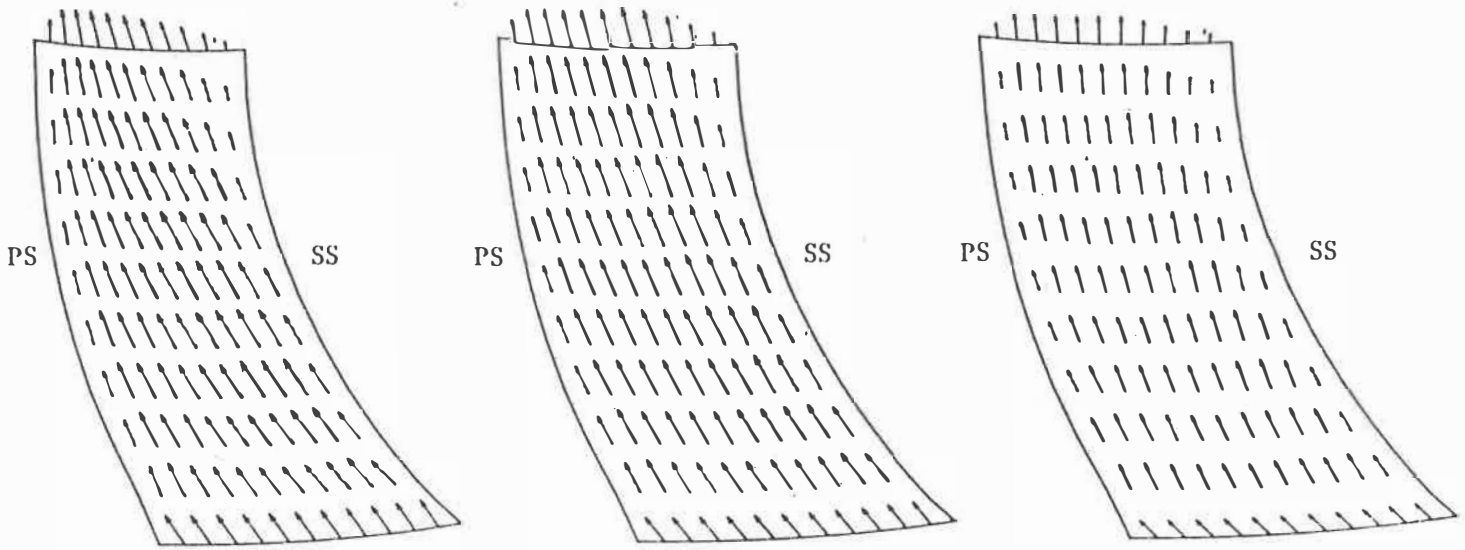

(a) s = 3.1 (b) s = 3.5 (c) s = 3.9

Figure 8.22: Blade-to-Blade Velocity Component $V_n$, Stator



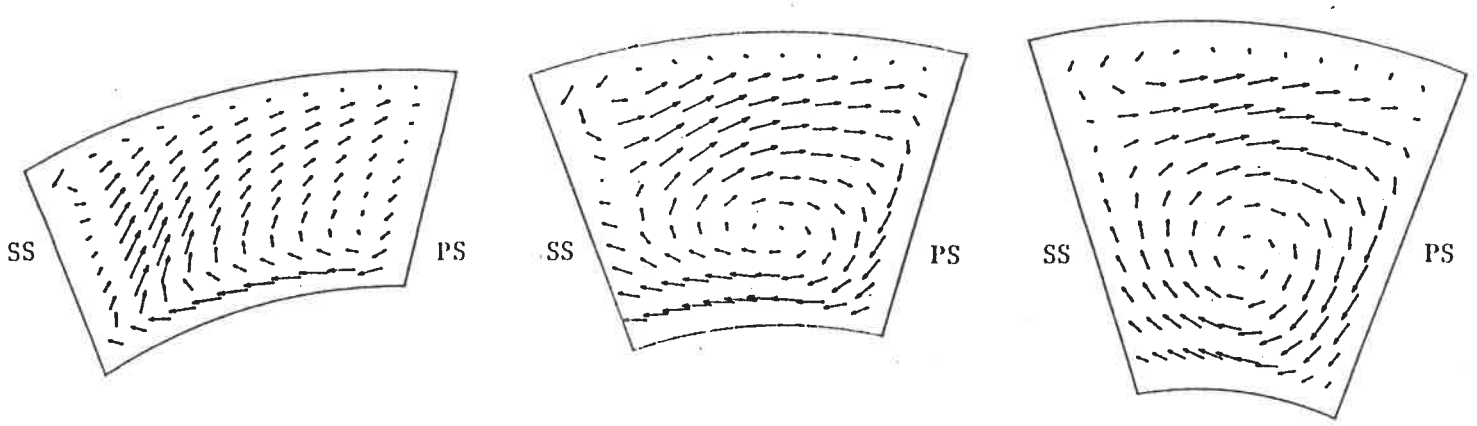

(a) R = 0.167 (b) R = 0.333 (c) R = 0.500

Figure 8.23: Blade-to-Blade Velocity Vector, Stator



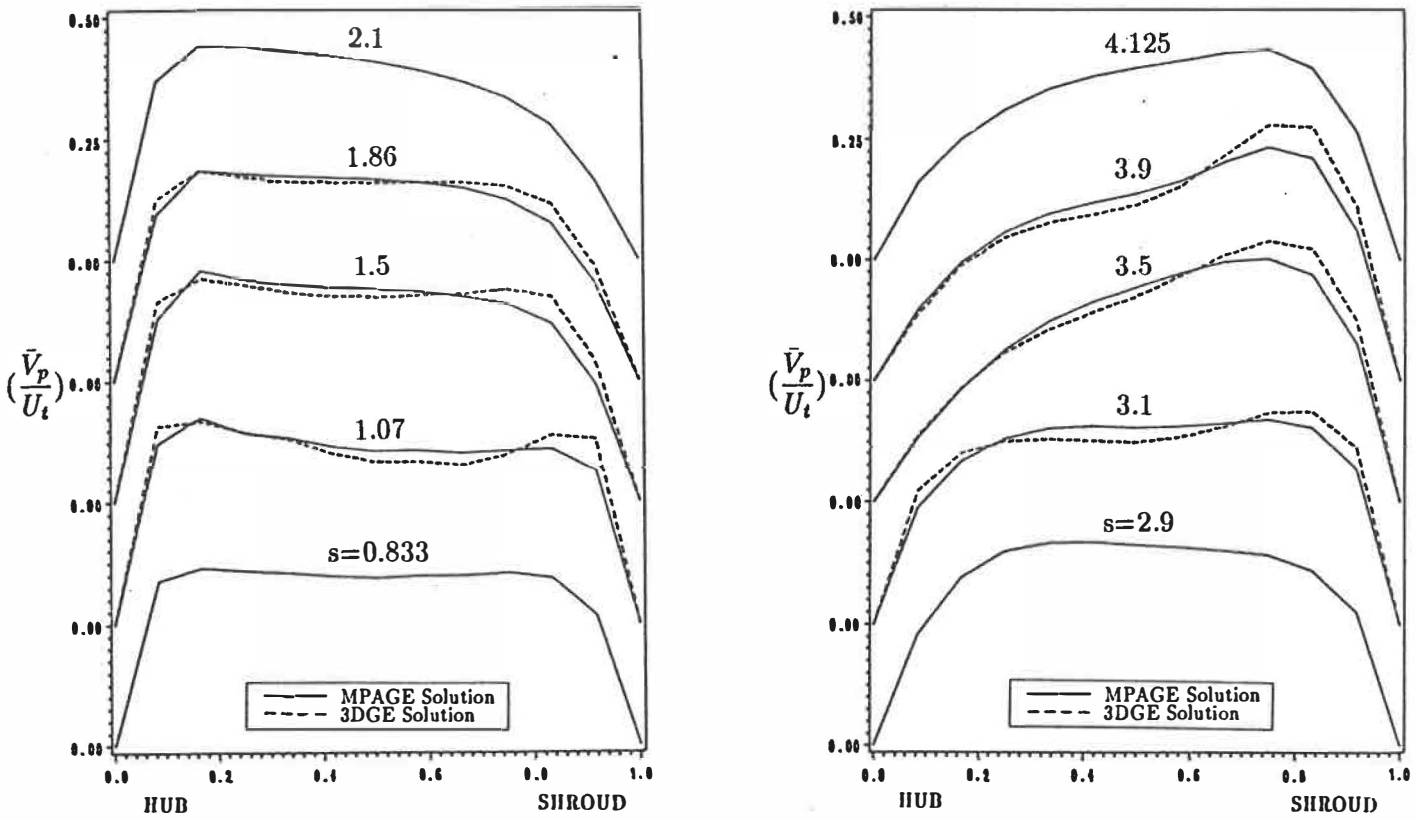

(d) $\mathrm{R} = 0.667$ (e) $\mathrm{R} = 0.833$ (f) $\mathrm{R} = 0.917$

**Figure 8.23: Blade-to-Blade Velocity Vector, Stator**




(a) s=3.1 (b) s=3.5 (c) s=3.9

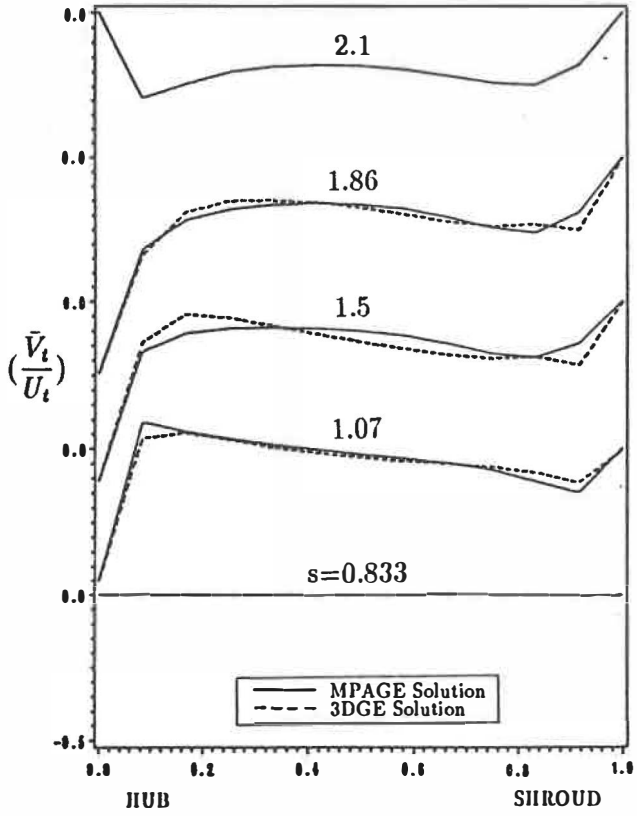
Figure 8.24: Secondary Velocity Vectors, Stator



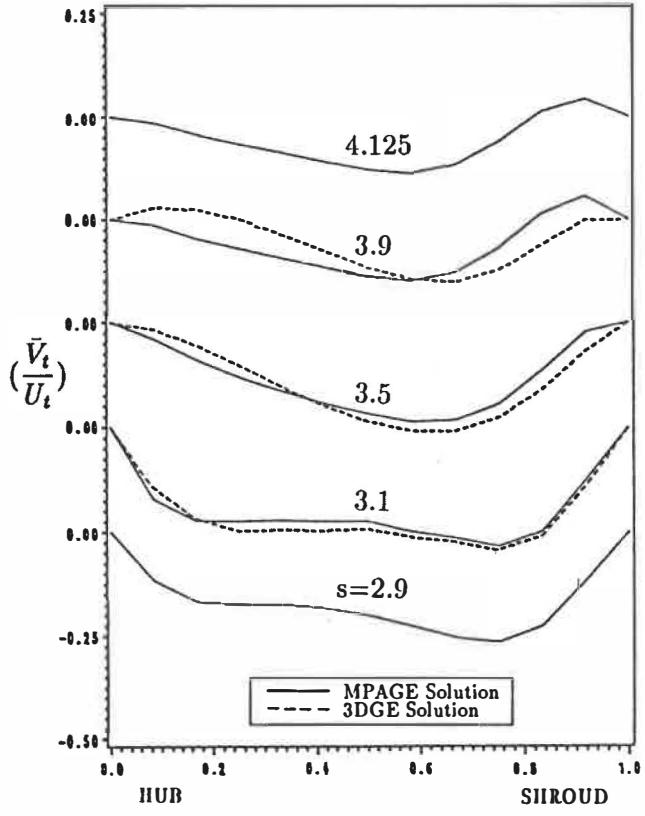

(a) Around Rotor

(b) Around Stator

Figure 8.25: Passage-Averaged Hub-to-Shroud Velocity Component $\bar{V}_p$

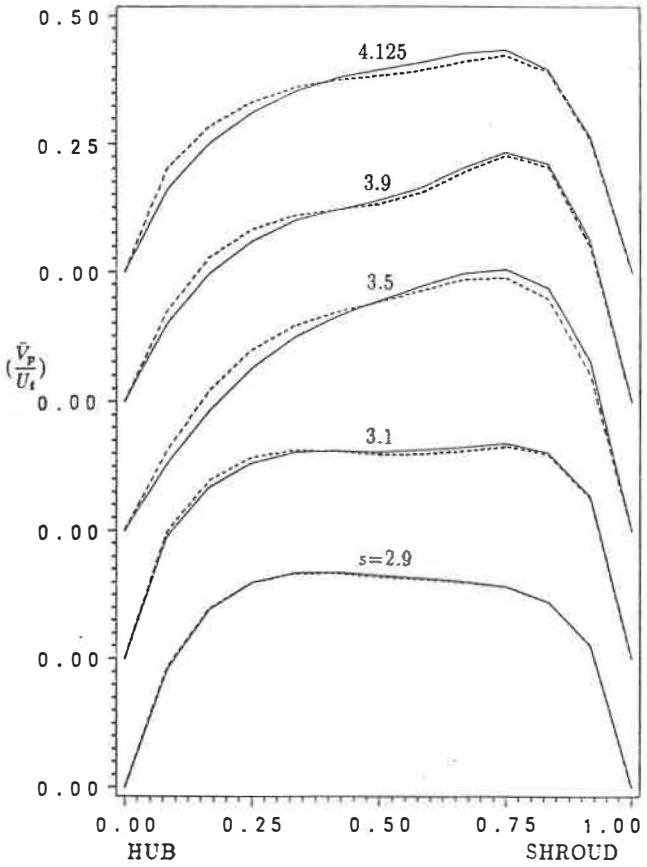



(a) Around Rotor

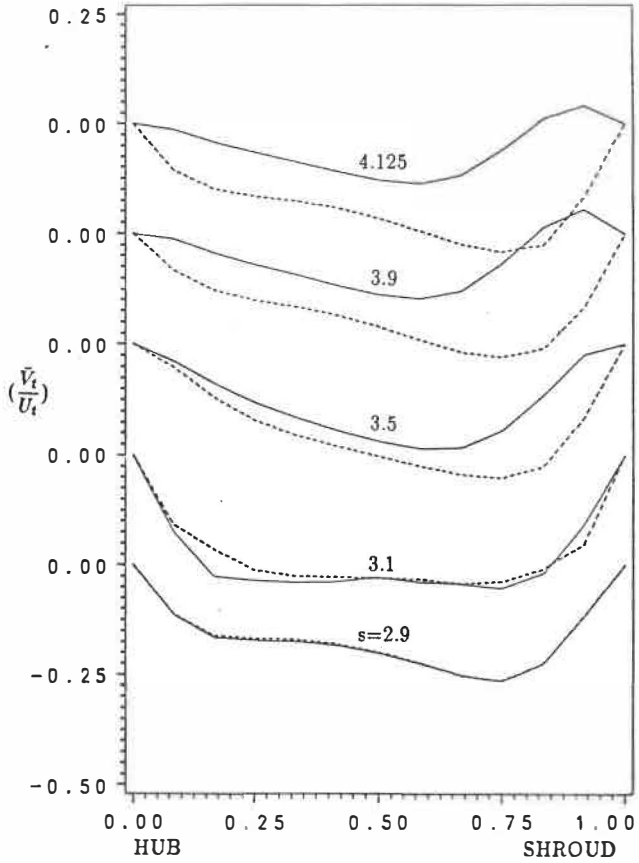



(b) Around Stator

Figure 8.26: Passage-Averaged Hub-to-Shroud Velocity Component $\bar{V}_t$




(a) Component $\bar{V}_p$




(b) Component $\bar{V}_t$

**Figure 8.27: Passage-Averaged Hub-to-Shroud Velocities with and without the Stator**

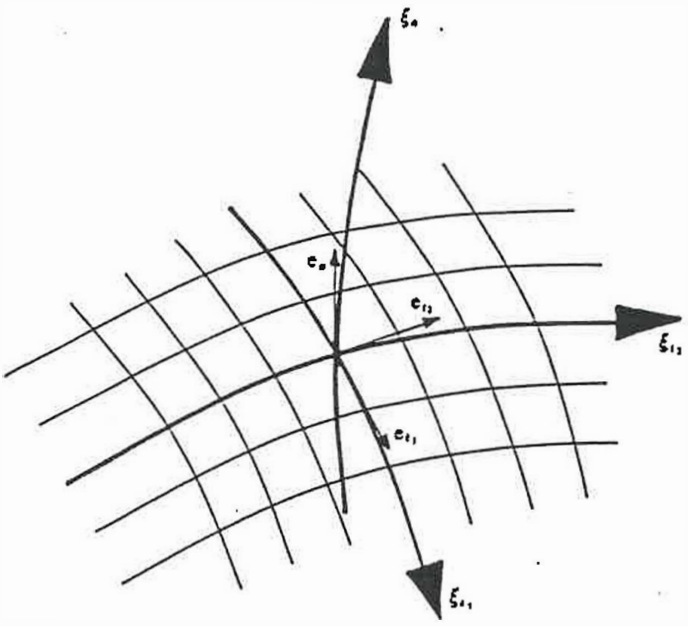


Figure B.1: Local Coordinate System on the Boundary Surface

ÉCOLE POLYTECHNIQUE DE MONTRÉAL
3 9334 00291756 3

ZH
1
CA
UP
199
Z64